

Institute of Petrology and Structural Geology Faculty of Science Charles
University, Prague

Institute of Geophysics The Academy of Sciences of the Czech Republic

Ph.D. thesis, Prague, 2011

**Relation of pore space geometry,
permeability and microstructure in
low-porosity rocks**

Matěj Machek

Supervised by Stanislav Ulrich

Dnes do háku opět nešel

a nic nezařídil ani

cennější je denní snění

než hovadský lopocení...

Národní Třída - Do háku(J. Topol)

A co říkám já?

**Čtěte a memorujte všechno nejen zepředu,
ale i odzadu a zevnitř. Jenom takovým
hloubkovým stúdiem se vzděláte jako já.**

Velryba (J. Trnka a B. Pojar - Zahrada)

Acknowledgments

First and greatest thanks belong to Marta Edith, Doubravka and Diviš for their support and love.

I would like to thank Stano Ulrich who survives to supervise my thesis for such a long time with great patience. I also owe him thank for significant help with forming this manuscript. I would like to thank Aleš Špičák and Zuzana Kratinová for revision and help with manuscript text and Zuzana also for AMS measurements. I thank to all my colleagues who helped me as collaborators of thesis parts, namely to Petr Špaček, Ondra Lexa, David Mainprice, Florian Heidelberg, Lenka Baratoux, Rostislav Melichar and Jakub Haloda. Lukáš Padjen is acknowledged for the P-wave velocity anisotropy measurements. Lots of thanks are addressed to all the people from my home departments at Institute of Geophysics and Faculty of Sciences. I acknowledge also Ivan Rozkošný from NIKON for technical support.

The thesis was financed from resources of research plan of the Institute of Geophysics, ASCR, no. AV0Z30120515, SÚRAO/G-Bariéra project and GAČR project No. 205/08/0767.

At the end I shall thank to Cirkus alien, Dead Kennedys, Kmts, Koda, Atari teenage riot, Chaos UK, Jahba, Rage against the machine, L7, Analogue death, Radio23, BEATS'N BREAKS, PsychoRadio and all the others for their music which kept me working.

Abstract

Influence of different rock structure aspects (grain size of mineral grains, contribution of individual microstructures, role of original magmatic and/or metamorphic microstructure and brittle structure of rock massif) on pore space geometry evolution was studied. Eclogite, granite and metagabbro rock samples were examined to see different microstructural rock characteristics. Combination of quantitative microstructural analysis of grains, grain boundaries and microcrack network, measurement of lattice preferred orientation and measurements of elastic velocities at increasing confining pressure turned out to be effective in evaluation of preferred orientation of the pore space in rock samples. Together with information about porosity and permeability these analysis represents solid methodology for determination of zones of potentially high risk of fluid infiltration to the rock mass.

In studied eclogites the microporosity is related to cracks at grain boundaries and cleavage cracks ((110) planes) in clinopyroxene. With increasing confining pressure, grain boundaries close below 50 MPa, while cleavage planes in clinopyroxene remain open up to 100 MPa.

In Melechov granites the pore space geometry reflects the orientation of exfoliation planes or the pore space is preferentially oriented 20° to 40° oblique to the closest macrofracture. Microcrack preferred orientation is in agreement with pore space geometry deduced from distribution of P-wave velocity differences. The most important crack type in terms of fabric strength and interconnectivity is intergranular crack. The pore space in granites formed by planar microcracks does not reflect the observed geometry of macroscopic fractures in the Melechov massif. More likely is the

explanation that microcracks forming preferred orientation developed in process zone of closest macrofracture during its propagation and/or reactivation.

In metagabbro rocks the pore space geometry generally reflects the microstructure. The micropores follow grain boundaries and cleavage planes of amphibole mainly. The study indicate that even above confining pressure of 200 MPa the microcrack pore space in metagabbro remains open to some extend.

Abstrakt

Studie se zabývá vlivem různých strukturních aspektů na vývoj geometrie pórového prostoru v málo porézních horninách. Zabýval jsem se studiem eklogitů, granitů a metagabru, neboť různé horninové typy umožňují porozumět vlivu více odlišných mikrostrukturních charakteristik na pórový prostor. Kombinace kvantitativní mikrostrukturní analýzy zrn, hranic zrn a mikrotrhlin společně se stanovením krystalové přednostní orientace hlavních horninotvorných minerálů a měření prostorového rozložení a anizotropie ultrazvukových P-vln se ukázala být efektivní při určování orientace pórového prostoru v horninách. Při současné znalosti pórovitosti a propustnosti a její směrové závislosti představují výše zmíněné techniky významný metodologický postup k odhalování oblastí horninových masivů, ve kterých hrozí nebezpečí infiltrace a cirkulace tekutin. Ve studovaných eklogitech je pórový prostor tvořen mikrotrhlinami na hranicích zrn a klivážových plochách v klinopyroxenu (krystalové plochy (110)). S rostoucím omezujícím napětím se trhliny na hranicích uzavírají za 50 MPa a kliváže v klinopyroxenu uzavírají otevřené do 100 MPa. V granitech z Melechovského masivu geometrie pórového prostoru odpovídá orientaci exfoliačních ploch, anebo je přednostně orientován šikmo mezi 20 a 40 stupni k nejbližší makroskopické fraktuře. Přednostní orientace mikrotrhlin odpovídá geometrii pórového prostoru odvozeného z měření ultrazvukových P-vln za rostoucího omezujícího tlaku. Nejdůležitějším typem mikrotrhlin vzhledem k přednostní orientaci pórového prostoru a zároveň nejdůležitějšími pro propojenost se ukázali být trhliny intergranulární. Přednostní orientace mikrotrhlin v námi studovaných vzorcích nesouhlasí s orientací makroskopických křehkých poruch. Naopak se

zdá, že jejich systematická orientace vůči nejbližší makrofraktuře odpovídá vzniku mikrotrhlin v procesní zóně vznikající či reaktivované fraktury. Ve vzorcích metagabber Staroměstského pásma pórový prostor sleduje převážně hranice a kliváže zrn amfibolu. Studie ukazuje že v těchto horninách zůstávají póry, s největší pravděpodobností mikrotrhliny, otevřeny i za omezujících tlaků přesahujících 200 MPa.

Contents

1. Introduction	1
1.1. Motivation and goals	3
1.2. Methodology	5
1.3. Applied Methods	7
1.3.1. Anisotropy of p-wave velocity and pore space geometry	7
1.3.2. Microstructure	9
1.3.3. Rock Texture	12
1.3.4. Porosity and Permeability	13
2. Origin and orientation of microporosity in eclogites of different microstruc- ture studied by ultrasound and microfabric analysis	17
2.1. Microstructural and grain boundary orientation analyses . . .	19
2.1.1. Fine-grained eclogite (JK1b)	19
2.1.2. Coarse-grained eclogite (SNW3)	20
2.2. Lattice preferred orientation	22
2.2.1. Fine-grained eclogite (JK1b)	24
2.2.2. Coarse-grained eclogite (SNW3)	24
2.3. Anisotropy of P-wave velocities	25
2.3.1. Fine-grained eclogite (JK1b)	25
2.3.2. Coarse-grained eclogite (SNW3)	27
2.4. Orientation of microporosity	27
2.4.1. Fine-grained eclogite (JK1b)	27
2.4.2. Coarse-grained eclogite (SNW3)	29
2.5. Discussion	29

2.6. Conclusions	33
3. Relation of pore space geometry, permeability and microstructure of three granite types	35
3.1. Geological background and structure of the Melechov Massif .	36
3.2. Description of samples	38
3.2.1. Magmatic fabric	40
3.3. Anisotropy of p-wave velocity and pore space geometry	42
3.4. Porosity and permeability	46
3.5. Microstructural analysis	48
3.6. Analysis of connected network	53
3.7. Summary and Discussion	56
3.8. Conclusions	61
4. Development of pore space geometry in progressively deformed metagabbro	63
4.1. Description of samples	64
4.2. Lattice preferred orientation and deformation mechanisms . .	67
4.3. Seismic anisotropy	68
4.3.1. Experimental results	69
4.3.2. Numerical results	72
4.4. Pore space geometry	74
4.5. Summary and Discussion	77
4.6. Conclusions	80
5. Summary	83
References	87
A. Appendix I	103
B. Appendix II	111
C. Appendix III	115

1. Introduction

The fluid transport in deformational zones of the Earth's crust has been previously the principal target of numerous studies (e.g. Fyfe et al., 1978; Kerrich, 1986; Sibson et al., 1988; McCaig, 1988; Bruhn et al., 1990; Forster and Evans, 1991; Selverstone et al., 1991; Chester et al., 1993). It has been showed that fluid-fault-rock interaction can cause changes in volume, permeability and enhanced weakness of fault zones. Investigation of fluid transport in fault and fracture zones is essential in research of geothermal and petroleum reservoirs and the long-term and safe insulation of long-lived wastes in underground repositories. Laboratory analyses of fault gauges (Chu et al., 1981; Faulkner and Rutter, 1998; Lockner et al., 2000) usually show low permeabilities, which indicate that some parts of fault zones can represent natural barriers for fluid transport. However, number of studies indicate that zones of high microfracture density are often developed in association with faults and macroscopic fractures (Scholz et al., 1993; Anders and Wiltschko, 1994; Vermilye and Scholz, 1998; Zang et al., 2000; Wilson et al., 2003). Permeability in these zones of microfracturing is often much higher than that of the protomylonites (e.g. Caine et al., 1996; Evans et al., 1997; Seront et al., 1998; Simpson et al., 2001). Such increase in permeability and microcrack density in fracture zones can be observed at the scale of laboratory samples, thus it is not associated only with macroscopical brittle structures. Detailed analyses of deformational zones shows the relation between the permeability, microcrack orientation and the position within the fault zone can be rather complicated (Scholz et al., 1993; Anders and Wiltschko, 1994; Vermilye and Scholz, 1998; Zang et al., 2000;

Wibberley and Shimamoto, 2003; Wilson et al., 2003). Porosity in the rocks outside the zones of large deformation is formed mostly by a network of microcracks which are responsible for the fluids infiltration and transition. The permeability and its anisotropy in such rocks are closely related to the character of the microcrack network. Orientation and properties of microcrack networks is often controlled by regional stress orientation (Plumb et al., 1984; Kowalis et al., 1987; Vollbrecht et al., 1991). Pores or open cracks strongly influence its petrophysical properties, e.g. decreasing tensile and shear strength, decreasing the velocity of elastic waves or increasing the permeability. In low-porosity rocks the pores usually have microscopic dimensions, they are often related to the thermo-mechanical history of the rock being linked with a metamorphic cleavage, microfractures, or boundaries of preferentially oriented mineral grains (Kranz, 1983). Unlike meso- or macroscopical brittle structures, the direct analysis of such small-size discontinuities (microcracks) is difficult because it requires a 3D geometric description at microscale. However, some specific physical features of rocks which are closely linked to pores can be used for laboratory analysis of the quantity, orientation and other properties of microcracks. These are mainly inelasticity which leads to a decrease of seismic velocities and seismic attenuation, and permeability which is a function of content, orientation and interconnection of pores. The anisotropy of these physical properties is related to the preferred orientation of microcracks that can transport fluids through rock mass in low porosity rocks, not affected by macrofracturing (e.g. Brace and Orange, 1968; David et al., 1999; Petrov, 2005). Experimental research also documents that microcrack dilatancy is responsible for increased permeability in deformed rocks (Zoback and Byerlee, 1975; Schulze et al., 2001; Simpson et al., 2001). In some experiments the dilatancy and increased permeability were observed even under plastic regime of deformation (Peach and Spiers, 1996). The permeability and its anisotropy is controlled by geometry, interconnectivity, density, aspect ratio and roughness of microcracks (e.g. Scholz, 1968a,b; Brace and

Orange, 1968; Scholz, 1968a,b; David et al., 1999; Benson et al., 2006a,b; Shild et al., 2001). The orientation of microcracks and hence the permeability anisotropy depends on stress field orientation during the deformation (Plumb et al., 1984; Kowalis, 1987; Vollbrecht et al., 1991; Kano and Tsuchiya, 2002; Åkesson et al., 2004; Onishi and Shimizu, 2005). The permeability anisotropy caused by microcracks can reach one order of magnitude (Benson et al., 2006b; Shild et al., 2001). However, permeability can be influenced by relative orientation of microcracks to stress field even after the formation of deformational zone (e.g. Zoback and Townend, 2001). Development of microcracks is often concentrated into the “process zone” of larger fractures. “The process zone is a region of enhanced cracking surrounding the fault, produced by crack tip stress field of the propagating fault”(Scholz et al., 1993). Microcrack development in the process zone can be also related to the stress field produced by movement of reactivated fracture (Anders and Wiltschko, 1994; Vermilye and Scholz, 1998). The relative orientation of microcracks to the fracture depends on mode of fracture propagation and reactivation and its surface roughness (Scholz et al., 1993; Anders and Wiltschko, 1994; Vermilye and Scholz, 1998; Zang et al., 2000; Wilson et al., 2003). Despite the fact that the microcracks development strongly depends on local or regional stress field, it is also controlled by the precursor microstructure originated during magmatic and/or metamorphic stage of rock evolution. Formation of microstructure leads to establishment of important rock characteristics such as preferred orientation of crystal lattice, grain shapes and grain boundaries as well as compositional layering or other microstructural features.

1.1. Motivation and goals

This thesis deals with the relationship between the rock microstructure, texture and pore space geometry and permeability anisotropy in crystalline rocks. Pore space identification and geometry is of interest in a number of

contexts, such as: a) fluid and contaminant migration in low porosity rock masses (below 2%) fundamental for building radioactive waste repositories and underground storage reservoirs; b) seismology (the effect of microcracks on seismic properties of rocks), deeper Earth systems (such as a role of fractures in seismogenic zones or during metamorphism) etc. The waste repository or storage reservoir site is commonly situated in a rock mass of low porosity with minimum content of macroscopic fractures, which are most efficient for contaminant migration. In such places, geometry and origin of pore space is of great interest in order to describe physical pathways for fluids and, if possible, to define the depth level below which the majority of micropores is closed. For such reasons, the study is focused on identification and semiquantitative estimates of pore space orientation based on knowledge of microstructure and seismic properties as well as on understanding of the contribution of individual microstructures to the bulk pore space.

The thesis is composed of three partial studies concerning different aspects of relationship between microstructure and pore space geometry. First part documents influence of grain size on development and preferred orientation of pore space in simple rock system on the example of two microstructurally distinct eclogites. The second part investigate relations between the pore space geometry, permeability, microstructure and structure of granitic rocks collected in the Melechov granite in the central part of the Variscan Bohemian Massif. In this study we combined indirect and direct methods to study pore space geometry and its relationship to microstructure and elastic properties of granitic specimens. The third part is concentrated on the role of microstructure originated during magmatic and/or metamorphic stage of rock evolution on the pore space development during relieve of lithostatic stress and brittle deformation. In the study we examine pore space geometry in relation to stages of progressive deformation of metagabbro from the Staré Město belt (Bohemian Massif).

1.2. Methodology

Frequently used direct methods are based on quantitative microstructural analysis of thin sections prepared from three mutually perpendicular sample sections. Petrographical thin sections were used for the microstructural analysis (Vollbrecht et al., 1991; Siegesmund and Vollbrecht, 1991; Siegesmund et al., 1993; Takeshita and Yagi, 2001; Takemura et al., 2003) or thin sections from samples saturated by fluorescent resin (Anders and Wiltschko, 1994; Shild et al., 2001; Onishi and Shimizu, 2005; Liu et al., 2006). Microcracks in thin section were also studied using image analysis of scanning electron microscope images (Batzle et al., 1980; Katz et al., 2003; Haimson and Chang, 2005), back-scattered electron images (Kanaori et al., 1991; Wilson et al., 2003) and images from confocal scanning laser microscope allowing 3D reconstruction of microcrack network (Menendez et al., 2001; Onishi and Shimizu, 2005; Liu et al., 2006). Indirect information on the content and orientation of microcracks can be deduced from elastic properties of rocks (e.g. Birch, 1961; Benson et al., 2006a,b). The dependence of seismic properties on porosity has been experimentally studied in many low-porosity rocks with microcracks (e.g. Siegesmund et al., 1996; Popp and Kern, 2000; Kern et al., 2001). In most cases, these experiments have been carried out taking several oriented cylinders from each sample or alternatively on spherical samples measured in many directions (Babuška and Pros, 1984; Siegesmund et al., 1993; Rasolofosaon et al., 2000; Schild et al., 2001; Přikryl et al., 2005; 2007; Machek et al., 2007). Pore space geometry can be determined from elastic properties of rock by its inversion using Kachanov (1994) „noninteractive effective medium“ theory (Sayers and Kachanov, 1995; Guéguen and Diens, 1989; Guéguen et al., 1997; Guéguen and Schubnel, 2003; Schubnel and Guéguen, 2003; Benson et al., 2006a,b; Schubnel et al., 2006). Another method which can be used for the analysis of open pore space is a measurement of electrical properties. Several authors used this method for laboratory petrophysical characteristics of the

rock samples (e.g. Lockner and Byerlee, 1985; Ruffet et al., 1991; Freund and Nover, 1995; Pezard et al., 1999) or as a study tool for experimentally produced brittle microstructures (e.g. Glover et al., 1997).

The thesis is founded on investigation of the elastic properties of rock samples using a high-pressure ultrasonic apparatus, which gives a 3D image of compressional elastic wave velocities (Pros and Babuška, 1968; Pros et al., 1998). A number of laboratory investigations of rock samples have demonstrated that microcracks significantly decrease elastic wave velocities (e.g. Birch, 1961; Brace, 1965; Babuška and Pros, 1984) and that with increasing depth (lithostatic pressure), the majority of microcracks progressively closes down, causing the increase of elastic waves velocity (e.g. Birch, 1961). Oriented systems of porosity may cause velocity anisotropy even if the matrix of the rock is almost isotropic (Babuška et al., 1977). If measurements have been carried out on a spherical sample in many directions, the difference between P-wave velocities measured at atmospheric pressure and at a higher hydrostatic pressure is a useful tool for the visualization of microporosity (velocity difference - ΔV_P) in a stereodiagram (Babuška and Pros, 1984; Siegesmund et al., 1993). Babuška and Pros (1984) correlated opening of major cleavage planes and cracks as a function of confining pressure in the case of granodiorite and quartzite, finding that the flat cleavage cracks and their orientation have the strongest influence on elastic wave velocities and their anisotropy at atmospheric and low hydrostatic pressures. Siegesmund et al. (1993) investigated the influence of rock fabric on the spatial distribution of P-wave velocities in orthogneisses. They correlated directions of high P-wave velocity differences at low confining pressures with directions of minimum values of P-wave velocities. Cleavage cracks in biotite and grain boundary cracks parallel to foliation have the main influence on elastic wave velocity in orthogneiss and its anisotropy at low pressures.

In the thesis, pressure-dependent change of elastic properties is used as a direct measure of microcrack orientation and volume. Pore space geometry

data obtained from velocity measurements are combined with quantitative microstructural analysis of grains, grain boundaries (Chapter II) and microcrack networks (Chapter III), texture of the rock samples (Chapter II and IV) and porosity and permeability measurements (Chapter III).

1.3. Applied Methods

1.3.1. Anisotropy of p-wave velocity and pore space geometry

Pore space geometry was investigated using the 3D analysis of velocity of ultrasonic P-waves (V_P) measured on the samples at changing confining pressure. The difference of velocity measured at two different levels of confining pressure in certain direction (Fig. I.1), the ΔV_P (Δp), is largely due to the effective volume changes of small pores in the rock. The analysis of spatial distribution of ΔV_P (Δp) can be used to describe the preferred orientation of such micropores, and it can be linked directly with the preferred orientation of microcracks since these are usually associated with each other (e.g. Popp and Kern, 2000; Kern et al., 2001; Schild et al., 2001; Benson et al., 2006a,b). The ultrasonic P-wave velocity measurements have been carried out by means of the pulse transmission technique using the apparatus designed at Institute of Geophysics ASCR, Prague, for measurement on spherical rock samples (Pros and Babuška, 1968; Pros et al., 1998). The spherical sample is mounted on a holder in the pressure vessel where it can be rotated to any direction desired. For purposes of this study we used several levels of confining pressure up to 400 MPa (commonly 10, 20, 50, 100, 200, 400 MPa) and the individual measurements were carried out in a $15 \times 15^\circ$ grid. The velocity anisotropy, A , was then calculated as $A = [(V_{Pmax} - V_{Pmin}) / ((V_{Pmax} + V_{Pmin}) / 2)] * 100\%$, after Birch (1961). To compare the degree of preferred orientation of pores in the studied rocks, the anisotropy of P-wave velocity differences were calculated between confining pressure steps 400-min MPa, 400-100 MPa and 100-min MPa as $a =$

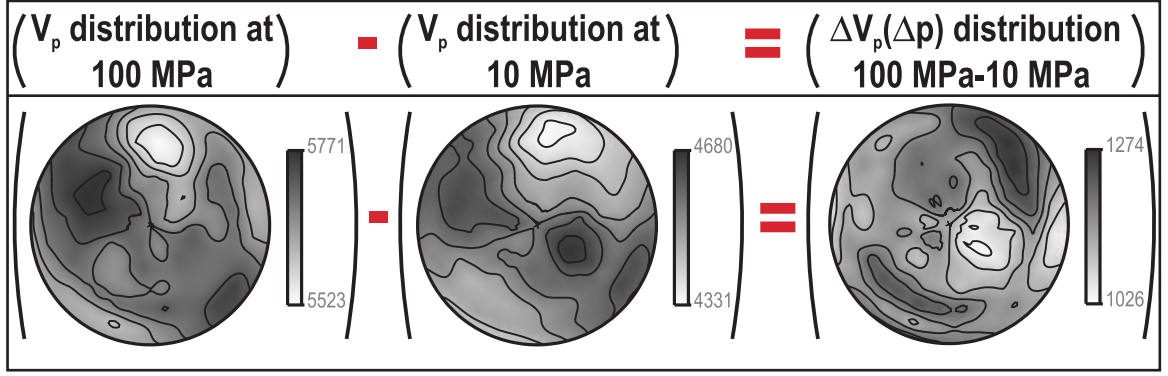


Figure I.1. Construction of diagram of spatial distribution of ΔV_p (Δp) (the pore space geometry), by subtraction of P-wave velocity distribution at two levels of confining pressure. Here 100 MPa and 10 MPa levels (Melechov granite).

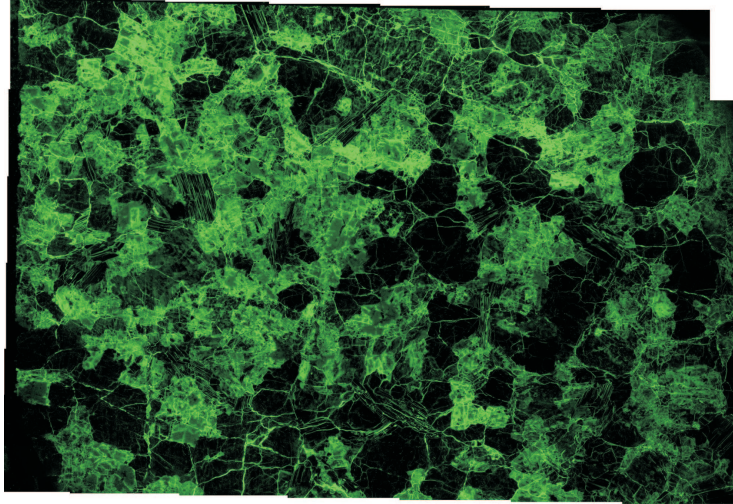
$(\Delta V_{p\max} - \Delta V_{p\min}) / V_{p\max}$. where $\Delta V_{p\max}$ and $\Delta V_{p\min}$ are maximum and minimum of difference between P-wave velocities measured at given levels of confining pressure and $V_{p\max}$ is P-wave velocity maximum obtained at higher confining pressure. For additional description of the samples, the sum and mean of P-wave velocity differences between given pressure levels in all 132 measured directions were calculated. The mean of ΔV_p was calculated to assign the relative amount of open space in the studied rock samples. Obtained velocity data and data of $\Delta V_p(\Delta p)$ dependence in space are presented in stereodiagrams (lower hemisphere, equal area projection). Three sources of possible errors of measurements are considered: sample distortion, first onset picking inaccuracies and pressure instabilities. The sample distortion is mainly due to pressure induced closing of micropores. Since we are dealing with low-porosity rocks, we estimate the resulting error of V_p at less than 1%. The first onset picking inaccuracies can be large namely under low confining pressure in low velocity directions and the estimated errors of V_p are around 1%. The first onset picking inaccuracies decrease rapidly with increasing confining pressure and for pressures 20-400 MPa we estimate the errors due to the first onset picking inaccuracies to about 0.3-0.5%. In spite of manual corrections of pressure level during measurement, the pressure instabilities during the single run of multidimensional measurements at certain pressure can be as high as 1

MPa (usually 0.2-0.4 MPa). We estimate the maximum errors of V_P resulting from pressure instabilities during individual runs of 3-D measurement to 1.5% for atmospheric pressure and 0.2% for maximum confining pressure. For the calculation of P-wave velocities and numerical comparison with experimental results a special computer program has been developed (Špaček and Melichar, 2005). The calculation is based on finding the elastic stiffness tensor for an aggregate of all constituent mineral phases. For each mineral phase the crystallographic orientation distribution is measured using the EBSD method. The elastic stiffness tensors of all phases are computed using the single crystal elastic constants. Based on stiffness tensors, volume fractions and densities of mineral phases, the aggregate stiffness tensor can be calculated using selected elastic mixture rule. For amphibole we used the elastic stiffness constants of Alexandrov and Ryzhova (1961). Calculation of elastic stiffness constants of plagioclase was based on the chemical composition using the simple interpolation of the end-members as given in Seront et al. (1993). Voigt-Reuss-Hill average was used as a mixing rule. After the unification of coordinate systems of the two datasets, discrete experimental data are interpolated and numerically compared with the calculated data in a dense grid. The spatial distribution of the deviations is visualized by stereodiagrams.

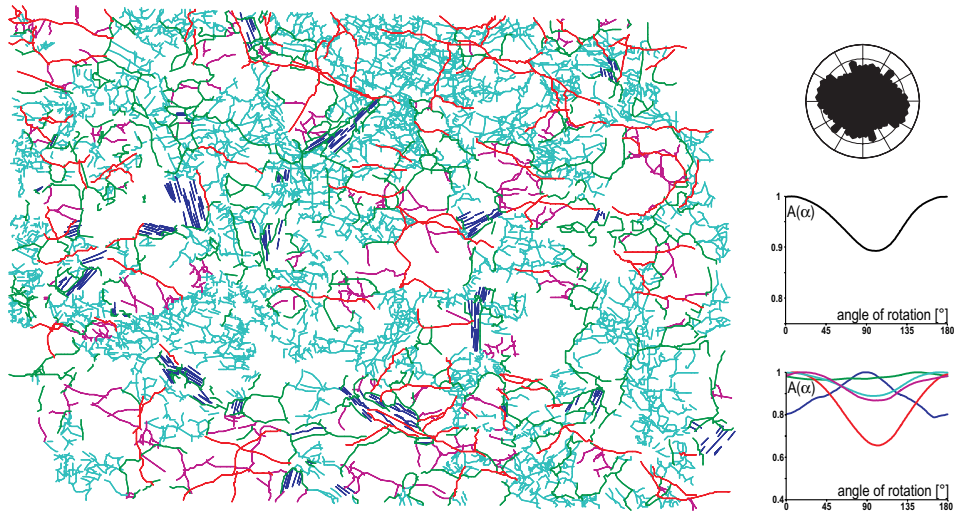
1.3.2. Microstructure

A quantitative microstructural analysis of grain boundaries was carried out in ESRI ArcView© 3.3 GIS environment. Grains were manually traced from micrographs obtained from three thin sections cut parallel to XZ, YZ and XY planes of finite strain ellipsoid. The map of grain boundaries was generated using ArcView extension Poly (Lexa et al., 2005). The resulting polygons have been treated by MATLAB™ PolyLX Toolbox (Lexa et al., 2005) and used for quantitative microstructural analysis. Average grain size is given as Feret diameter ($F = 2\sqrt{(A/\pi)}$, where A is area of grain). Grain bound-

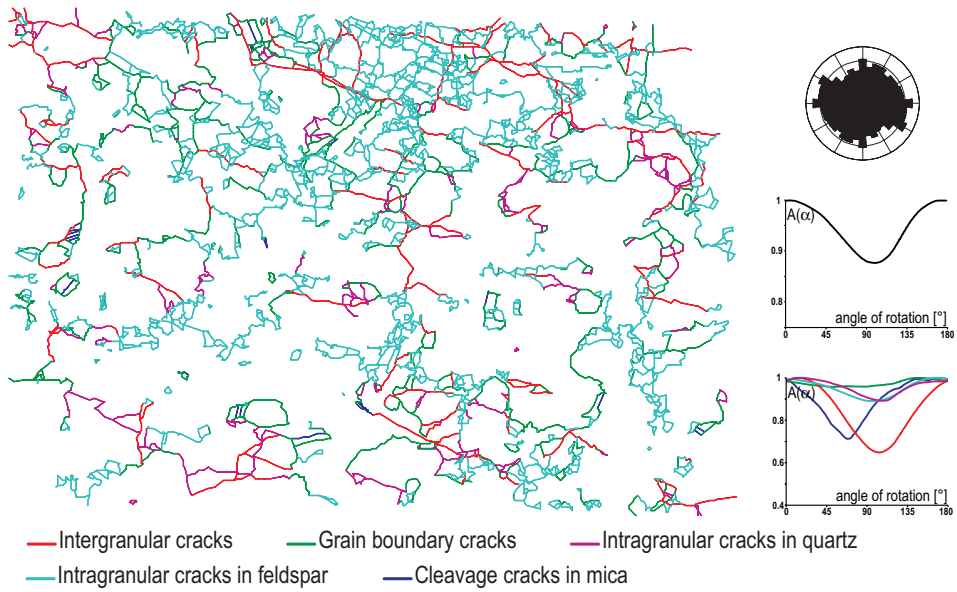
(a) Microphotographs taken in UV light



(b) Map of traced microcracks



(c) Skeleton of connected microcracks



ary preferred orientation was determined using the moment of inertia ellipse fitting and eigen analysis of bulk orientation tensor technique and its degree is expressed as eigenvalue ratio of weighted orientation tensor of grain boundaries. Quantitative microstructural analysis of microcrack networks was performed on the samples which were vacuum-saturated by fluorescent epoxy resin prior to the preparation of thin sections. Three sections were cut from each sample with the orientation scheme given by the results of the ultrasonic velocity measurements. From each thin section, a set of microphotographs (Fig. I.2a) was taken in UV and polarized light, upon which the microstructural features were manually traced in ArcView GIS environment. The map of microcracks (Fig. I.2b) was analysed quantitatively using FracNetLX - Fracture network analysis toolbox for MATLAB™ (Ondrej Lexa (c) 2010). Microcracks were classified into five microstructural types: intergranular cracks, grain boundary cracks, and intragranular cracks in quartz, feldspars and mica. Density, proportion, the preferred orientation and projection function $A(\alpha)$ obtained from SURFOR analysis have been determined from the classified vector map of microcracks. The quantitative microstructural analysis of connected microcracks is based on the analysis of fracture network cleaned until no 1st degree node exists, withal keeping nodes on convex hull of the original network (Fig. I.2c). This produces a “skeleton” of connected microcracks of the network. The skeleton of fracture network was subjected to the same analysis of microcrack properties and orientation as the entire network. The microstructural analysis of connected parts of fracture networks is amended by analysis of connectivity

Figure I.2. Illustration of microcrack analysis procedure: (a) Compiled set of microphotographs taken in UV light from thin sections of samples, which were vacuum-saturated by fluorescent epoxy resin. (b) The map of microcracks classified into five microstructural types: intergranular cracks, grain boundary cracks, and intragranular cracks in quartz, feldspars and mica. (c) Skeleton of connected microcracks - fracture network cleaned until no 1st degree node exists, withal keeping nodes on convex hull of the original network. Example of the rose diagrams of microcrack orientation and microcrack fabric of all cracks and of individual crack types. The curve $A(\alpha)$ represents the average crack projection (see SURFOR; Panozzo, 1984). $A(\alpha)$ is normalized: $A(\alpha)_{\max} = 1.00$.

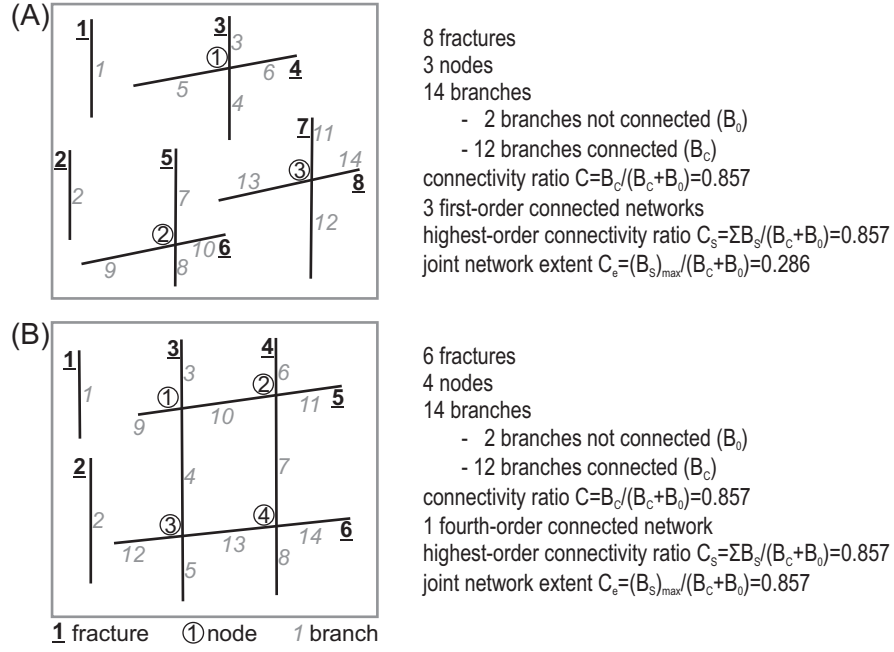


Figure I.3. Difference of two joint patterns with the same connectivity ratio. Illustration shows meaning of terms fracture, node and branch in terms of connectivity analysis and main features of fracture patterns. (a) Fracture pattern with 3 first-order connected networks. (b) Fracture pattern with 1 fourth-order connected network. Modified after Zhang et al. (1992).

using total connectivity ratio C , k th-order connectivity ratio C_k and crack network extent C_e as defined by Zhang et al. (1992) (Fig. I.3) as:

$$C = B_c / (B_c + B_0).$$

$$C_k = \sum B_k / (B_c + B_0).$$

$$C_e = (B_s)_{\max} / (B_c + B_0)$$

where B_c is the total number of connected crack branches in the crack pattern, B_0 is the total number of non-connected crack branches in the crack pattern. $\sum B_k$ is the sum of the connected crack branches of all k th-order connected networks in a crack pattern and $(B_s)_{\max}$ is the number of connected branches in a single crack network of order s having the highest number of connected branches (Zhang et al., 1992).

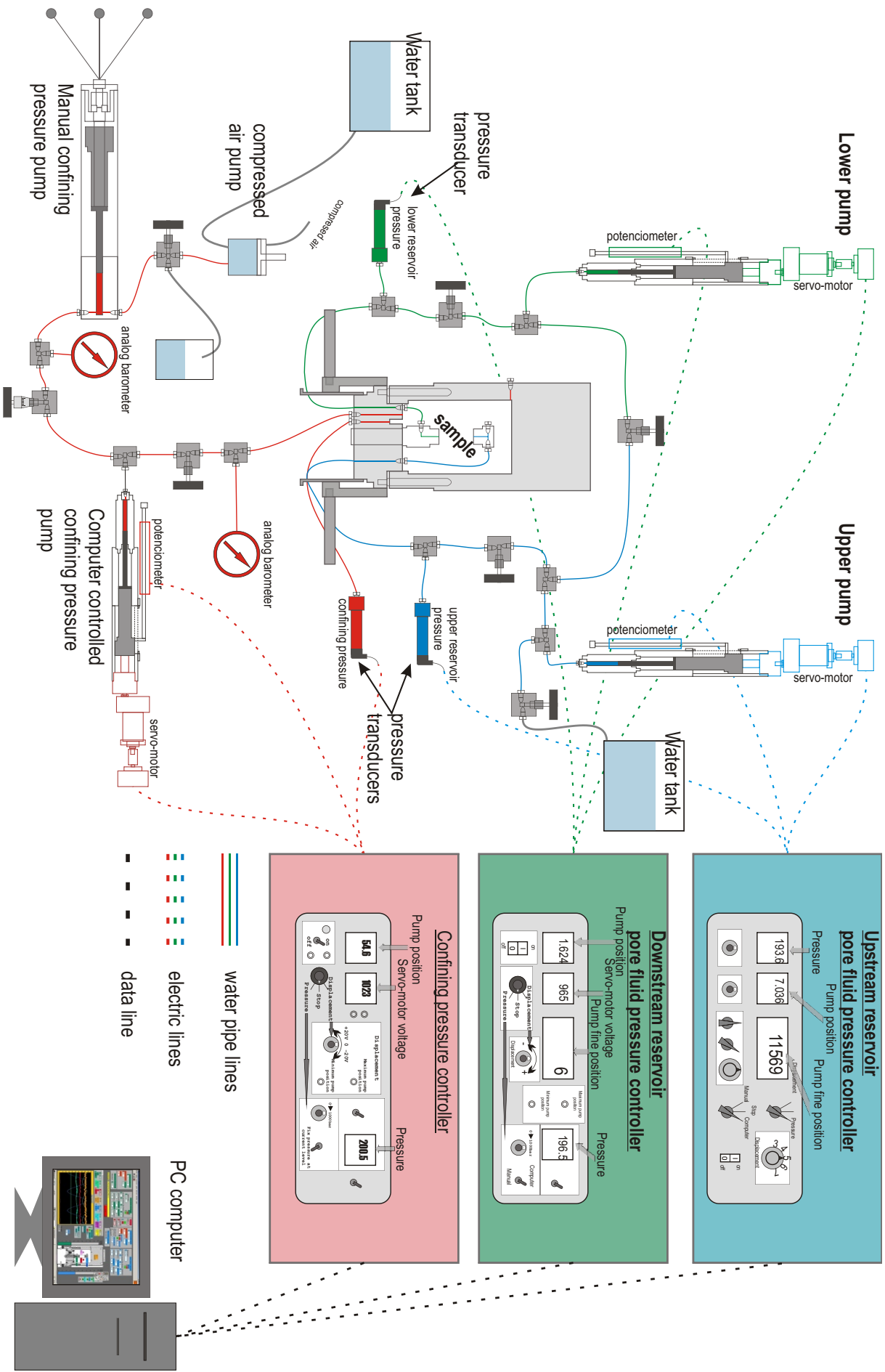
1.3.3. Rock Texture

Lattice preferred orientation (LPO) on rock forming minerals was measured on the scanning electron microscope (by electron backscatter diffraction

(EBSD) technique (e.g. Lloyd et al., 1991). This technique is based on automatic analysis of electron back-scattered diffraction patterns (EBSP) generated by interaction of a vertical incident electron beam with a flat crystal surface tilted to 70° from the horizontal. The EBSPs are recorded online by a phosphorus screen attached to a low-light CCD camera. At each point, the complete orientation of the crystal is determined. EBSPs were acquired at an accelerating voltage of 20 keV and a working distance of about 22 mm with a beam current of about 4 nA. EBSD patterns were processed and indexed using the CHANNEL5 software system by HKL Technology (Schmidt and Olesen, 1989). Results of LPO measurements are presented in equal area projection lower hemisphere pole diagrams, constructed using the Unicef careware software package developed by D. Mainprice (2005).

1.3.4. Porosity and Permeability

Two test cylinders with diameter of 2.5 ± 0.2 cm were prepared from each sample. The cylinder orientations corresponds to the direction of minimum and maximum difference between P-wave velocities measured at minimum (0.1 or 10 MPa) and 100 MPa of confining pressure. We assumed that the direction of minimum change of P-wave velocity with pressure (ΔV_P) are parallel to maxima of preferred orientation of microcracks and direction of maximum ΔV_P is normal to the plane of strongest preferred orientation of microcracks, representing the directions of highest and lowest permeability, respectively. Porosity (ϵ) was obtained from successively measured weight of dry (WD), water-saturated (WS) and water-immersed sample (WI) as: $\epsilon = V_p/V_s = (WS - WD) / (WS - WI)$, where V_p is the volume of sample pore space and V_s is the bulk volume of sample. Samples were first completely dried at a temperature 50°C in an oven until constant WD had been reached. To avoid any air in interconnected pore space, samples were degassed in a vacuum cell and then water-saturated in the cell still under vacuum. Saturated samples were weighted (WS) after sample surface was



slightly dried. For saturation, we used natural water of chemical composition given by the producer (Volvic): Ca^{2+} 11.5 mg/l, Na^{+} 11.6 mg/l, Cl^{-} 13.5 mg/l, SO_4^{2-} 8.1 mg/l, SiO_2 31.7 mg/l, Mg^{+} 8 mg/l, K^{+} 6.2 mg/l, NO_3^{-} 6.3 mg/l, HCO_3^{-} 71 mg/l. To measure WI, sample was placed on a hanger suspended under the balance and immersed in a water containing vessel. All weights were measured three times and then averaged. Permeability measurements were carried out on high precision permeameter of Laboratoire de Tectonophysique at the Université Montpellier II (Larive, 2002) at a room temperature (Fig. I.4). For the confining pressure and pore fluid was used the similar type of natural water as for saturation of samples. Measurements were made in a pressure vessel with a volume of 2.5 litres. Water injection in the vessel and its pressurization was provided by hydraulic pump driven by compressed air. The hydraulic pump was computer controlled. The confining pressure could be controlled in a limited range by either a manual piston pump or by a computer controlled servomotor driven piston pump. The latter one was also used to keep the confining pressure stable when at some fixed level. Confining pressure was acquired by electronic pressure transducer mounted next to the pressure vessel. The pore fluid system is divided into two circuits to enable to control pore fluid pressure in the upstream and downstream reservoirs separately. Pore fluid pressure in the reservoirs is controlled by high precision servomotor-driven piston pumps equipped with displacement transducers. The apparatus arrangement enables interconnection or volume reduction of upstream and downstream reservoirs using interconnection or reduction valves, respectively. Pressure acquisition is provided by two electronic pressure transducers mounted next to the ends of a sample. Water-saturated sample is placed into the highly elastic polyurethane jacket to separate the pore fluid pressure system from the confining pressure system. The sample is placed in between water-transmitting steel caps. Finally, the jacket is sealed to up-

Figure I.4. Scheme of the high precision permeameter in Geosciences Montpellier (Larive, 2002).

per and lower metal caps by rubber O-rings. First, the pore fluid pressure (Pf) of the up and downstream reservoirs and confining pressure (Pc) was increased simultaneously, with $P_c - P_f = 0.5$ MPa, until confining pressure reached 20 MPa. With confining pressure fixed, pore fluid pressure was adjusted to produce three effective pressure steps ($P_e = P_c - P_f$) of 0.5, 10 and 19 MPa. A permeability test was performed at each pore fluid pressure level by “steady state flow method”. The permeability is determined by imposing a pore fluid pressure gradient across the ends of the sample (~0.3 MPa difference of Pf between sample ends). When a constant flow rate is established through the sample, the flow rate of water through rock was determined by recording the change of displacement of upper and lower pore fluid pumps. Darcy’s Law is assumed to be valid, therefore the sample permeability can be calculated as: $k = Q\mu L / A\Delta P$. where k is the permeability, Q is the volume flow rate, μ is the viscosity of water, A is cross-sectional area of the sample normal to the direction of flow, L is the length of the sample and ΔP is pore fluid pressure difference between the sample ends.

2. Origin and orientation of microporosity in eclogites of different microstructure studied by ultrasound and microfabric analysis

co-authors: Petr Špaček, Stanislav Ulrich, Florian Heidelberg

published in Engineering Geology 89 (2007) 266–277

In this chapter, we examine origin and orientation of microporosity in two eclogites of similar lattice preferred orientation (LPO) of clinopyroxene but different grain size and microstructure using 1) qualitative and quantitative microstructural analysis of grains and grain boundaries orientation in three thin sections that are oriented parallel to XZ, XY and YZ planes of finite strain ellipsoid, 2) measurement of lattice preferred orientation using the electron backscattering diffraction (EBSD) method and 3) experimental measurement of the velocity of acoustic P-waves in spherical samples in 132 directions under confining pressures up to 400MPa. We choose eclogites as a simple bi-mineral rock type composed of omphacite and garnet as cleavage-bearing anisotropic and cleavage-free isotropic minerals, respectively. The study documents the influence of grain size and deformation stage of precursor microstructure on development and preferred orientation of pore space in a simple rock system. Two samples of eclogite (JK1b and SNW3) presented in this work provide different microstructural characteristics that refer to different metamorphic and deformational evolution

(Fig. II.1). The first sample (JK1b) is a dynamically recrystallized fine-grained crustal eclogite. The second sample (SNW3) belongs to the population of coarse-grained mantle eclogite xenoliths.

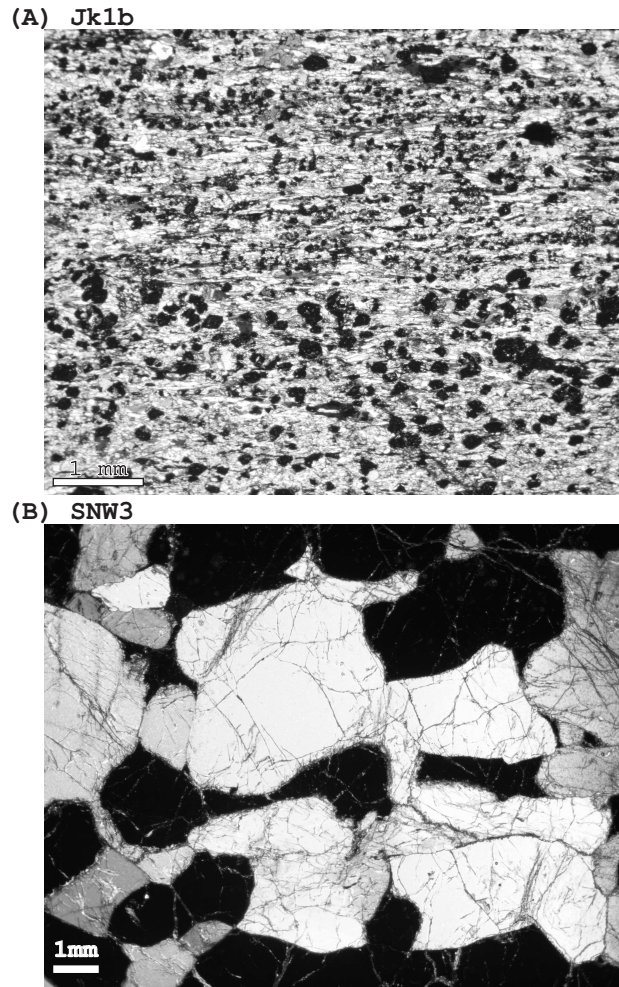


Figure II.1. Micrographs of thin sections illustrating the microstructure of a) sample JK1b and b) sample SNW3. Thin sections were prepared from spherical samples after experimental measurement of seismic velocities parallel to lineation and perpendicular to foliation in order to carry out quantitative microstructural and SEM-EBSD analyses. The majority of visible cracks in the sample SNW3 developed during the decrease of confining pressure at P-wave velocity measurements and also during thin section preparation.

Table II.1 Summary of microstructural analysis of studied samples

	Phase	% of volume fraction	Mean Feret diameter	Mean axial ratio		
				xz	xy	yz
JK1B	cpx	53.3	41.13 [μm]	2.46	2.39	1.74
	grt	30	87.05 [μm]	1.42	1.44	1.30
	amp	7.58	118.59 [μm]	1.52	2.47	1.84
	ru	3.52	29.21 [μm]	2.46	2.16	1.74
	q	2.9	65.30 [μm]	1.64	2.20	1.54
	par	2.27	93.82 [μm]	x	x	2.45
	zo	0.44	48.70 [μm]	1.72	x	x
SNW3	cpx	55.97	1.31 [mm]	1.96	1.78	1.75
	grt	44.03	2.20 [mm]	2.05	1.80	1.97

Modal mineralogies (%), mean Feret diameter (μm for sample JK1b and mm for sample SNW3), mean axial ratio. Axial ratio data are presented separately for sections parallel to XZ, YZ and XY planes of finite strain ellipsoid. cpx-clinopyroxene, grt-garnet, amp-amphibole, ru-rutile, q -quartz, par-paragonite, zo-zoisite.

2.1. Microstructural and grain boundary orientation analyses

A quantitative microstructural analysis of grains and grain boundaries was carried out on three thin sections cut parallel to XZ, YZ and XY planes of finite strain ellipsoid (Fig. II. 2). Grain boundary orientation is presented in rose diagrams corresponding to circular histograms of grain boundaries frequency (Fig. II.2). All data obtained from grains and grain boundaries orientation analyses are summarized in Table II.1 and II.2.

2.1.1. Fine-grained eclogite (JK1b)

The sample of fine-grained eclogite comes from a lens of eclogite emplaced in anatectic orthogneiss of the Czech part of the Krušné hory Mts., Bohemian Massif. An equilibration temperature of 600 - 650° and peak metamorphic pressure of 2.6 GPa were estimated for this eclogite (Klápová et al., 1998). The studied sample is a fine-grained mylonite with well developed macroscopic foliation and lineation defined by elongated clinopyroxene grains. The rock consists of 53.3% clinopyroxene, 30% garnet, 7.6% amphibole, 3.5% rutile, 2.9% quartz, 2.3% white mica (paragonite) and

0.4% zoisite (Table II.1). Clinopyroxene is dynamically recrystallized to an elongated fine grain size ranging between 3 μm and 265 μm with a mean Feret diameter of 41 μm . Garnet grains have idiomorphic shapes with size

Table II.2 Summary of grain boundary orientation analysis

	Boundary type	% of length			Eigenvalue ratio		
		xz	xy	yz	xz	xy	yz
JK1B	cpx-cpx	60.95	67.13	46.60	2.12	1.88	1.20
	cpx-grt	21.09	12.58	17.84	1.29	1.31	1.05
	cpx-ru	7.59	9.32	5.31	2.20	1.53	1.29
	amp-cpx	0.34	3.61	5.49	1.18	1.60	1.31
	grt-grt	3.08	1.02	4.90	1.52	1.65	1.07
	all	x	x	x	1.76	1.69	1.12
SNW3	cpx-cpx	27.92	24.53	23.44	1.17	1.06	1.16
	cpx-grt	68.33	65.87	73.04	1.36	1.02	1.28
	grt-grt	3.75	9.60	3.52	1.10	1.38	1.13
	all	x	x	x	1.30	1.05	1.22

Percentage of important grain boundary types, eigenvalue ratios of boundary types and of all traced boundaries in sections parallel to XZ, YZ and XY planes of finite strain ellipsoid.
cpx - clinopyroxene, grt - garnet, amp - amphibole.

ranging between 7 μm to 386 μm with a mean Feret diameter of 87 μm . The mean axial ratio of clinopyroxene and garnet grains ranges from 1.74 in YZ section to 2.46 in XZ section and from 1.30 in YZ section to 1.44 in XY section respectively (Table II.1). Orientation of grain boundaries is influenced mostly by clinopyroxene, which is the most abundant mineral. Eigenvalue ratios show a constrictional fabric of grain boundaries with strong preferred orientation in XZ (1.76) and XY (1.69) sections, while in YZ section the eigenvalue ratio is significantly lower (1.12). Thereby the grain boundaries form a constrictional fabric almost parallel to the direction of macroscopic lineation (deviating 10° from it).

2.1.2. Coarse-grained eclogite (SNW3)

The sample of coarse-grained eclogite comes from the Newlands kimberlite pipe in South Africa and belongs to mantle xenoliths that were brought to the surface by kimberlite eruptions. The temperature of equilibration was

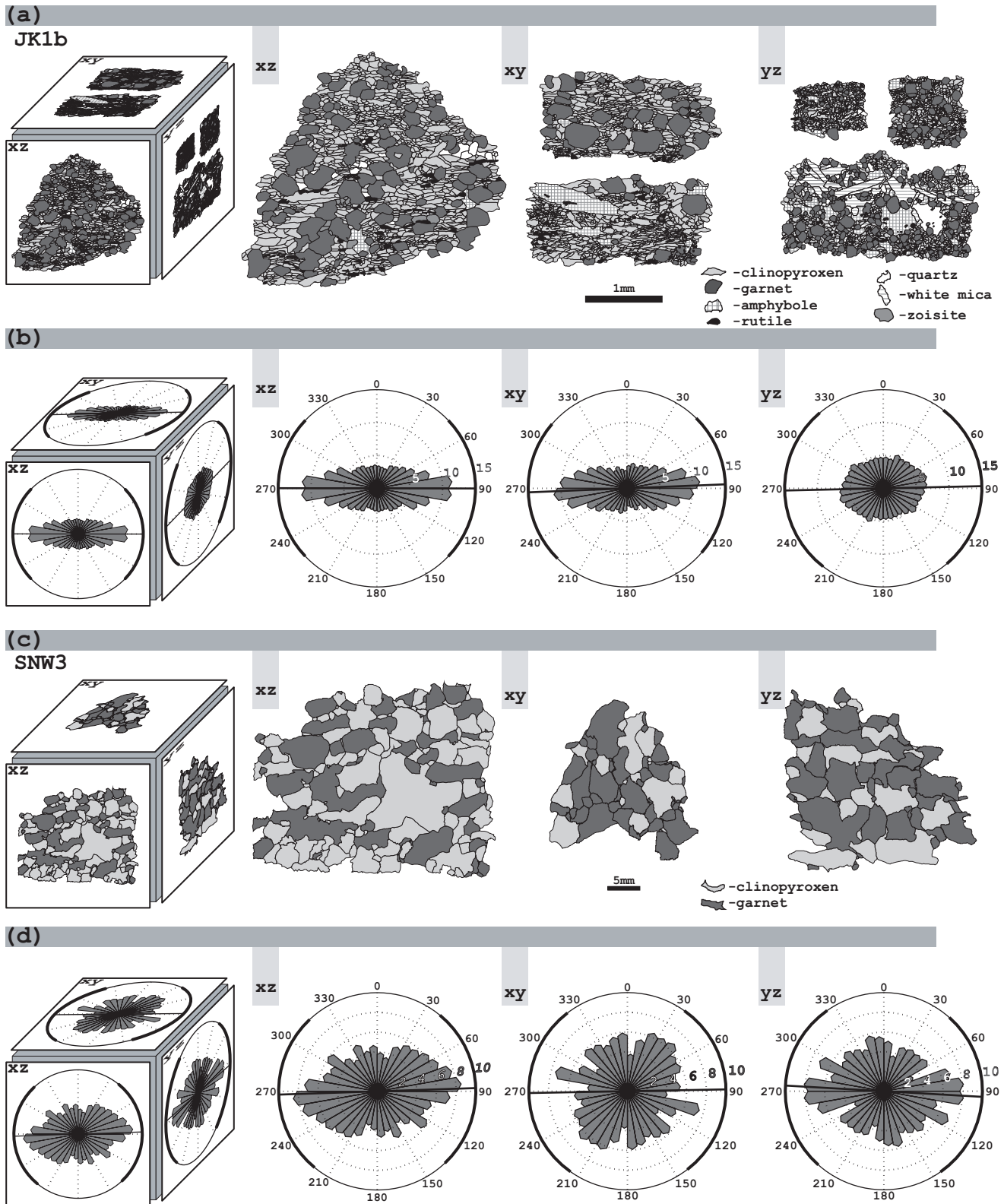


Figure II.2. Digitized microstructure and rose diagrams of grain boundary orientation of all phases of sample JK1b (a, b) and sample SNW3 (c, d) obtained from sections parallel to XZ, YZ and XY planes of finite strain ellipsoid. Therefore foliation is horizontally oriented and lineation is in this plane in E-W direction.

estimated at 1060° - 1100°C (Gurney and Menzies. 1998). The eclogite is coarse-grained with an equilibrated microstructure, well developed macroscopic foliation and consists of slightly elongated garnet and clinopyroxene grains (Fig. II.1b). Clinopyroxene represents 56 % of volume fraction of the rock and the grain size ranges between 0.067 mm and 10.80 mm with a mean Feret diameter of 1.31 mm. Garnet represents 44 % of volume fraction of the rock and grain size ranges between 0.002 mm and 7.89 mm with a mean Feret diameter of 2.20 mm. The mean axial ratio of clinopyroxene and garnet ranges from 1.75 in XY section to 1.96 in XZ section and from 1.80 in YZ section to 2.05 in XZ section, respectively (Table II.1). The distribution of grain boundaries suggests plain strain fabric with weak preferred orientation in XZ and YZ sections with eigenvalue ratios 1.29 and 1.22, respectively, and almost no preferred orientation in XY section (eigenvalue ratio of 1.05). The grain boundary fabric is parallel to macroscopic foliation in this sample.

2.2. Lattice preferred orientation

Lattice-preferred orientation (LPO) was measured on a FEG scanning electron microscope (LEO Gemini 1530) by electron backscatter diffraction (EBSD) technique. In the JK1b sample, an area of 1.5 by 1.5 mm² was measured with a step size of 10 µm. Due to the large grain size in sample SNW3, two areas of 745 and 600 µm² were measured with a step size of 250 and 200 µm, respectively. The large differences in measured areas and step sizes take into account the largely different grain sizes in the two samples so that the actual number of grains measured in each sample are about equal. For both samples thin sections oriented parallel to the XZ plane of the finite strain ellipsoid were used for the texture measurements (Fig. II.3).

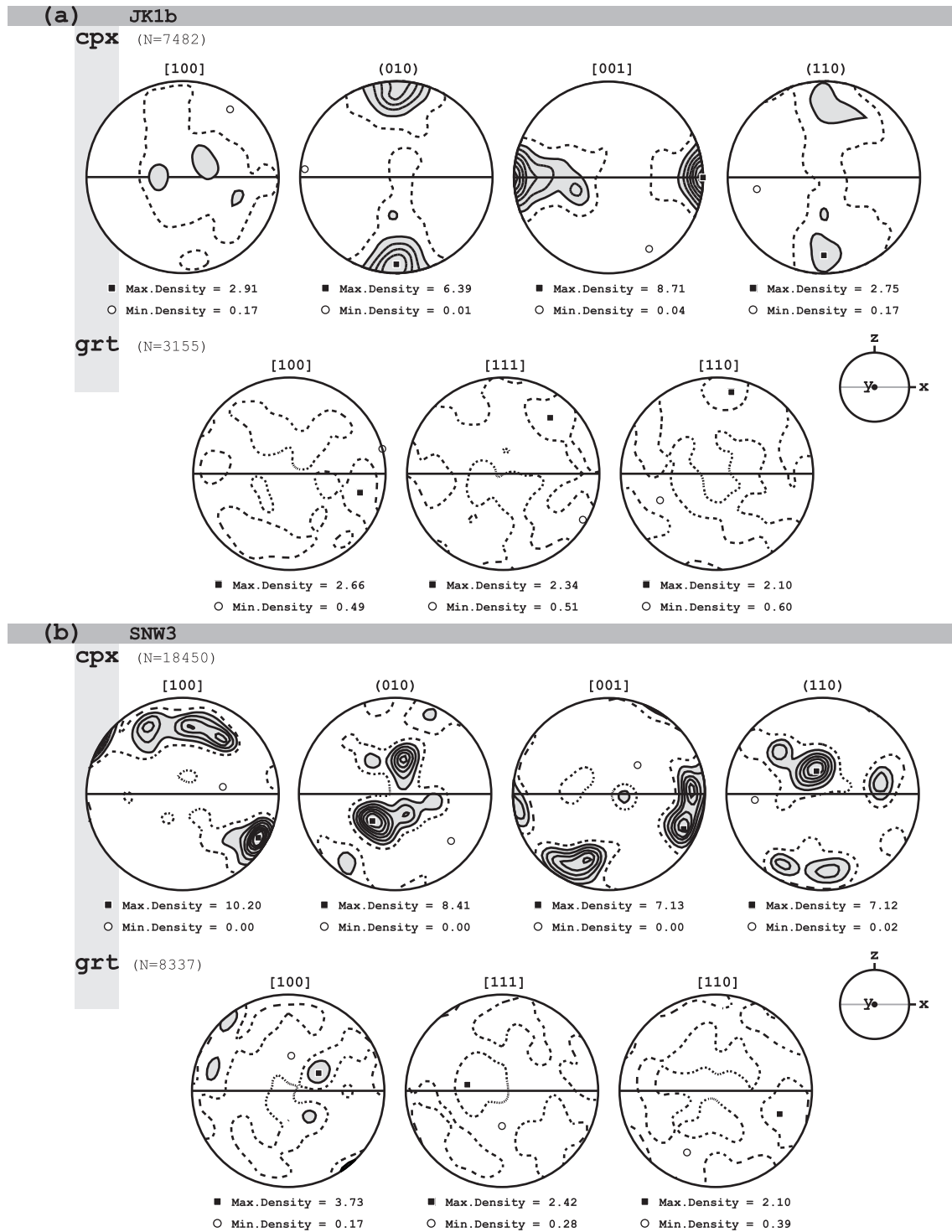


Figure II.3. Clinopyroxene and garnet LPO of sample JK1b (a) and SNW3 (b) measured using the EBSD technique. Equal area projection, lower hemisphere. Contoured at interval 1.0 times of uniform distribution. Foliation (full line) is horizontal and lineation is in this plane in E-W direction. Number of points for each set of pole figures is noted as N.

2.2.1. Fine-grained eclogite (JK1b)

The LPO of clinopyroxene is characterized by a strong concentration of (010)-poles perpendicular to the foliation plane and by strong concentration of [001]-axes in the foliation and parallel to the lineation (Fig. II.3a). [100]-axes are weakly concentrated close to Y axis of finite strain ellipsoid. Poles to (110) cleavage planes of clinopyroxene are concentrated in the girdle normal to lineation and foliation having two main maxima, both oriented about 60° oblique to the foliation plane. The LPO of garnet shows generally very weak density of principal crystallographic directions [100], [110] and [111]. Values of maximum density do not exceed 3 multiples of uniform distribution in any pole figure and values of minimum density are relatively high (Fig. II.3a). These results together with idiomorphic shapes of grains suggest that garnets have no LPO.

2.2.2. Coarse-grained eclogite (SNW3)

The LPO of clinopyroxene is characterized by a concentration of (010)-poles forming a girdle inclined 70° relative to the foliation plane with clearly defined maximum close to the Y-axis of finite strain ellipsoid (Fig. II.3b). [001]-axes form one maximum close to the lineation and another one which is inclined 70° to the foliation plane. The maximum density of [100]-axes is inclined 30° from the lineation in the XZ plane. A second maximum of [100]-axes is elongated and occurs oblique to the foliation plane. Poles to (110) cleavage planes show strong maximum inclined 15° from the centre of the pole figure and several weaker maxima. Such LPO with second point maximum of [001] axes located oblique to foliation plane at the margin of the pole figure does not belong to any known LPO type of clinopyroxene. The LPO of garnet in this sample is similarly weak as that in the sample JK1b. The strongest density (3.73) occurs in the pole figure of [100]-axes due to the lowest multiplicity in the crystal structure compared to [110] and [111], which is in agreement in the number of submaxima observed in all three

pole figures (Fig. II.3b). The observed weak lattice preferred orientation of garnet is in agreement with the large number of slip systems available in the garnet cubic structure (Mainprice et al., 2004).

2.3. Anisotropy of P-wave velocities

P-wave velocity measurements have been carried out by means of the pulse transmission technique using the apparatus designed at the Institute of Geophysics ASCR in Prague for the measurement of spherical samples (Pros and Babuška, 1968; Pros et al., 1998).

2.3.1. Fine-grained eclogite (JK1b)

At minimum confining pressure (0.1 MPa), directions of high velocities form a wide belt parallel to macroscopic foliation and a broad maximum deviated by 20° from lineation direction in the foliation plane. Directions of low velocities form two strong maxima inclined about 25° to the pole of foliation (Fig. II.4a). The third maximum of low velocities is weaker and located close to lineation. At maximum confining pressure of 400 MPa, the directions of high velocities form an incomplete girdle along foliation with the maximum in the lineation, whereas the velocity minimum is perpendicular to foliation (Fig. II.4a). The spatial distribution of P-wave velocities progressively changes with increasing confining pressure with the main change between 50 MPa and 100 MPa (Fig. II.4a). Nearly the same change can be observed during decreasing pressure between 100 MPa and 50 MPa (Fig. II.4a). Maximum and minimum velocities at the highest confining pressure of 400 MPa are 8.1 kms⁻¹ and 7.7 kms⁻¹, respectively. The coefficient of anisotropy k is 22.4 % at 0.1 MPa and decreases with increasing confining pressure to 5.1 % at 400 MPa.

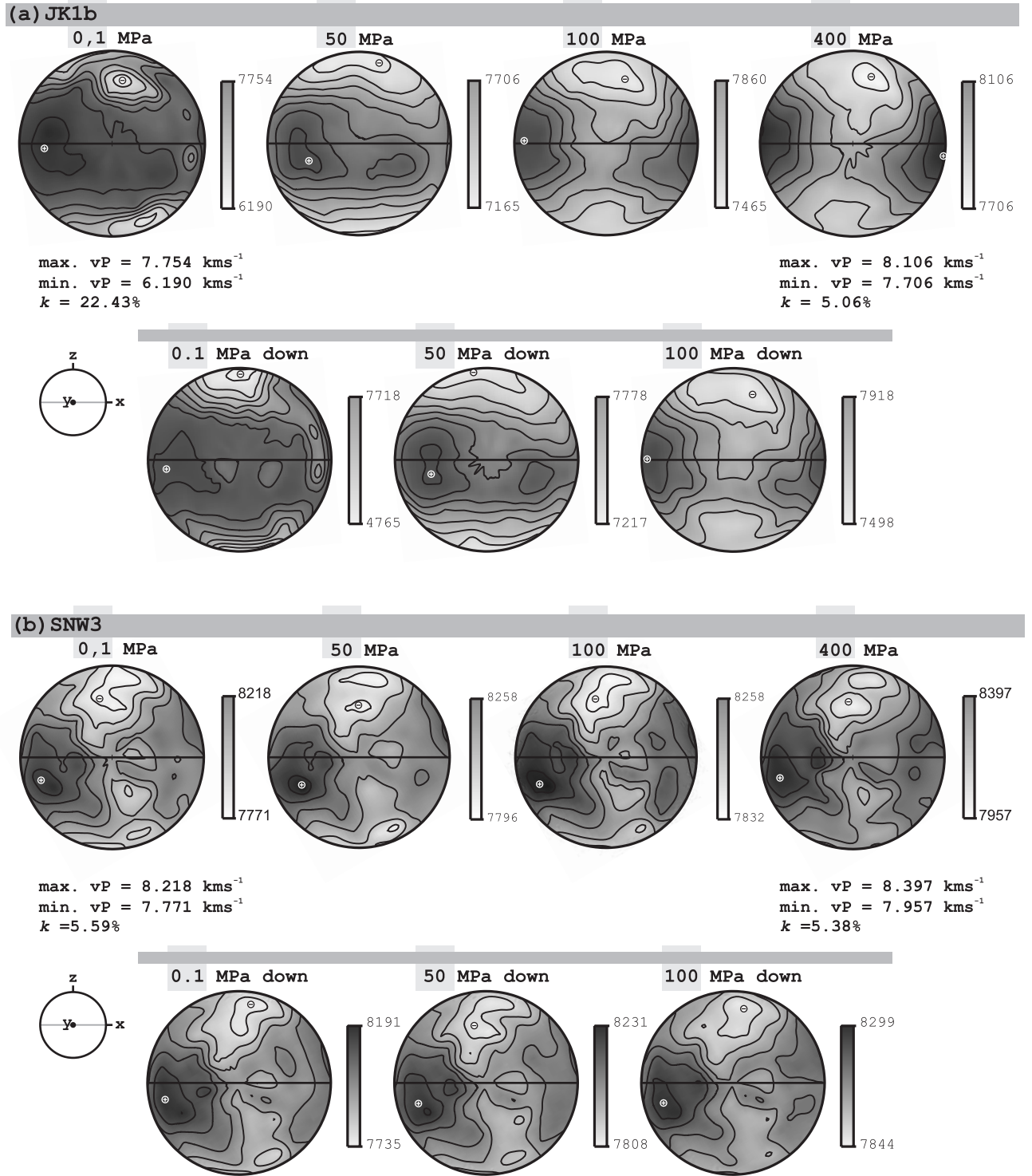


Figure II.4. Results of measurements of P-wave velocity spatial distribution in sample JK1b (a) and sample SNW3 (b) at pressure levels 0.1, 50, 100, 400 MPa for increasing and decreasing pressure path. Diagrams are in the form of velocity isolines projected onto the lower hemisphere, equal area projection. The directions of maximum and minimum of P-wave velocities are noted by signs plus and minus. Foliation (full line) is horizontal and lineation is in this plane in E-W direction.

2.3.2. Coarse-grained eclogite (SNW3)

At minimum confining pressure, directions of both high and low velocities form broad maxima around 20° out of lineation and normal to foliation, respectively. There is no visible change in position of directions of maximum and minimum velocities with increasing confining pressure. The coefficient of anisotropy k at 0.1 MPa is 5.6 %. and slightly decreases to 5.4 % at 400 MPa, maximum and minimum velocities at the highest pressure are 8.4 kms-1 and 8.0 kms-1, respectively (Fig. II.4b).

2.4. Orientation of microporosity

The spatial distribution of micropores has been investigated using the 3D analysis of differences between P-wave velocities measured at various confining pressures, i.e. describing the ΔV_P (Δp) dependence in space. The $\Delta V_P(\Delta p)$ dependence has been studied for each pair of subsequent sets of 3D measurements in order to evaluate progressive closure of individual sets of microporosity. Results are shown in Fig. II.5. together with bulk difference of V_P between 0.1 and 400 MPa. To compare the degree of preferred orientation of microporosity and the relative amount of open space in the studied rocks, the anisotropy of P-wave velocity difference, a , between confining pressures of 400-0.1 MPa, 400-100 MPa and 100-0.1 MPa and the mean of ΔV_P were calculated.

2.4.1. Fine-grained eclogite (JK1b)

The bulk ΔV_P between 400 and 0.1 MPa shows a pattern which is virtually an inverse to V_P distribution at 0.1 MPa (Fig. 4a). Two main maxima (areas A and B in Fig. II.5a) are located approximately 20° out of the normal to foliation plane, and another, subsidiary maximum of ΔV_P is oriented close to the direction of lineation (area C) (Fig. II.5a). In the ΔV_P diagram for 10-0.1 MPa, two maxima corresponding to areas A and B are visible. For

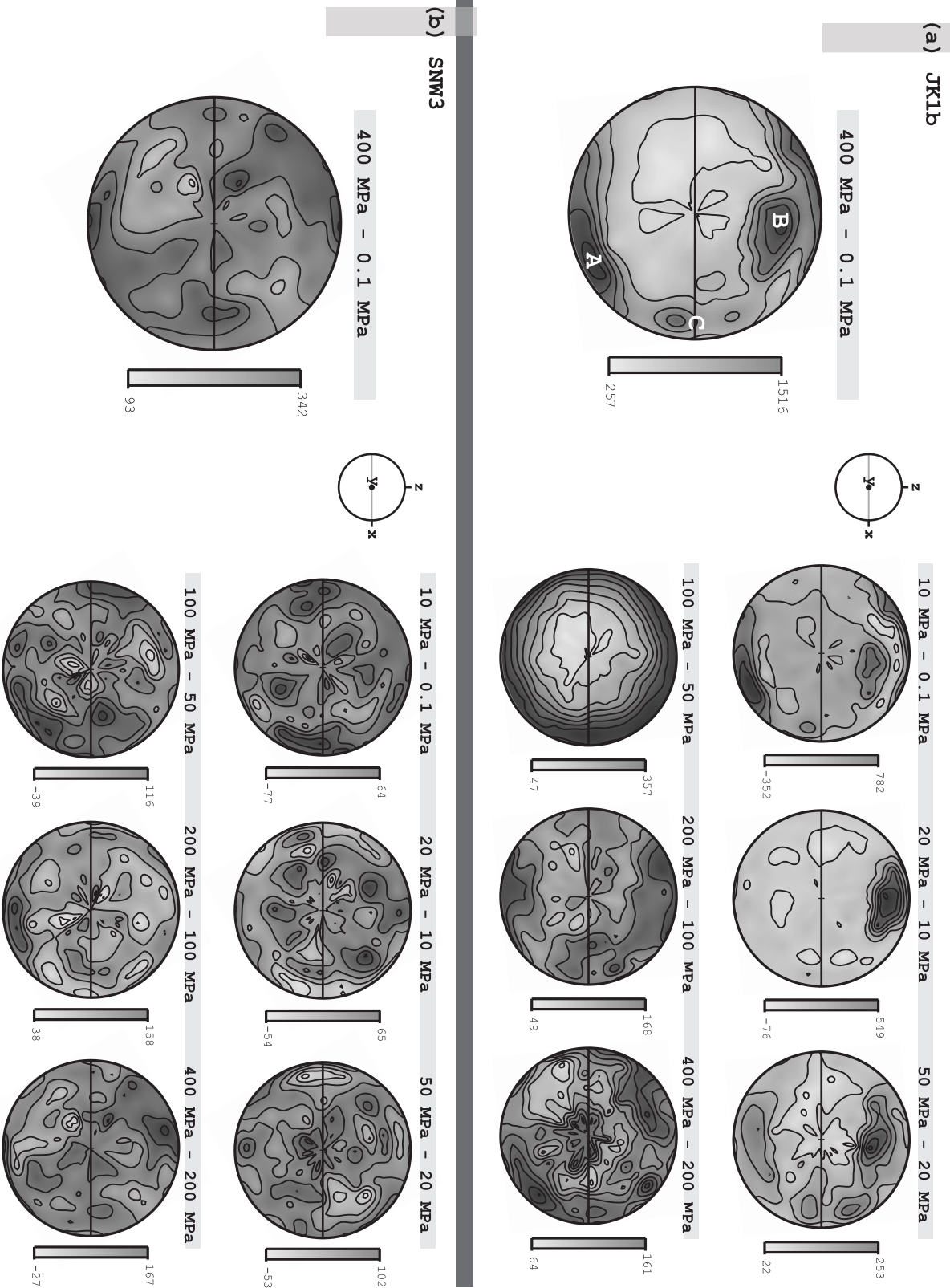


Figure II.5. Stereodiagrams of the $\Delta V_p(\Delta p)$ dependence in space for samples JK1b (a) and SNW3 (b). It shows diagrams of each pair of subsequent sets of 3D measurements together with bulk difference of V_p between 0.1 and 400 MPa. Orientation of foliation and lineation is same as in figure II.4.

the pressure level of 20-10 MPa, the ΔV_P diagram shows a combination of the areas A and B forming single maximum. Between 50 and 20 MPa, a strong maximum of P-wave velocity differences is located in area B. Other two submaxima are oriented close to a direction of lineation (near area C). The values of maxima in partial ΔV_P diagrams are decreasing with increasing confining pressure from 0.8 kms^{-1} to 0.3 kms^{-1} . The anisotropy of V_P difference a between 400 and 0.1 MPa is 15.5 % and the mean ΔV_P is 0.6 km^{-1} . Partial ΔV_P diagrams indicate that most microporosity of the set corresponding to the area A closed down between 0.1 and 20 MPa. Most microcporosity corresponding to the area B and C closed between 0.1 and 50MPa. (Fig. 5a)

2.4.2. Coarse-grained eclogite (SNW3)

In the sample SNW3, the bulk ΔV_P between 400 and 0.1 MPa shows three approximately orthogonally located maxima: the first normal to foliation plane, the second about 30° from the centre of the diagram in the foliation plane and the third about 30° from the lineation direction in the foliation plane (Fig. II.5b). All partial ΔV_P diagrams show neither strong individual maxima or minima nor progressive lowering of absolute maximum value of ΔV_P within the individual pressure levels (Fig. II.5b). There are several partial maxima and minima in ΔV_P diagram, whose position changes with pressure, and surprisingly, the absolute values of maximum ΔV_P slightly increase with increasing confining pressure. However, all these values are close to the estimated value of error of experimental measurement. The V_P difference anisotropy a between 400 and 0.1MPa is 3.0 % and the mean ΔV_P is 0.2 kms^{-1} .

2.5. Discussion

The spatial distribution of P-wave velocities at 400 MPa is more or less similar in both samples and corresponds well to the observed lattice pre-

ferred orientation (LPO) of clinopyroxene (Figs. II.3 and II.4). The LPO of clinopyroxene in the fine-grained sample JK1b is characterized by a strong concentration of c-axes [001] in the direction of stretching lineation. The direction of high P-wave velocities is also oriented close to the lineation, which can be correlated to the single crystal model of P-wave velocities in clinopyroxene. The more diffuse orientation of directions of high P-wave velocities and the oblique orientation of the maximum velocity with respect to foliation in the sample SNW3 can be probably explained by the presence of clinopyroxene c-axes sub-maxima declining 70° from the foliation plane. In spite of the abundance of garnet, it does not influence the directional dependence of velocity due to its high symmetry and low elastic anisotropy (e.g. Babuška et al., 1978). In both samples, the P-wave velocity and its anisotropy are in the range of observations in eclogites from other orogens (Fountain et al., 1994; Kumazawa et al., 1971; Mauler et al., 2000). However, the presence of about 13% of randomly oriented mineral phases with lower P-wave velocity as amphibole, quartz, paragonite and zoisite are very likely the main reason for the lower measured velocities.

The evolution of the spatial distribution of P-wave velocities with increasing pressure is different in both samples. In the coarse-grained sample SNW3, the spatial distribution of P-wave velocities at 0.1 MPa is similar to that observed at 400 MPa. The maximum and minimum velocities (8.2 km s^{-1} and 7.8 km^{-1} , respectively) are only slightly lower compared to the values obtained at maximum pressure conditions. Also, the degree of anisotropy shows only a very small difference between maximum and minimum pressure conditions (Fig. II.4b). On the contrary, the differences between the velocities obtained at 400 and 0.1 MPa are much more significant in the fine grained sample. The major change of spatial distribution of the P-wave velocities takes place between 50 and 100 MPa as can be seen in the differential diagram in Fig. II.5a. The difference between the spatial distribution of P-wave velocities in the sample JK1b obtained at maximum and minimum confining pressure is likely caused by preferentially oriented microporosity.

The important effect of microporosity on P-wave velocities and their spatial distribution at low confining pressures is indicated by high degree of anisotropy ($k = 22.4 \%$) and low values of maximum and minimum velocity measured at atmospheric pressure (7.8 kms^{-1} and 6.2 kms^{-1} , respectively).

In the sample JK1b, the microporosity is preferentially oriented in two main directions, denoted as areas A and B in Fig. II.5a. Individual differential diagrams show that the pores corresponding to the area A are closed at lower pressures (20 MPa) than the pores corresponding to the area B, whilst the majority of pores are closed above 50 MPa. This indicates the presence of several types of microporosity with different response to confining pressure (cf. Babuška and Pros, 1984; Siegesmund and Vollbrecht, 1991). The most probable microscopic features responsible for oriented microporosity in this sample are grain boundaries and cleavage planes in clinopyroxene. There are other minerals having cleavage planes in the sample, but they are much less abundant than clinopyroxene and they are not preferentially oriented. The quantitative microstructural analysis shows a strong constrictional fabric of grain boundaries with the largest population oriented subparallel to the foliation plane (Fig. II.2a.b). Lattice preferred orientation shows the (110) cleavage planes concentrated in the girdle normal to lineation having two maxima, both oriented about 60° from the foliation plane (Fig. II.3a). These data suggest that the area A in Fig. II.5a may correspond to grain boundaries parallel to foliation plane and the area B most likely corresponds to the cleavage planes. In this sample, the grain boundaries were therefore closed prior to the cleavage planes as a result of increasing confining pressure.

In the second sample, SNW3, the microporosity forms three orthogonally oriented maxima as seen in the differential diagram in Fig. II.5b. Nevertheless, no systematic evolution of microporosity orientation with increasing pressure was observed. The quantitative microstructural analysis of the sample SNW3 shows a weak plane strain fabric of grain boundaries, with the strongest preferred orientation parallel to the foliation plane (Fig.

II.2c,d). The determined preferred orientation of cleavage planes (110) in clinopyroxene shows a strong maximum inclined 15° away from the Y-axis of strain ellipsoid and two other weaker maxima (Fig. II.3b). All three maxima correspond well with the orientation of maxima in the differential diagrams of V_P . This seems to indicate that the open space along the cleavage planes in clinopyroxene represents a major part of the microporosity and the grain boundaries contribute to the bulk porosity only in the direction perpendicular to the foliation plane.

The mean and the anisotropy of P-wave velocity differences were calculated to assign the relative amount of microporosity and the degree of its preferred orientation. The mean P-wave velocity difference is 0.6 kms^{-1} in the fine-grained sample JK1b and 0.2 kms^{-1} in the coarse-grained sample SNW3. The anisotropy of bulk microporosity reached 15.5% in fine-grained sample JK1b and 2.9% in coarse-grained sample SNW3. These data suggest that in the sample JK1b the microporosity is relatively large and strongly preferentially oriented, in contrast to the sample SNW3 in which it is significantly lower and weakly oriented. This is in agreement with the assumption that the grain boundaries are the most important carriers of microporosity in eclogites. The orientation of microporosity thus seems to depend mostly on the preferred orientation of grain boundaries and rather less on the orientation of (110) cleavage planes in clinopyroxene.

We assume that micropores which are preferentially oriented parallel to grain boundaries (grain boundary porosity) have a shape of planar cracks in our samples, since their closing at higher pressures leads to a change (decrease) of velocity anisotropy. It is very likely that the micropores parallel to the (110) clinopyroxene cleavage planes also have the shape of planar cracks. So we suggest that grain-boundary cracks and cleavage cracks parallel to the (110) clinopyroxene planes are responsible for the main part of microporosity. Such microcracks and corresponding porosity have been most probably formed during exhumation process, as an inelastic response to the decrease of lithostatic stress and an elastic mismatch between grains.

2.6. Conclusions

Using a combination of three independent research methods - microstructural analysis, measurement of lattice preferred orientation and 3-D measurement of elastic P-wave velocity - we were able to document the pressure-dependent behavior and distinguish the differences of two main anticipated carriers of microporosity in two samples of eclogite – crystal cleavage and grain boundaries.

The following main observations were made:

1. Microporosity in fine-grained and coarse-grained eclogites is related to grain boundaries and cleavage planes in clinopyroxene.
2. In the fine-grained sample, the microporosity is relatively large and strongly preferentially oriented. The grain boundaries oriented parallel to the foliation plane contribute mainly to the bulk microporosity.
3. In the coarse-grained sample, microporosity is relatively low and weakly preferentially oriented. The cleavage planes in clinopyroxene are responsible for the main part of preferentially oriented microporosity.
4. The grain boundaries have much stronger influence on orientation and amount of microporosity than the cleavage planes in both samples.
5. With increasing confining pressure, grain boundaries close below 50 MPa, while cleavage planes in clinopyroxene remain open up to 100 MPa. Orientation of microporosity mostly depends on preferred orientation of grain boundaries and somewhat less on orientation of cleavage planes in clinopyroxene. We conclude that grain-boundary cracks and cleavage cracks parallel to clinopyroxene (110) planes are responsible for the main part of microporosity.

3. Relation of pore space geometry, permeability and microstructure of three granite types

co-authors: Petr Špaček, Ondrej Lexa, David Mainprice, Stanislav Ulrich

In this chapter, we investigate relations between the pore space geometry, permeability, microstructure and structure of granitic rocks collected in the Melechov granite in the central part of the Variscan Bohemian Massif. This small post-orogenic granitic body experienced only a very weak deformation during the last 315 Ma since its formation. It is also for this reason that the Melechov massif has been lately established a testing locality for the radioactive waste repository by state authorities of the Czech Republic. In the study we combined indirect and direct methods to study pore space geometry and its relationship to microstructure, elastic properties of granitic specimens and already studied brittle structure of the Melechov granite by Lexa and Schulmann (2006). The framework of the study is based upon the measurements of P-wave velocities (V_P) and analysis of spatial distribution of ΔV_P (Δp) (difference of P-wave velocity measured at two different levels of confining pressure in a certain direction). The pore space geometry established by velocity measurements is confronted with the results of quantitative analysis of microstructure and measurements of permeability of selected samples. Samples were taken from surface outcrops (quarry walls or natural outcrops) with respect to macroscopic brittle structures observed on outcrops (called “reference plane” in the following

text). Direction-dependent velocity of acoustic P-waves measured on spherical samples under changing confining pressure was used as a tool to investigate the overall pore space geometry. The porosity and the permeability study have been carried out using the “steady state flow” method. Two test cylinders oriented according to results of P-wave velocity measurements were prepared from each sample. Permeability tests were carried out on each cylinder at 3 different levels of effective pressure. Samples were subjected to a quantitative microstructural analysis from three sections in each sample corresponding in orientation to the results of P-wave velocity measurements.

3.1. Geological background and structure of the Melechov Massif

The Melechov massif forms the northern-most part of the Moldanubian Batholith, separated from the rest of the batholith by metamorphic rocks of the so-called Monotonous and Varied unit of the Moldanubian zone of the Bohemian Massif (Fig. III.1a). The Moldanubian Batholith is a product of an intrusion of large volume of crust-derived magma into the internal domain of the Variscan orogen during and after the thermal peak of regional metamorphism. The high-resolution U–Pb geochronology indicates that the batholith in general was formed during ~331–323 Ma (Gerdes et al., 2003). The host rock of the batholith comprises mainly paragneisses, migmatized paragneisses, and migmatites of the Monotonous Group (Vrána, 1988; Vrána et al., 1995). The Melechov massif consists of a series of per-aluminous two-mica granite intrusions subdivided into four granite types forming concentric zoning from the Stvořidla type in the centre towards Melechov, Kouty, and Lipnice type on the rim (Fig. III.1a). The central part formed by the fractionated Melechov and Stvořidla types has presumably a common deep-seated crustal source compared to the Lipnice and Kouty granites, originated from the in situ partial melting of the local paragneisses

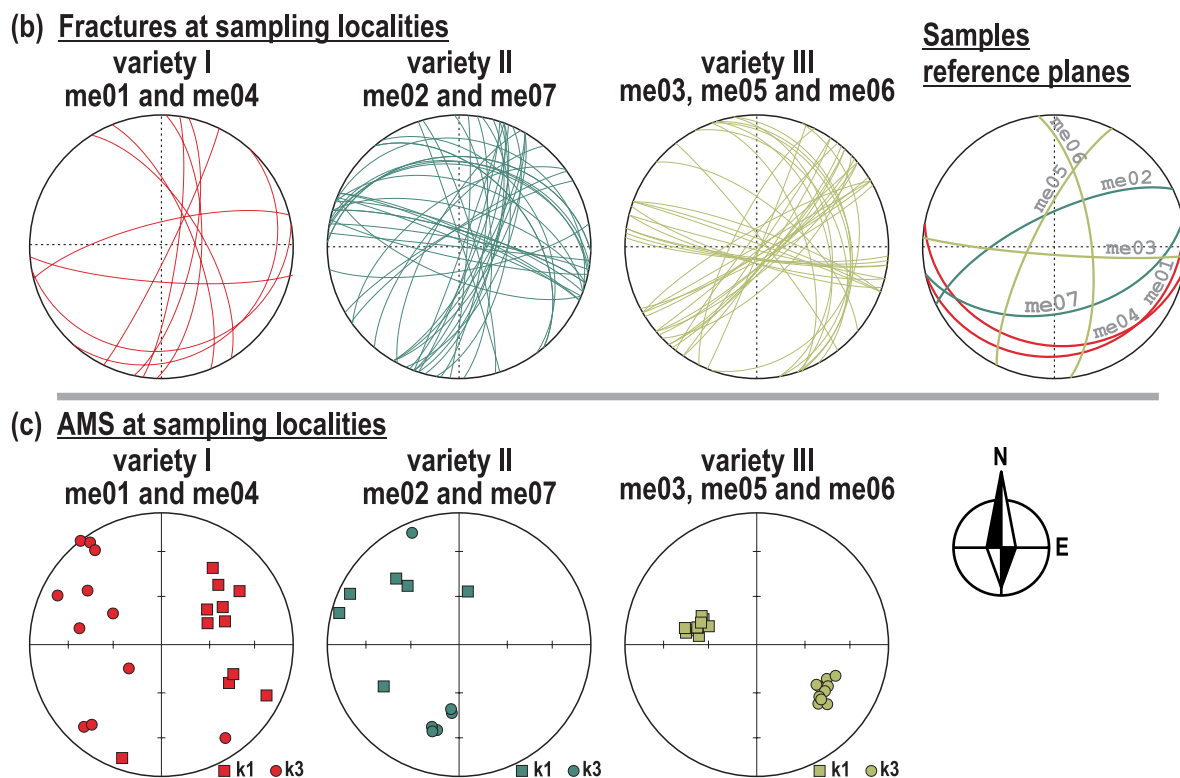
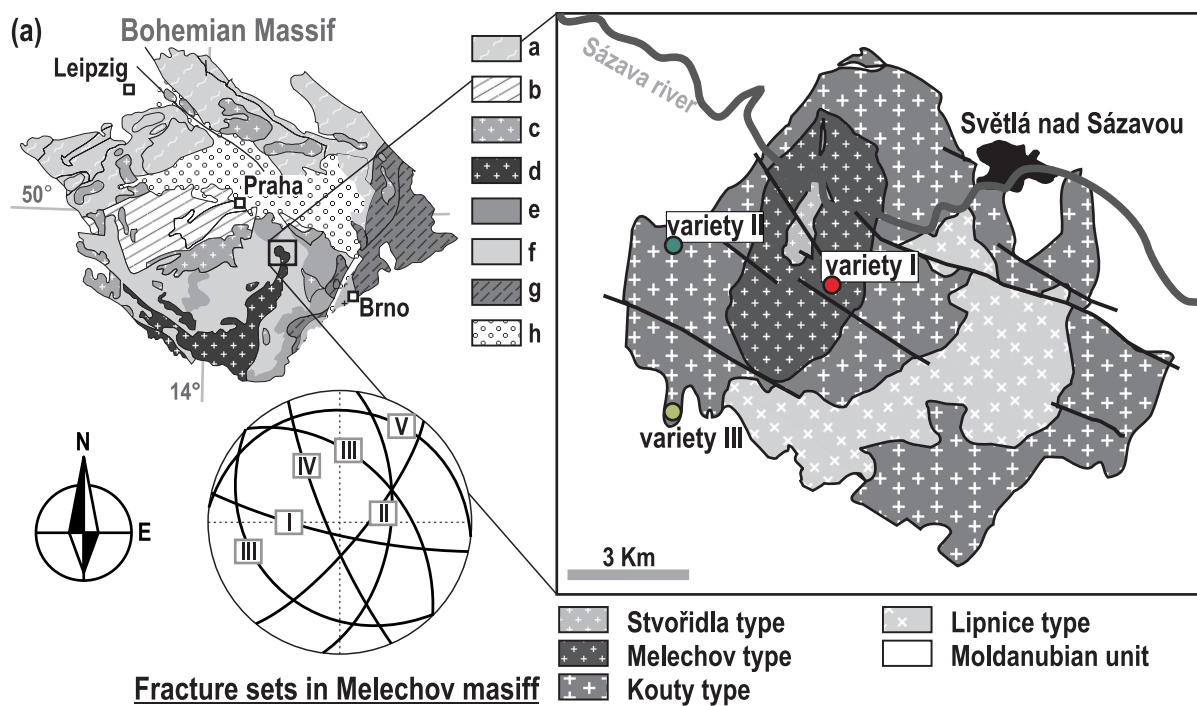


Figure III.1. (a) The location of the study area, simplified geological map of the Bohemian Massif (modified after Franke 2000) (a- Saxothuringian and Lugian, b- Teplá-Barrandian, c- Variscan granitoids, d - Moldanubian Batholith, e - Gföhl unit, f - Varied and Monotonous unit, g - Brunovistulian, h - Cretaceous sedimentary cover) and geological map of Melechov granite and fracture sets recorded in Melechov granite by Lexa et al. (2005). (b) Orientation of fractures at sampling localities and geographical orientation of reference planes. (c) AMS record at sampling localities.

(Breiter et al., 1998; Procházka and Matějka, 2006). The chemical ages (Th, U, Pb microprobe analysis in monazite) suggest that the intrusion of all granite types in the range 313–317 Ma occurred about 10 Ma later than intrusion of the southern part of the Moldanubian Batholith (Gerdes et al., 2003). Mineral assemblages at the contact with the paragneiss suggest that the emplacement of granites in the Melechov massif occurred at about 500 MPa and 670–750°C (Schulmann et al., 1998). The brittle structure of the Melechov massif has been studied recently by Lexa & Schulmann (2006) who distinguished five main fracture sets (Fig. III.1a): Sets I and II form the primary post-magmatic joint system reflecting regional extensional stress regime. Set I is formed by large WNW-ESE trending steep joints and set II forms smaller steep joints trending in the NNE-SSW direction. Set III represents shear fractures developed in the regional stress regime during cooling of the granite massif; it forms conjugate set of fractures dipping under medium to low angles in NE and SW directions. Set IV is formed by steep N-S to NNW-SSE oriented shear fractures of tectonic origin related to large N-S faults documented in the area. This fracture set is probably the youngest as it cuts through all other sets including the last set V, formed by subhorizontal exfoliation planes. The fracture network in the Melechov massif was reactivated by three tectonic events. First two events acted in the strike-slip mode. First event has reactivated sets I, II and III with the maximum stress oriented NW-SE. The second event with the maximum stress oriented NE-SW has produced fracture set IV and reactivated set II. The last reactivation occurred as an ESE-WNW extension, which has reactivated fracture set III.

3.2. Description of samples

In the Melechov massif, we collected 7 samples of three microstructural varieties of the Melechov and Kouty granite types. Microstructural varieties differ mainly in grain size and partly in mineral composition (Table

III.1). Microstructural variety I (samples me01 and me04) is a coarse-

Table III.1 Microstructural analysis of grains

		Quartz	Plagioclase	K-feldspar	Mica	Other	All
Variety I	%	38.6	26.4	23	11.1	0.9	100
	d [mm]	1.6	1.5	2.5	1.2	1	1.5
Variety II	%	33.7	23.3	33.5	8.5	1.1	100
	d [mm]	1	0.9	1.4	0.6	0.5	0.9
Variety III	%	34	36.2	20.3	8.6	0.9	100
	d [mm]	0.8	0.8	1	0.6	0.5	0.7

d - feret diameter in mm

grained granite of the Melechov type composed of 39% quartz, 26% plagioclase, 23% K feldspar, 11% micas and 1% other accessory phases. The average grain size of variety I is 1.5 mm. Samples of variety I were collected from natural outcrops at a locality where fractures of sets I, II, IV and V were recorded (Fig. III.1b). The most pronounced structures at this locality are subhorizontal exfoliations that have been used as a reference plane for sampling. Microstructural variety II (samples me02 and me07) is a medium-grained granite of the Kouty type composed of 34% quartz, 23% plagioclase, 34% K feldspar, 9% micas and 1% other accessory phases. The average grain size of variety II is 0.9 mm. Samples of this variety were collected from quarry walls at a locality where all fracture sets occur (Fig. III.1b). Samples were taken with respect to set I fracture (sample me07) and set II fracture (sample me02). Microstructural variety III (samples me03, me05 and me06) is a fine-grained granite from the Kouty type composed of 34% quartz, 36% plagioclase, 20% K feldspar, 9% micas and 1% other accessory phases. The average grain size of variety III is 0.7 mm. Samples of variety III were collected from quarry walls at a locality where fracture sets I, II and III predominate (Fig. III.1b). Samples were taken with respect to set I fracture (sample me03) and set II fracture (samples me05 and me06).

3.2.1. Magmatic fabric

Magmatic fabric is characterized by anisotropy of magnetic susceptibility (AMS) measurements. The AMS is measured on cylindrical samples from

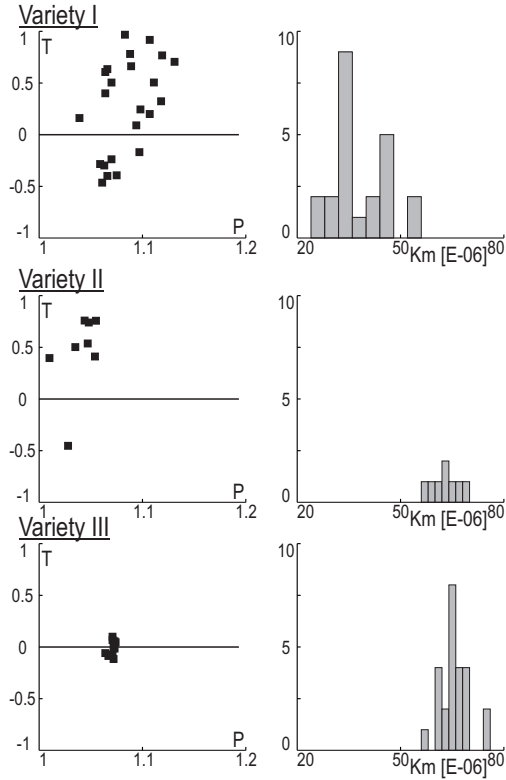


Figure III.2. The P - T graphs representing the shape and degree of AMS fabrics and histogram of mean magnetic susceptibility K_m for each sampling locality.

At the variety I locality the AMS is characterized by scattered distribution of subvertical to medium angle magnetic foliations (perpendicular to k_3) dipping in directions from NE to SE (Fig. III.1c). Magnetic lineation dips preferential towards NE. The magnetic susceptibility values ranges between 20×10^{-6} and 60×10^{-6} (Fig III.2a). The AMS fabric exhibits low degree of anisotropy ranging from $P = 1.05$ - 1.15 (Fig III.2a). The shapes

sampling localities as well as on spherical samples (5 cm in diameter) used for P-wave velocity measurements. The low field AMS was measured with a KLY-3 Kappabridge and KLY-2 Kappabridge with large air core inductor (spheres) in Agico (Jelínek and Pokorný, 1997) in the field of 300 A/m. Two AMS parameters (Jelínek, 1981) are used to characterize the magnetic fabric defined by principal magnetic susceptibilities $k_1 \geq k_2 \geq k_3$. The intensity of preferred orientation of magnetic minerals was indicated by the degree of anisotropy $P = k_1/k_3$. The character or symmetry of the magnetic fabric was defined by the shape factor $T =$

of AMS ellipsoid are dominantly oblate with few data points in the prolate field of the P-T plot (Fig III.2a). The AMS of spherical samples of variety I (me01 and me04) do not show systematic orientation in relation to sample reference plane (Fig. III.3).

The AMS at locality of variety II reveals very weak oblate fabric ($P = 1.01-1.06$) (Fig. III.2b) showing magnetic foliation dipping under medium angles towards N with scattered orientation of lineation (Fig III.1c).

AMS of spherical samples

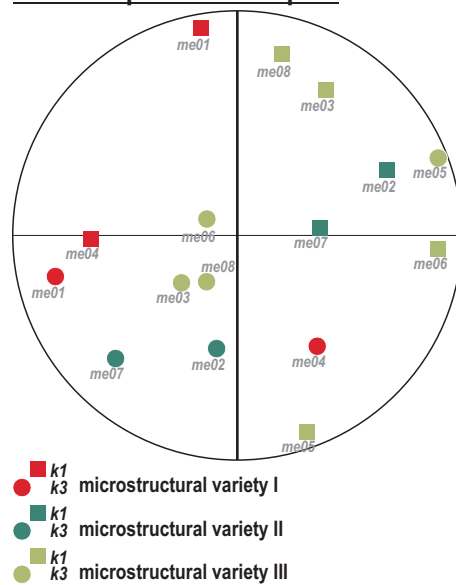


Figure III.3. AMS of spherical samples used for P-wave velocity measurements.

The values of magnetic susceptibility range at variety II locality around 60×10^{-6} (Fig III.2b). Spherical samples of variety II (me02 and me07) exhibits AMS characterized by orientation of k3 principal susceptibility about 40° degrees oblique to samples reference plane (Fig. III.3). At sampling locality of the fine grained microstructural variety III the AMS shows magnetic foliation dipping towards NW under medium angles with lineation in dip direction of foliation. The magnetic susceptibility values ranges between 60×10^{-6} and 80×10^{-6} (Fig III.2c). The AMS fabric exhibits low degree of anisotropy around $P = 1.07$ and weakly oblate shapes with few data points in the prolate field (Fig III.2c). Spherical samples show AMS fabric orientation its degree and shape similar to those obtained from cylindrical samples at sampling localities and do not shows regular relation to reference planes of individual samples (Fig. III.3). Values of magnetic susceptibility together with degree of anisotropy and shapes of AMS ellipsoids suggest that the magnetic fabric is formed by relatively weak biotite alignment that is usually observed in magmatic rocks lacking significant solid-state deformation (Bouchez. 2000).

3.3. Anisotropy of p-wave velocity and pore space geometry

At minimum confining pressure (10 MPa), the P-wave velocity distribution is characterized in all samples by one significant minimum. Which is oriented either perpendicular (variety I) or about 20 - 40° off the reference plane towards the horizontal position (variety II and III) (Fig. III.4). High velocities form either girdle or single concentration perpendicular to the orientation of the minimum velocity. The velocity distribution gradually changes with increasing confining pressure, and becomes more scattered at 400 MPa with several submaxima and subminima (Fig. III.4). The scattering takes place between confining pressures of 100 and 200 MPa. In the case of the variety I, the position of maximum and minimum is close to their respective orientations at minimum pressure (Fig. III.4). Measured velocities at minimum confining pressure show the largest differences in measured properties with respect to the microstructural variety (Table III.2). The largest difference is related to the values of anisotropy showing markedly the largest values for the variety I (~ 24 %) and the lowest range of values for the variety II (6.8 %– 7.7 %). The fine-grained variety shows medium range of anisotropies ranging from 7.2 % to 13.3 %. Values of measured velocities at minimum confining range between 3.4 and 5.2 km.s⁻¹. being similar for all varieties in the case of maximum observed velocity. Similar observation can be made for velocity values obtained at confining pressure 100 MPa but with minor anisotropy difference among microstructural varieties. The anisotropy drops between minimum pressure and 100 MPa to one half up to one fifth of the original value. The smallest drop shows samples of the variety II. Samples of other two varieties do not show some consistency in anisotropy evolution as they fulfill the drop range (Table III.2). At maximum confining pressure (400 MPa), values for all samples (Table III.2) reach similar velocities ranging from 6.0 km.s⁻¹ to 6.4 km.s⁻¹, with anisotropies being the lowest for samples of the variety II (2.5 and 3.2 %),

Table III.2 Summary of the P-wave velocity measurements

Sample		10 Mpa			100 Mpa			400 Mpa			$\Delta V_p(\Delta p)$ (100 - 10)		
		min V_p (kms ⁻¹)	max V_p (kms ⁻¹)	k (%)	min V_p (kms ⁻¹)	max V_p (kms ⁻¹)	k (%)	min V_p (kms ⁻¹)	max V_p (kms ⁻¹)	k (%)	ΔV_p (%)	ΔV_p (kms ⁻¹)	
Variety I	me01	3.9	5.0	24.3	5.4	6.0	10.7	6.1	6.4	6.3	11.2	1.2	
	me04	3.4	4.3	23.6	5.5	5.8	5.6	6.0	6.3	4.0	13.3	1.7	
Variety II	me02	4.5	4.8	6.8	5.6	5.8	3.4	6.1	6.3	3.2	3.7	1.0	
	me07	4.3	4.7	7.7	5.5	5.8	4.4	6.1	6.2	2.5	4.3	1.1	
Variety III	me03	4.8	5.2	8.3	5.6	5.9	6.3	6.0	6.3	3.6	4.0	0.7	
	me05	4.2	4.8	11.4	5.7	5.9	3.4	6.1	6.3	3.1	7.1	0.9	
	me06	3.9	4.5	13.3	5.8	6.0	4.8	6.1	6.3	3.0	10.6	0.9	

Pressure - confining pressure during experiment, min V_p and max V_p - minimum and maximum velocity, k - velocity anisotropy,

min ΔV_p and max ΔV_p - minimum and maximum of velocity difference, A - anisotropy of velocity difference, ΔV_p - average velocity difference

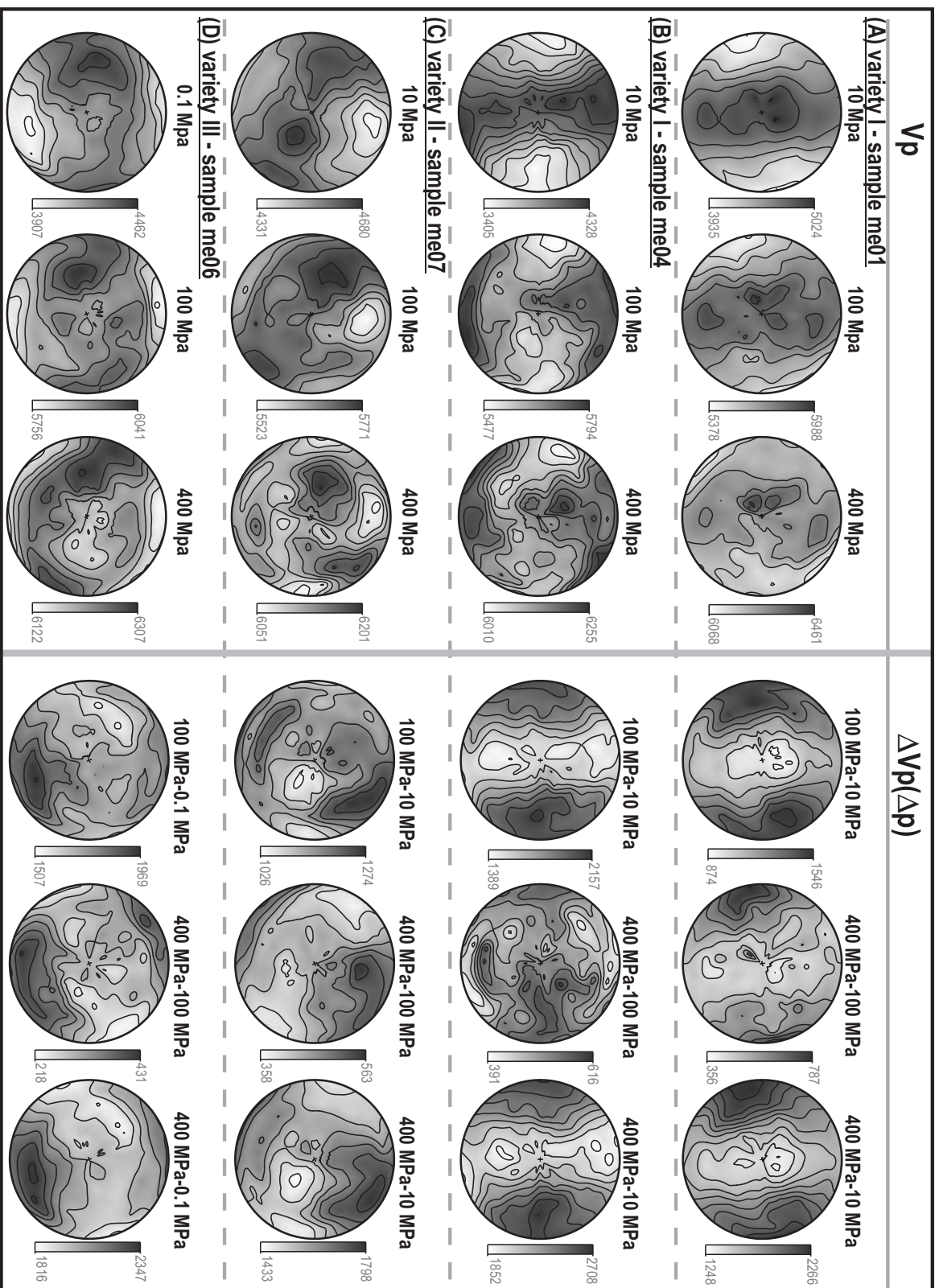


Figure III.4. Results of measurements of P-wave velocity spatial distribution (V_p) and stereodiagrams of the of the P-wave velocity differences ($\Delta V_p(\Delta p)$) dependence in space. Diagrams are in the form of velocity and velocity differences isolines projected onto the lower hemisphere, equal area projection. Reference plane (full line) is oriented in N-S direction with dip direction to the S of the diagram.

moderate samples of the variety III (3.0 - 3.6 %) and the highest for the variety I (4.0 % and 6.3 %). The ΔV_P distribution diagrams between 100 MPa and minimum pressure (Fig. III.4) shows typically virtually inverse pattern to the distribution of P-wave velocities obtained at minimum confining pressure (Fig. III.4). The pattern is characterized by formation of girdle or single maxima of high velocity differences perpendicular (variety I) or 20° to 40° oblique (variety II and III) to the reference plane. Low velocity differences are typically oriented in perpendicular position to the high velocity field. In general, partial ΔV_P diagrams between each pressure steps don't show any significant change of ΔV_P pattern with increasing pressure (appendix 1). An exception from the general trend can be observed for samples me04 (variety I), me03 and me05 (variety III), where pattern of ΔV_P distribution become rather scattered above 100 MPa. Another difference from the general ΔV_P distribution is observed for the sample me06 (variety III), which exhibits between 0.1 MPa and 10 MPa inverse ΔV_P distribution pattern to that observed between minimum and 100 MPa (appendix 1). However, subsequent partial ΔV_P diagrams are similar to the overall picture. The calculated anisotropy a and the average velocity difference of P-wave velocities obtained at 100 MPa and minimum confining pressure differs significantly between the microstructural varieties (Table III.2., appendix 2., and Fig. III.4). The highest anisotropy and the average velocity difference is observed for the variety I. ranging between 13.3 % and 11.2 % and 1.7 and 1.2 km.s⁻¹, respectively. The intermediate anisotropy and the lowest average velocity difference shows samples of the variety III reaching values between 4.0 and 10.6 % and 0.7 and 0.9 km.s⁻¹, respectively. The lowest observed anisotropy and the intermediate average velocity occurs in samples of the variety II ranging between 3.7 and 4.3 % and 1.0 and 1.1 km.s⁻¹, respectively. The observed systematic concentrations of high velocity differences indicates that microcracks present in the studied samples are preferentially oriented parallel (variety I) or 20° to 40° oblique (variety II and III) to the reference plane. Moreover, it can be seen that even at pres-

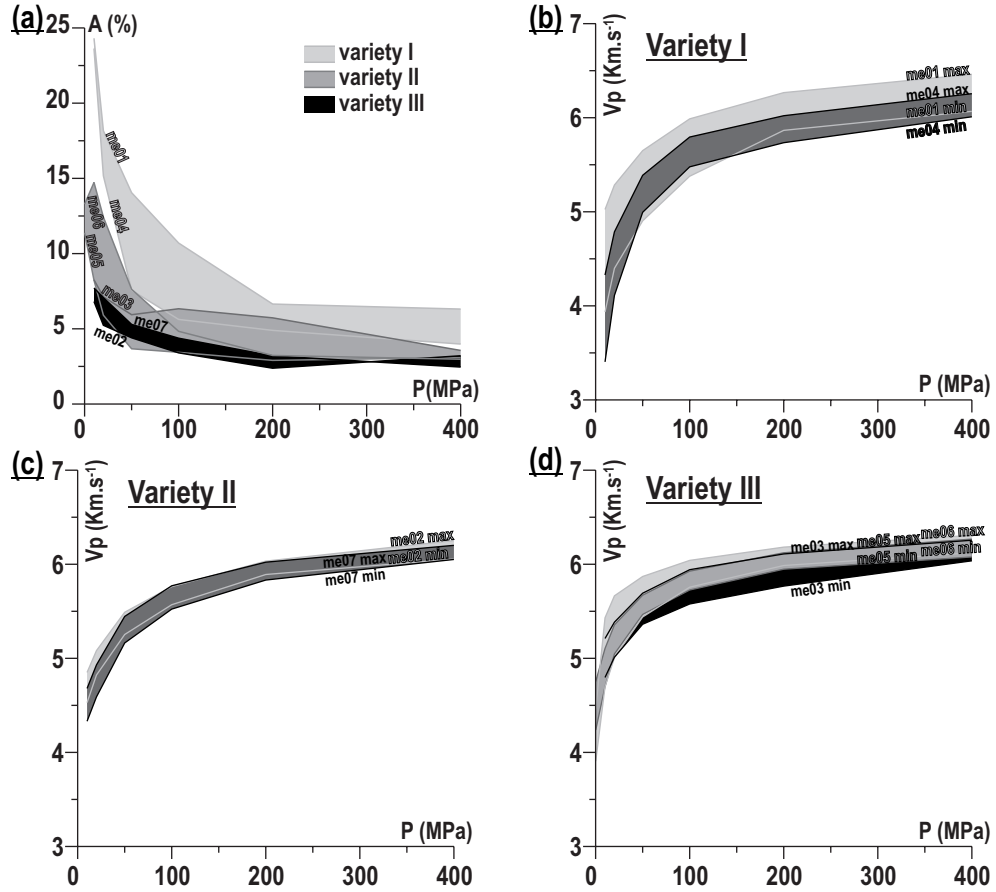


Figure III.5. Graphs of P-wave velocity anisotropy (a) and maximum and minimum velocity (b,c,d) dependence on increasing confining pressure, (b) microstructural variety I, (c) microstructural variety II, (d) microstructural variety III.

pressures above 200 MPa some microcracks of main preferred orientation in the most samples from all microstructural varieties remain present (open). While for the samples me04, me03 and me05 the partial ΔV_p diagrams indicate that most of preferentially oriented pores closed down between 0.1 and 100 MPa. Our observations indicate weaker preferred orientation of pore space in the samples me02, me03 and me05.

3.4. Porosity and permeability

The measured porosity ranges between 1.7% and 3.8% and it shows correlation with the grain size. The observed porosity dependence on the grain size correlates with the observed average velocity difference. The

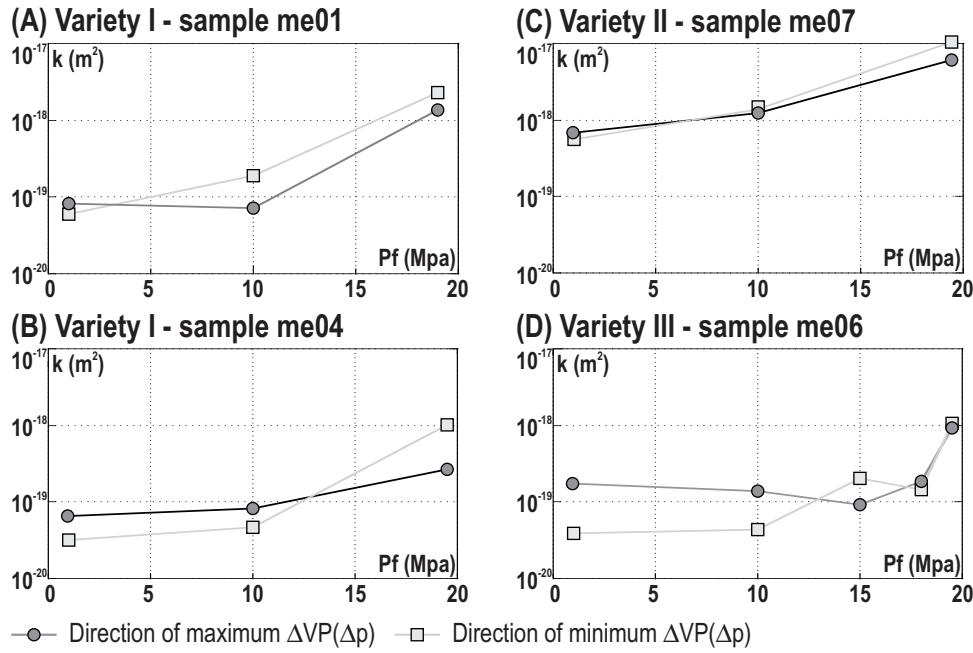


Figure III.6. Evolution of permeability in direction of maximum and minimum $\Delta V_P(\Delta p)$ with increasing pore fluid pressure for each measured sample.

results of permeability measurements (steady state flow method) are listed in Table III.3 and plotted as a function of pore pressure in Figure III.6. In

Table III.3 Permeability at levels of effective pressure

Sample	Direction	0.5 Mpa	2Mpa	5 Mpa	10 Mpa	19 Mpa
me01	K(min)	2.30E-18	x	x	1.90E-19	6.04E-20
	K(max)	1.36E-18	x	x	7.14E-20	8.20E-20
me04	K(min)	1.01E-18	x	x	4.71E-20	3.18E-20
	K(max)	2.66E-19	x	x	8.17E-20	6.54E-20
me07	K(min)	1.05E-18	1.44E-19	2.01E-19	4.32E-20	3.81E-20
	K(max)	8.35E-19	1.53E-19	8.99E-20	1.20E-19	1.66E-19
me06	K(min)	1.03E-17	x	x	1.35E-18	5.48E-19
	K(max)	6.01E-18	x	x	1.20E-18	6.65E-19

Direction - measurement of in direction corresponding to the direction of minimum and maximum difference between P-wave velocities measured at minimum and 100 MPa of confining pressure.

all samples, a significant decrease of permeability between the effective pressures 0.5 MPa and 10 MPa is observed. The values for the effective pressure of 0.5 MPa range over two orders of magnitude (10^{-17} to 10^{-18} m^2). At this effective pressure, slightly lower permeability in direction normal to the measured microcrack preferred orientation is observed. This observed difference is significant only in the coarse-grained sample me04 and in the medium-grained sample me07 (Table III.3). Permeability values

measured at the effective pressure of 10 MPa range between 1.4×10^{-18} and $4.7 \times 10^{-20} \text{ m}^2$ (samples me07 and 04, respectively) without systematic directional dependence. At the effective pressure of 19.5 MPa, permeability values range between 5.5×10^{-19} and $3.9 \times 10^{-20} \text{ m}^2$ (samples me07 and me06, respectively), also without any systematic directional dependence.

3.5. Microstructural analysis

The quantitative microstructural analysis was performed on the same samples used for the porosity and permeability measurements (me01, me04, me07 and me06). Three sections were cut from each sample in the coordinate system given by the results of the ultrasonic velocity measurements: direction of maximum (z) and minimum (x) of P-wave velocity differences (ΔV_P) between the minimum and 100 MPa pressure steps. The orientation of sections is chosen according to expected preferred orientation of microcracks normal to the direction of maximum P-wave velocity differences. Sections are oriented mutually perpendicular, except for the sample me01 (variety I), where sections xy and yz are oriented 110° angle-wise. The xz section is then parallel to both directions of minimum and maximum ΔV_P , xy section is perpendicular to the direction of maximum ΔV_P and yz section is perpendicular to the direction of minimum ΔV_P . Properties of microcrack networks are summarized in table III.4 and preferred orientation is illustrated in figures III.6 and III.7 by microcrack rose diagrams and projection function $A(\alpha)$ obtained from SURFOR analysis. The microcrack density of studied granites ranges from 2.6 to 4.2 mm/mm^2 . The highest density of 3.9 mm/mm^2 in average is observed in the sample me07 from the variety II. All other samples from the variety I and III show similar average density ranging between 2.7 and 3.0 mm/mm^2 . No systematic relation between density and section type has been observed (Table III.4). The representation of the microcrack types is generally similar for all microstructural types. The most abundant type in all samples are the intragranular microcracks in feldspars

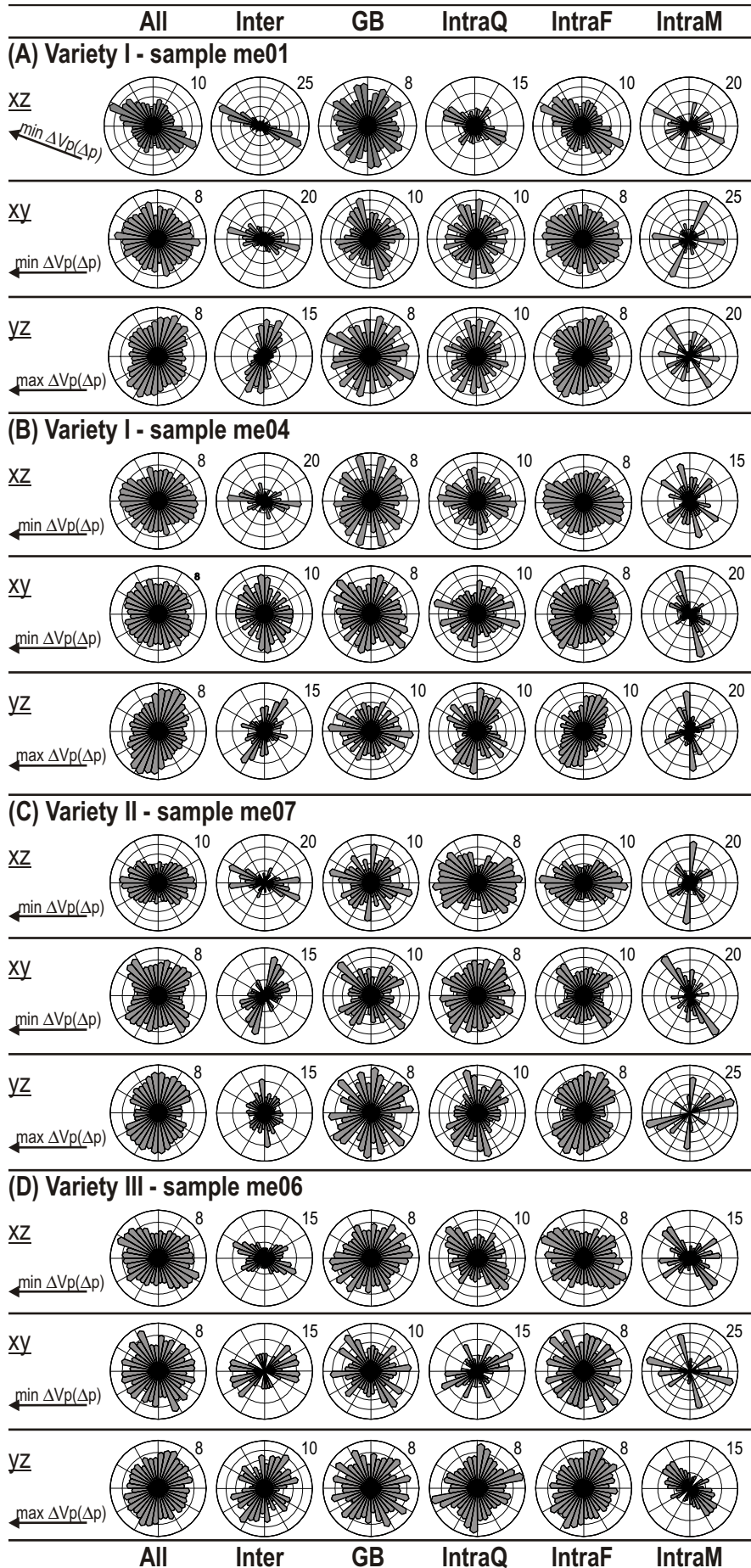


Table III.4 (A) Summary of microstructural analysis of entire microcrack networks

Sample	Section	Density	Length		Representation and length of the microcrack types								SURFOR		
		All (mm/mm2)	All L(mm)	IntraM %	L(mm)	GB %	L(mm)	Inter %	L(mm)	IntraF %	L(mm)	IntraQ %		L(mm)	(A(a)min)
Variety I	me01	xz	2.64	0.59	6.08	0.64	21.60	0.95	13.59	2.49	47.13	0.40	11.60	0.76	0.77
		xy	2.80	0.59	3.41	0.67	21.98	0.96	17.43	2.05	48.98	0.40	8.20	0.66	0.89
		yz	2.72	0.58	3.07	0.63	18.79	0.97	17.05	2.09	50.26	0.41	10.83	0.69	0.85
	me04	xz	3.14	0.56	4.16	0.61	20.89	0.96	11.18	2.17	55.57	0.42	8.20	0.65	0.89
		xy	2.82	0.69	8.06	0.76	30.88	1.05	17.54	2.12	36.77	0.42	6.74	0.68	0.96
		yz	3.00	0.70	6.63	0.75	18.51	1.14	25.79	2.83	40.82	0.42	8.26	0.68	0.82
Variety II	me07	xz	4.22	0.30	8.13	0.32	17.31	0.53	7.14	0.68	48.03	0.25	19.34	0.28	0.80
		xy	3.98	0.29	4.12	0.24	14.66	0.47	11.16	0.74	50.29	0.24	19.76	0.27	0.96
		yz	3.41	0.31	1.07	0.30	17.55	0.51	19.09	0.68	49.72	0.22	12.57	0.33	0.88
Variety III	me06	xz	3.01	0.50	2.61	0.40	26.78	0.73	18.33	1.40	42.60	0.34	9.68	0.46	0.90
		xy	2.47	0.37	2.83	0.38	26.24	0.58	7.44	1.44	53.12	0.29	10.38	0.39	0.90
		yz	3.07	0.43	2.55	0.35	19.40	0.62	24.56	1.12	43.11	0.29	10.39	0.40	0.92

Table III.4 (B) Summary of microstructural analysis of microcrack networks skeletons

Sample	Section	Density	Length	Representation and length of the microcrack types										SURFOR	
		All	All	IntraM	GB		Inter		IntraF		IntraQ				
		(mm/mm2)	L(mm)	%	L(mm)	%	L(mm)	%	L(mm)	%	L(mm)	%	L(mm)	(A(a)min)	
Variety I	me01	xz	1.14	0.49	0.36	0.39	22.60	0.74	20.93	1.99	42.75	0.31	13.36	0.63	0.80
		xy	1.46	0.54	0.57	0.34	24.61	0.77	26.45	1.70	40.37	0.34	8.00	0.54	0.87
		yz	1.56	0.54	0.82	0.43	21.88	0.81	26.97	1.67	41.00	0.34	9.32	0.50	0.88
	me04	xz	1.98	0.49	1.35	0.43	21.83	0.82	14.21	1.80	54.54	0.36	8.07	0.53	0.88
		xy	1.78	0.65	2.48	0.54	35.61	0.91	24.01	1.93	31.55	0.37	6.35	0.58	0.97
		yz	2.16	0.69	2.16	0.75	19.41	1.01	33.75	2.65	36.88	0.38	7.80	0.55	0.84
Variety II	me07	xz	0.28	0.22	0.79	0.10	24.40	0.39	16.75	0.38	41.44	0.17	16.62	0.16	0.77
		xy	0.78	0.23	0.39	0.46	12.83	0.35	24.10	0.64	48.22	0.17	14.46	0.18	0.90
		yz	1.32	0.26	0.26	0.46	16.67	0.36	29.29	0.50	41.38	0.17	12.40	0.31	0.91
Variety III	me06	xz	1.37	0.43	0.11	0.25	33.51	0.63	24.53	1.04	34.13	0.26	7.72	0.34	0.89
		xy	0.87	0.27	0.00	0.00	25.43	0.32	12.12	1.00	56.08	0.22	6.36	0.28	0.87
		yz	0.90	0.34	0.00	0.00	18.98	0.42	35.64	0.74	38.09	0.22	7.28	0.25	0.91

Abbreviations of microcracks type: All -whole microcrack network, Inter - intergranular cracks, GB - grain boundary cracks, IntraQ - intragranular cracks in quartz, IntraF - intragranular cracks in feldspar, IntraM - cleavage cracks in mica.

forming between 40 and 55 % of all microcracks (Table III.4). Other abundant types are in general microcracks on grain boundaries and intergranular cracks. The least frequent microcrack types are intergranular cracks in quartz and cleavage cracks in mica (Table III.4). The length of microcracks differs significantly between the microstructural types. The longest microcracks are observed in the variety I (average 0.6 mm) and the shortest microcracks are in the variety II (average 0.3 mm). The average length of microcracks in the variety III is 0.4 mm. The longest microcracks in all varieties and sections are intergranular microcracks and microcracks on grain boundaries. The first microcrack type has length usually more than twice the average length. Other types show length close to the average, where the shortest are intragranular cracks in feldspars. The preferred orientation of microcracks obtained by SURFOR method is in orientation similar for all samples showing in xz and xy section orientation subparallel to minimum (x) P-wave velocity differences and in section yz perpendicular to orientation of maximum (z) P-wave velocity differences (Fig. III.7 and III.8, Table III.4). The only exception can be seen in section xy of the sample me07 (variety II), where two main preferred directions oriented symmetrically 50° around the direction of minimum ΔV_P are present. The weakest preferred orientation of microcracks is observed in the sample me06 and shows similar fabric anisotropy ($A(\alpha)_{\min}$) in all three sections. Other three samples show similar range of fabric anisotropy. The lowest anisotropy is regularly observed in xy section (Table III.4). The strongest anisotropy is recorded in section xz in the samples me01 and me07, while in the sample me04 the largest anisotropy is documented in section yz (Table III.4). For the overall preferred orientation and fabric anisotropy mainly participates in-

Figure III.7. Rose diagrams of orientation of individual types and all microcracks in samples of variety I (a, b), variety II (c) and variety III (d). Data obtained from sections parallel to XZ, YZ and XY planes defined based on results of P-wave velocity measurements as described in the text. Orientation of minimum or maximum of $\Delta V_P(\Delta p)$ is marked in the figure. Abbreviations of microcracks type: All – whole microcrack network, Inter – intergranular cracks, GB – grain boundary cracks, IntraQ – intragranular cracks in quartz, IntraF – intragranular cracks in feldspar, IntraM – cleavage cracks in mica.

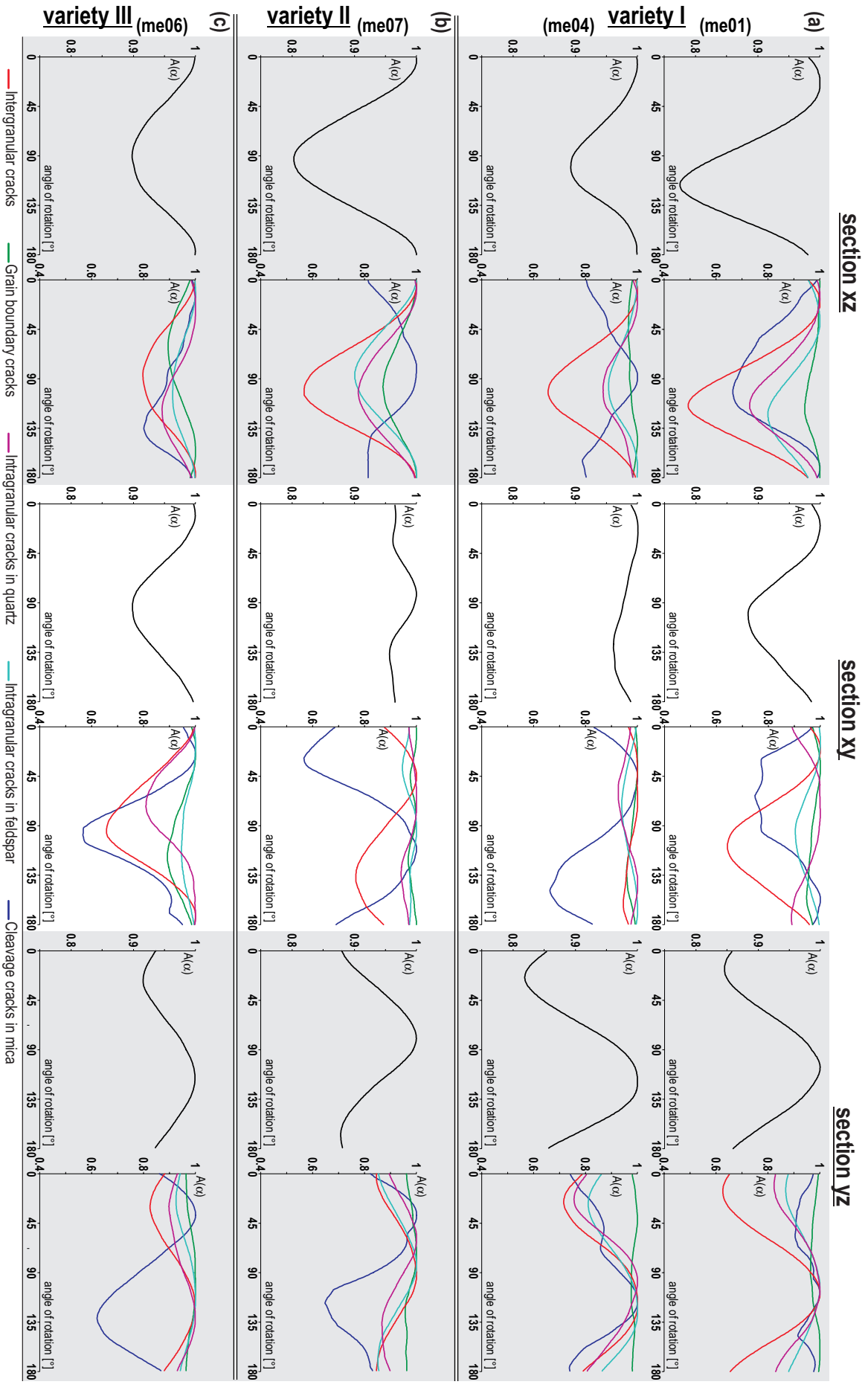


Figure III.8. Variety I (a, b), variety II (c) and variety III (d) microcrack fabric of all cracks and of individual crack types. The curve $A(\alpha)$ represents the average crack projection (see SURFOR; Panozzo, 1984). $A(\alpha)$ is normalized: $A(\alpha)$ max = 1.00. Fabric anisotropy is defined by $A(\alpha)$ minimum at the angle of preferred orientation α_p and presented in table III. 4.

tergranular cracks, intragranular cracks in quartz and intragranular cracks in feldspars (Fig. III.8). The intergranular cracks show regularly the highest fabric anisotropy ($A(\alpha)_{\min}$) obtained from SURFOR analysis. The grain boundary cracks shows weak anisotropy and often preferred orientation different from the overall trend.

3.6. Analysis of connected network

To perform the quantitative microstructural analysis of connected microcracks, the fracture network was cleaned until no 1st degree node exists, withal keeping nodes on convex hull of the original network. This produces a “skeleton” of connected microcracks of the network. The “skeleton” of fracture network was subjected to the same analysis of microcracks properties and orientation as the entire network. The quantitative analysis of “skeleton” networks is supplied by analysis of network connectivity using total connectivity ratio C , k th-order connectivity ratio C_k and crack network extent C_e as defined by Zhang et al. (1992) (for details see Chapter I - Methodology). For the microcrack density of network skeletons is characteristic significant drop with respect to microcrack density of original network. The density ranges from 0.3 to 2.15 mm/mm² and shows dependence on microstructural variety (Table III.4). The density decrease is least significant for coarse-grained samples of variety I, where the analysis exclude from network 28 to 60 % of microcracks showing values ranging from 1.14 to 2.15 mm/mm² (Table III.4). The medium grained variety II shows largest microcrack density decrease to range between 0.3 and 1.32 mm/mm², representing extraction of 94 to 61 % of microcracks from the network. The fine grained variety III shows density drop to range between 0.9 to 1.37 mm/mm² (72 to 55 % of microcracks removed). The representation of the microcrack types in network skeletons differs from representation in entire networks. In all samples abundance of intergranular cracks increase significantly (from 3 to 13 %) and slightly also increase abundance of grain boundary cracks. Abun-

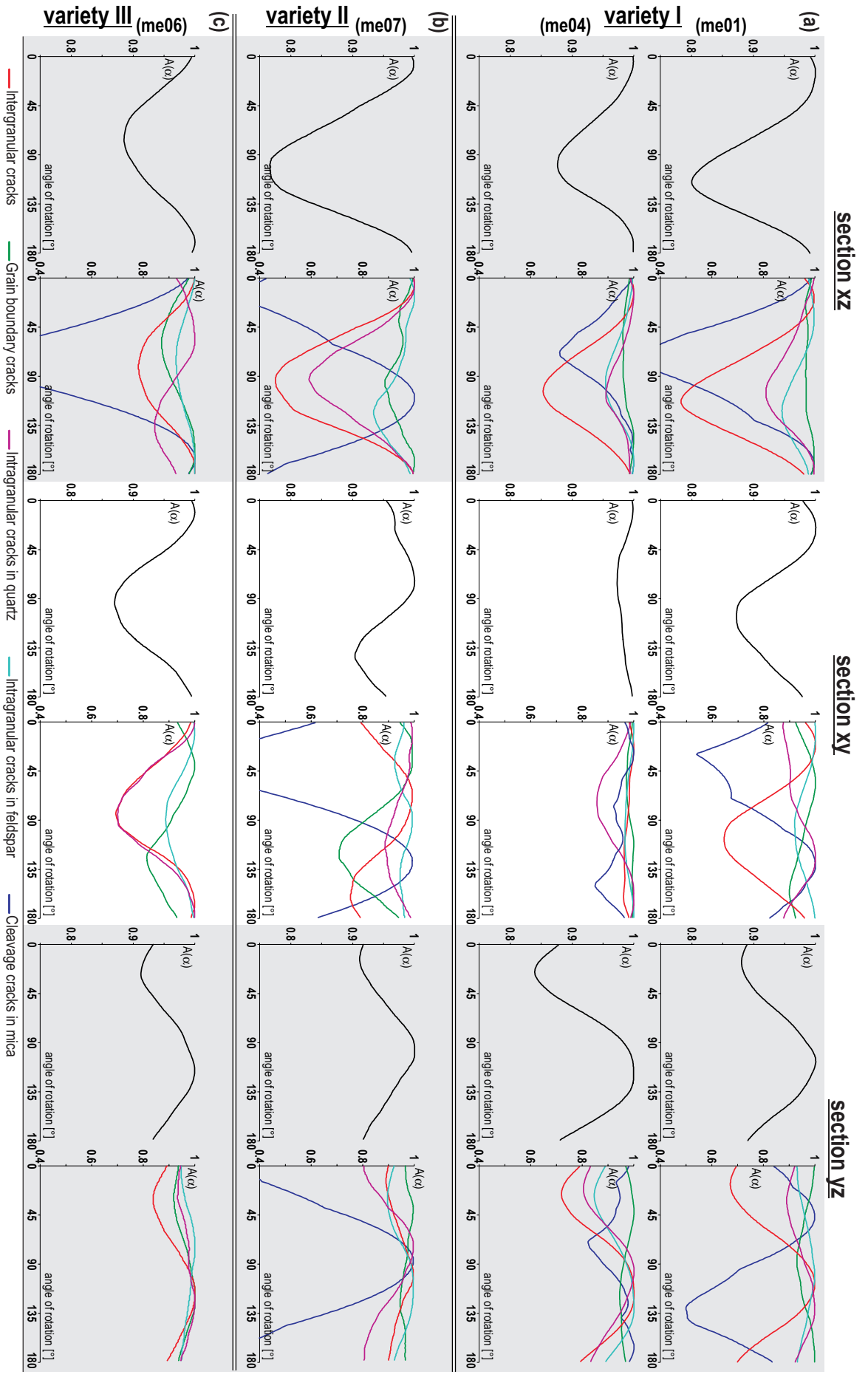


Figure III.9. Variety I (a, b), variety II (c) and variety III (d) microcrack fabric of all cracks and of individual crack types of skelnet networks. For graph description see Fig. III.8

dance of intergranular and grain boundary cracks occur at the expense of intragranular cracks in feldspars and cleavage cracks in mica, which almost vanish. All samples from all varieties exhibits shortening of al microcrack types compared to length of microcracks of the entire network. The shortening is more significant for medium and fine grained variety. The preferred orientation of microcracks as well as fabric anisotropy ($A(\alpha)_{min}$) is for network skeletons similar to preferred orientation and anisotropy of entire networks in all samples (Table III.4 and Fig. III. 9). Analysis of network connectivity reveals the highest total connectivity ratio and crack network extent in samples of microstructural variety I (Table III.5). The total con-

Table III.5 Analysis of network connectivity

		C	Ce	order	(Bs)max
var. I (me01)	xz	0.96	0.36	1516	3997
	xy	0.97	0.75	2498	6579
	yz	0.97	0.76	2716	7111
var. I (me04)	xz	0.98	0.85	5288	13468
	xy	0.98	0.91	3932	10147
	yz	0.98	0.94	4388	11108
var. II (me07)	xz	0.96	0.13	37	81
	xy	0.96	0.17	185	481
	xy	0.95	0.05	198	526
var. III (me06)	xz	0.71	0.02	688	1817
	xy	0.84	0.1	173	454
	yz	0.94	0.11	259	676

total connectivity ratio C. crack network extent Ce. number of connected branches in a single crack network (Bs)max

nectivity ratio range from 0.96 to 0.98 in both samples of variety I, being slightly higher for sample me04. The crack network extent is markedly high for sample me04 (0.85 – 0.94) and somewhat lower for sample me01 (0.35 – 0.75). The fine grained variety III showed also relatively high total connectivity ratio (0.95 – 0.96). however significantly lower crack network extent (0.05 – 0.17). Lowest values of total connectivity ratio and network extend display sample me07 of variety II (0.71 – 0.94 and 0.02 – 0.11 respectively). Such observation together with kth-order connectivity ratios (Fig. III.10 and Appendix 3) shows that in microcrack network of variety I dominate one main high-order connected network. On the other hand the microc-

rack networks of variety II and III are formed by many low-order connected networks.

3.7. Summary and Discussion

P-wave velocity patterns and their pressure dependence document strong influence of open microcracks on elastic anisotropy and pressure evolution of V_P in investigated granites, which has been already previously documented (Birch, 1960; Kern et al., 1997; Nishizawa, 1982; Sayers and Kachanov, 1995; Simmons and Brace, 1965; Schubnel and Guéguen, 2003). According to microstructural analysis, the pore space in all samples is formed by network of microcracks. Evolution of velocity patterns exhibits two general behaviors with increasing pressure being independent of granite microstructural type. The first one is characterized by the scattered distribution of V_P at pressures above 100 MPa which has been observed in the samples me04, me03 and me05. The second behavior is that the velocity pattern at 400 MPa is geometrically close to that observed at minimum confining pressure. Similar observation can be obtained from partial ΔV_P distribution diagrams between each pressure steps. However, all samples reveal similar values of velocity, its anisotropy, average ΔV_P and anisotropy of velocity differences at higher pressures independently of V_P and ΔV_P pattern evolution with increasing pressure. Such observations imply that in all studied samples there exists an open pore space even above 100 or 200 MPa. The first mode of behavior suggests that the pore space preserve similar geometry during increasing confining pressure even above 200 MPa. The second mode of behavior indicates that, the preferentially oriented pore space is closed between 100 and 200 MPa and remaining pores are scattered in orientation. However, similar amount of pore space remain open in this samples as it is documented by similar values of average ΔV_P . In the fine-grained sample (me06), partial ΔV_P distribution diagrams reveal volume of pore space almost in perpendicular geometry to the general

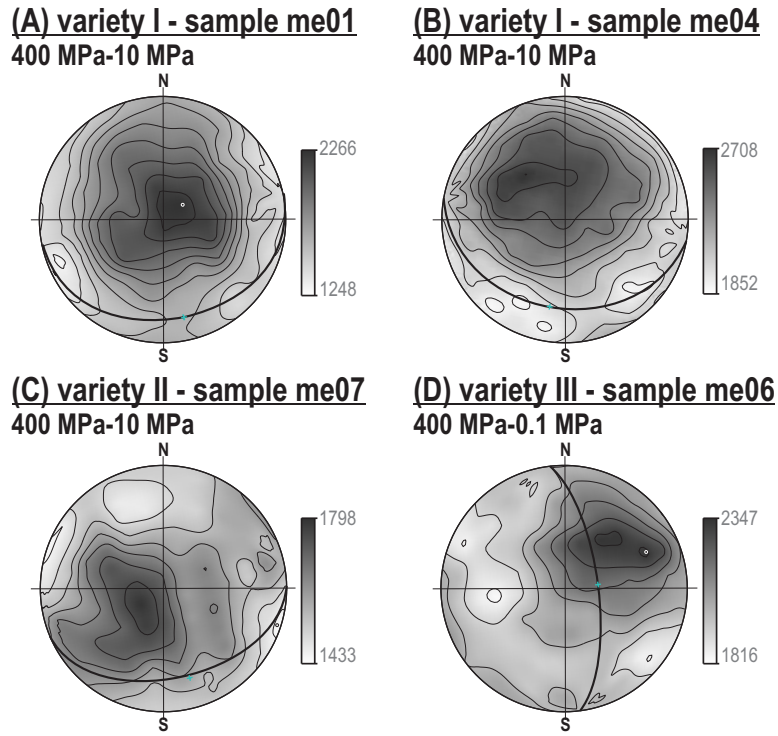


Figure III.10. Stereodigrams of the the P-wave velocity differences (ΔV_p (Δp)) dependence in space in geographic position with marked orientation of reference plane.

orientation. However, these “perpendicular” pores are at 20 MPa already closed. Such an observation can be explained by the presence of a set of microcracks with the lower aspect ratio, which commonly close at lower effective pressures (Le Ravalec et al., 1996; Reuschlé et al., 2003). The pore space geometry (microcrack preferred orientation) determined from analysis of the spatial distribution of ΔV_p (Δp) do not correspond to observed geometry of macroscopic fractures in the Melechov massif (Lexa et al., 2005b). However, the orientation of pore space geometry (Fig. III.10) in microstructural variety II (samples me02 and me07) however correlates with the AMS observed on sampling locality (Fig. 1c) as well as on actual spherical samples (Fig. III.3). This suggests that magmatic flow fabric of variety II granites could to some extent predispose the microcrack development. These microcracks however do not develop in mica, regarding the discrepant orientation of the mica cleavage cracks with respect to microcrack preferred orientation. Such correlation is not observed for other two vari-

eties (Fig. III.8). Pore space in microstructural varieties II and III exhibits planar preferential orientation 20 - 40° oblique to the individual reference plane (closest macroscopic fracture). Samples of variety I show planar preferential orientation parallel to the reference plane. In the case of variety I samples the reference plane is represented by exfoliation plane. Observations deduced from analysis of the spatial distribution of ΔV_P (Δp) together with discrepancy with regional scale fracture network imply that the pore space geometry and thus also orientation of microcracks is not consistent with regional macrofracture network. This suggests that in the studied samples, the stress regimes that give rise to brittle structure of the granite massif as it has been observed on other places (Plumb et al., 1984; Kowalis et al., 1987; Vollbrecht et al., 1991; Kano and Tsuchiya, 2002; Åkesson et al., 2004; Onishi and Shimizu, 2005) are not directly responsible for the microcrack development. The regular relation of pore space geometry to the closest macroscopic fracture is most likely linked to the development of microcracks in the process zone of that fracture during its propagation or reactivation (Scholz et al., 1993; Anders and Wiltschko, 1994; Vermilye and Scholz, 1998; Zang et al., 2000; Wilson et al., 2003).

The measured porosity ranges between 1.7 and 3.8% and shows correlation with the grain size. Observed porosity dependence on the grain size is related to the observed average velocity difference. In all samples, a significant decrease of permeability between the effective pressures 0.5 MPa and 10 MPa was observed. The permeability values at the effective pressure of 0.5 MPa range over two orders of magnitude (10^{-17} to 10^{-19} m²) and are higher than in an ordinary intact granite (Larive, 2001). At the lowest effective pressure, directional dependence of permeability corresponds to microcrack preferred orientation perpendicular to the orientation of P-wave velocities difference maximum. Observed permeability difference is significant only in the coarse-grained sample me04 and in the medium-grained sample me07. With increasing effective pressure, the permeability decreases up to two orders of magnitude in all samples. Microstructural

analysis of microcrack networks document microcrack density in the range from 2.6 to 4.2 mm/mm², which is lower than commonly observed in intact granites (Nasser et al., 2007; Wong, 1985; Moore and Lockner, 1995).

The highest microcrack density observed in medium-grained granite (sample me07) corresponds to the highest established permeability. On the other hand microcrack densities show no correlation with the grain size of samples. This observation is in contradiction with the expectation based on results and correlation of measurements of P-wave velocities (average ΔV_P) and porosity. The average length of microcracks partly correlates with the microstructural variety, being significantly largest in the coarse-grained granite (variety I) and the shortest in the medium-grained granite (variety II). Observed preferred orientation of microcracks is in agreement with the pore space geometry deduced from the distribution of P-wave velocity differences, being mostly perpendicular to the maximum of P-wave velocity differences. Only in medium-grained sample me07 in section xy, two main microcrack preferred orientations are present 50° symmetrically around the direction of minimum ΔV_P . It is important to note that xy section where the twofold microcrack preferred orientation is observed is parallel to the plane of pore space preferred orientation deduced from ΔV_P distribution diagrams. The weakest microcrack preferred orientation is observed in the fine-grained sample me06 (variety III) with similar values of fabric anisotropy ($A(\alpha)_{\min}$) in all three sections. The strongest observed microcrack preferred orientation among all samples occurs in one sample of variety I (me01) and of variety II (me07) in section xz (section parallel to maximum and minimum ΔV_P). For samples showing the directional dependence of permeability, it is common that in the section xy, parallel to the plane of pore space preferred orientation, the fabric anisotropy of microcracks is significantly lower than in other sections and samples. Classification of microcracks to five types based on microstructural position showed that the most important in terms of fabric anisotropy are intergranular cracks followed by intragranular cracks in quartz and intragranu-

lar cracks in feldspars. The grain boundary cracks exhibit very low fabric strength with variable orientation. The cracks in micas have usually high fabric anisotropy, but with discrepant preferred orientation compared with the overall microcrack preferred orientation. The relatively strongly preferentially oriented intergranular cracks follow overall microcrack orientation. The intergranular cracks are also the significantly longest cracks among other types but not the most abundant. The most frequent type of cracks is the intragranular cracks in feldspars, which are also the shortest. The intergranular cracks in our study are defined as cracks that cut through at least one whole grain and can continue on the grain boundary or on the cleavage plane of other mineral. It is therefore difficult to distinguish if such intergranular cracks open as one crack or if more cracks of different type are interconnected to one large crack. Such process of crack interconnection in studied granites could reduce the number of originally grain boundary cracks in orientation close to the general preferred orientation. In general, intergranular cracks, cracks in quartz and cracks in feldspars form the overall microcrack fabric and thus preferably reflect the stress field, which induced the microcrack development.

The analysis of skeletons of connected networks show an increase in abundance of intergranular cracks in networks of connected microcracks and decrease in content of cracks in feldspars and micas. Important observation of little or none influence of cleavage cracks in mica on microcrack network connectivity is discrepant from observation of significant influence of such cracks on P-wave velocities difference even if micas represent only minor volume of the rock (Babuška and Pros, 1984; Siegesmund et. al., 1993). This implies that interpretation of microcrack network connectivity, based only on P-wave velocities and their differences can be in contradiction with results of microstructural investigation. Microcrack network of variety I is dominated by one main high-order network of connected microcracks. On the other hand, the microcrack networks of varieties II and III are formed by many low-order microcrack networks. The connectivity of microcrack net-

works shows dependence on average crack length as suggested by Zhang (1992). However, no correlation between crack network connectivity and actual permeability is observed in samples from the Melechov granite.

3.8. Conclusions

Based on investigation of granite samples from Melechov massif we propose a combination of three laboratory methods: measurements of elastic velocities at increasing confining pressure, quantitative microstructural analysis of samples impregnated by fluorescent epoxy resin and measurements of permeability in several directions at increasing confining pressure, which turned out to be effective in evaluation of preferred orientation of pore space and determination of diverse aspects of rock properties.

The pore space geometry reflects the orientation of exfoliation planes in coarse-grained granite. However, in medium-grained and fine-grained granite the, pore space is preferentially oriented 20° to 40° oblique to the closest macrofracture. In general view the pore space preferably formed by planar microcracks does not reflect the observed geometry of macroscopic fractures in the Melechov massif. More likely is the explanation that microcracks forming preferred orientation developed in process zone of closest macrofracture during its propagation and/or reactivation (Scholz et al., 1993; Vermilye and Scholz, 1998; Wilson et al., 2003). Microfracture orientation in fracture process zone corresponds to stress field orientation during fracture propagation and reactivation. The stress field orientation depend on mode of propagation or reactivation (Scholz et al., 1993).

Permeability in studied granites shows significant decrease up to two orders of magnitude with increasing effective pressure from 0.5 MPa to 10 MPa. Established permeability directional dependence corresponds to preferred orientation of microcracks perpendicular to the maximum P-wave velocities difference. The highest permeability measured at the minimum confining pressure correlates with the maximum density of microcracks.

Porosity and observed average velocity difference shows a correlation with the grain size of granite. On the other hand, the microcrack density does not show correlation with grain size. Microcrack preferred orientation is in agreement with pore space geometry deduced from distribution of P-wave velocity differences, being mostly perpendicular to the maximum of P-wave velocity differences. The most important crack type in terms of fabric strength and interconnectivity is intergranular crack.

4. Development of pore space geometry in progressively deformed metagabbro

co-authors: Petr Špaček, Stanislav Ulrich, Lenka Baratoux, Rostislav Melichar, Jakub Haloda

The pore space geometry in crystalline rocks is controlled by the microstructural framework. In the low porosity crystalline rocks, the pore space is typically formed by microcrack networks, and it was shown that the original microstructure have strong influence on the process of the pore space opening during lithostatic stress relieve (Machek et al. 2007). In this chapter we examine relationship between pore space geometry and original deformational microstructure developed during plastic deformation of metagabbro from the Staré Město belt (Bohemian Massif). The gabbroic rocks were chosen as a relatively simple biminerale system common in the Earth crust. Four stages of deformation ranging from weakly-deformed gabbro mylonite up to ultramylonite are described in terms of microstructure, texture and pores space geometry. The methodology of pore space investigation is based upon measurements of P-wave velocity distribution in space and subsequent analysis of difference of P-wave velocity measured at different levels of confining pressure. In order to establish the influence of open pore space on the P-wave velocity distribution at high confining pressures (at 400 MPa), the experimentally acquired data are confronted with numerically obtained velocity distribution data deduced from lattice

preferred orientation of main constitutive minerals.

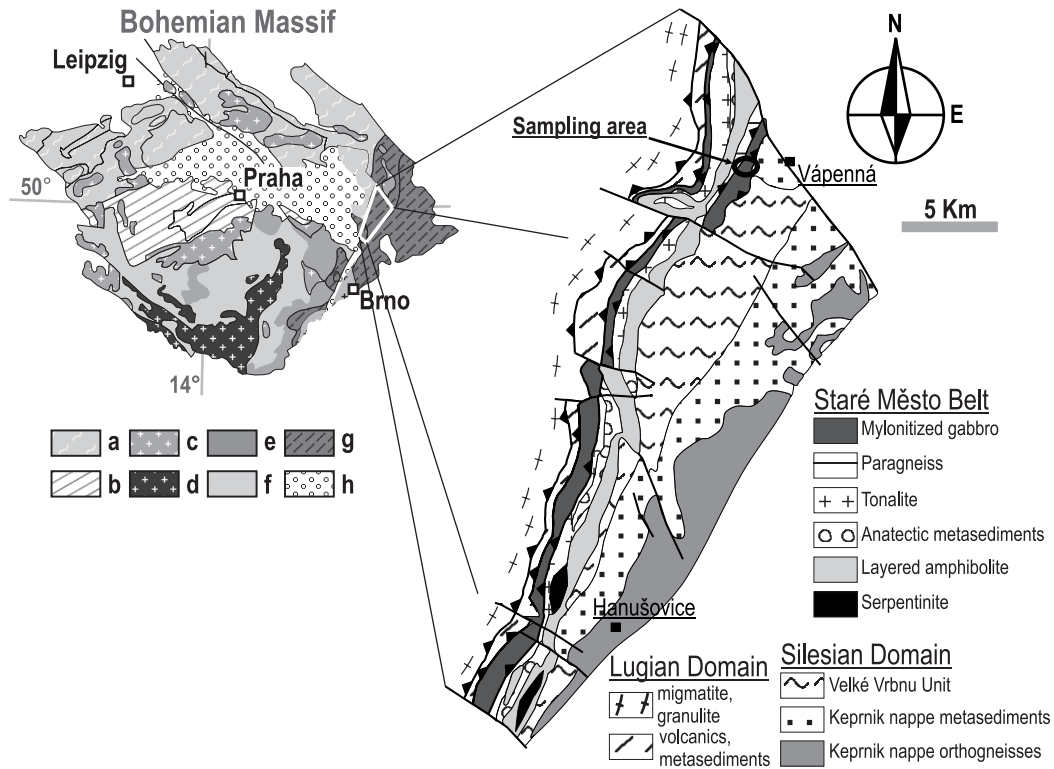


Figure IV.1. Location of the studied area in the frame of the Bohemian Massif. Geological map of the Staré Město belt is based on unpublished geological maps 1:25 000 provided by the courtesy of the Czech Geological Survey (Dr. M. Opletal author). Important thrusts and faults and location of samples are indicated. (a- Saxothuringian and Lugian, b- Teplá-Barrandian, c- Variscan granitoids, d – Moldanubian Batholith, e - Gföhl unit, f - Varied and Monotonous unit, g - Brunovistulian, h - Cretaceous sedimentary cover)

4.1. Description of samples

The set of metagabbro samples from the Staré Město belt (Bohemian Massif) represents a lower crust progressively deformed under amphibolite facies conditions ($\sim 650^{\circ}\text{C}$ and 9 kbar) (Baratoux et al., 2005; Štípská et al., 2001). ranging from weakly deformed protomylonite to ultramylonite (Fig. IV.1). Samples of modal composition $\sim 50\%$ of amphibole and $\sim 50\%$ of plagioclase and sample from amphibole-rich domains with 80% of amphibole were investigated. Detailed description of microstructures was presented by Baratoux et al. (2005). Only the most important microstructural features from the work of Baratoux et al. (2005) will be thus reported here.

Amphibole at the protomylonite and mylonite stages exhibit twinning on (100) planes (Rooney et al., 1975), kinking and strong undulatory extinction related to bending of crystalline lattice.

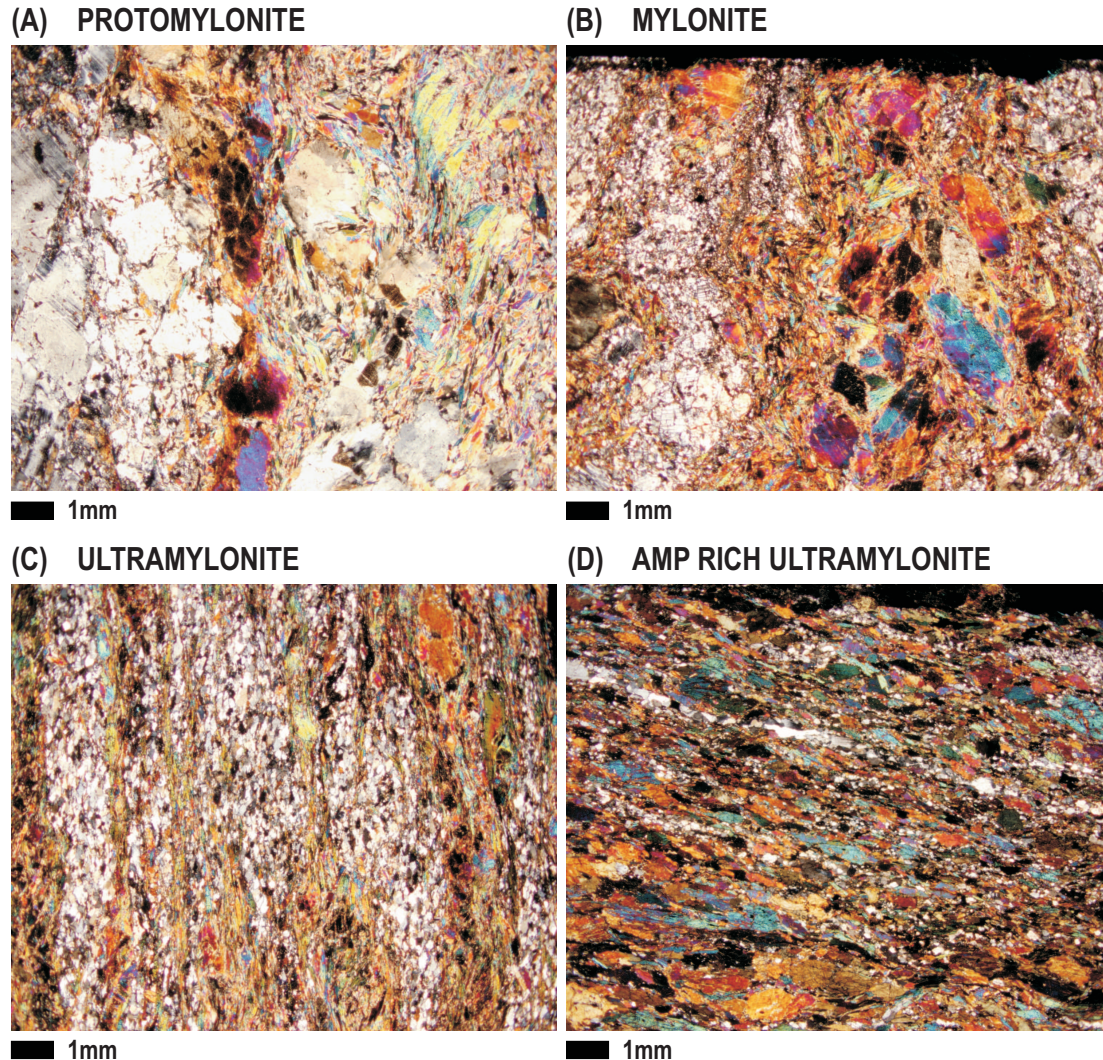


Figure IV.1. Micrographs of thin sections illustrating the microstructure of a) protolith, b) protomylonite, c) ultramylonite and d) amp-rich ultramylonite of Staré Město metagabbro. Thin sections were prepared parallel to lineation and perpendicular to foliation.

Microshear zones transect large porphyroclasts into book-shelf like segments and these segments further rotate with their c-axes parallel to the shear direction (Fig. IV.1a,b). These features are also preserved in porphyroclast of ultramylonite stage. Amphibole host grains are often rimmed by “subgrains” forming core and mantle-like structures (Fig. IV.1c,d). Contacts of new grains with the porphyroclast are very sharp indicating separation of

such a “subgrain” by microfracturing rather than by subgrain rotation (Nyman et al., 1992). With progressive deformation, amphibole and plagioclase tend to separate into monomineralic bands (Fig. IV.1). In bands amphibole shows grain size between 0.1–0.3 mm and strong shape preferred orientation, characterized by long axes alignment parallel to macroscopic foliation. (Baratoux et al., 2005)

The plagioclase at protomylonite and mylonite stage is characterized by development of “core and mantle” microstructure (Fig. IV.1a,b). The microstructure suggests recrystallization mechanism by subgrain rotation. The deformation leads to grain size reduction to 0.02–1 mm in size in plagioclase. Almost all plagioclase has recrystallized during mylonite and ultramylonite stages forming continuous bands with interstitial grains of amphiboles (Fig. IV.1b,c). Elongate plagioclase aggregates are composed of equilibrated mosaic of regular shape grains of 0.1–0.25 mm in size showing weak shape preferred orientation parallel to foliation. (Baratoux et al., 2005)

The grain boundaries show increasing degree of preferred orientation with progressive deformation. Two types of grain boundaries (plagioclase-plagioclase and plagioclase-amphibole) progressively deviates from the foliation direction, which was interpreted as increasing role of non-coaxial deformation. The preferred orientation of like-like grain boundaries of amphibole is only slightly inclined with respect to the foliation suggesting minor component of non-coaxial deformation. (Baratoux et al., 2005)

During the early stages of deformation in plagioclase the subgrain rotation and dislocation creep operated, as indicated by strong crystallographic and shape preferred orientations. Subsequent randomizing of plagioclase crystallographic preferred orientation is interpreted to be due to grain boundary sliding in the mylonitic stage. Amphibole is stronger and deforms in the brittle regime, which leads to important grain size reduction and strong shape preferred orientation. (Baratoux et al., 2005).

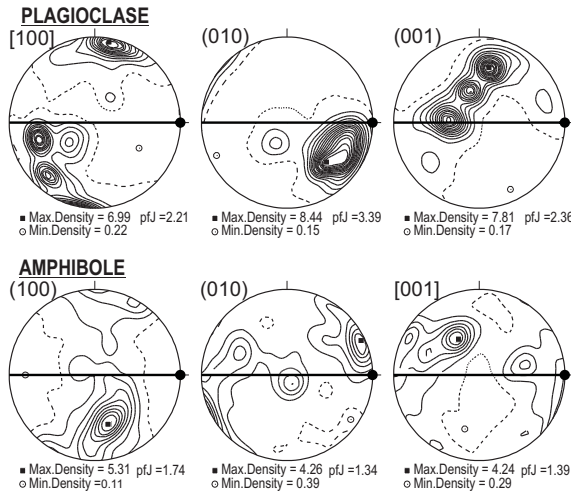
4.2. Lattice preferred orientation and deformation mechanisms

The lattice preferred orientation (LPO) were studied in four thin sections covering all the deformation stages. The LPO were measured automatically from large areas, approximately 2 mm wide and 20 mm long stripes oriented perpendicular to the foliation. LPO mapping were used to obtain LPO representative for the microstructure and to avoid influence of single large grain orientation on LPO and consequently also on the numerically determined P-wave velocity values and distribution. Plagioclase LPO in the protomylonit (Fig. IV.2) is characterized by a concentration of poles to (100) to incomplete girdle perpendicular to the foliation plane, moderately inclined from direction of lineation with clearly defined maxima perpendicular to foliation a lineation. Consequently, poles of (010) planes are concentrated to maxima perpendicular to the (100) poles girdle and (001) poles form girdle in similar orientation to that of (100) poles. The plagioclase fabric significantly weakens with increasing deformation, which is interpreted by a switch of the dislocation to the diffusion creep (Baratoux et al., 2005). The amphibole LPO is in the protomylonit and mylonite samples characterized by (100) poles girdle perpendicular to the foliation plane with maxima close to position perpendicular to the lineation. This is accompanied with (010) poles single concentration slightly inclined from the foliation and lineation, and amphibole c-axes incomplete girdle subparallel to foliation plane. The mylonitic amphiboles are characterized by arrangement of (100) planes parallel to the foliation and by the strong alignment of c-axes parallel to the lineation or along the foliation plane with maxima present in the direction of lineation. Amphibole LPO is even stronger in more deformed samples maintaining slightly oblique character with respect to the structural framework. The deformation mechanisms for amphibole were not uniquely determined based optical observations and EBSD data (Baratoux et al., 2005). The strong CPO patterns could be interpreted both in terms of activity of easy

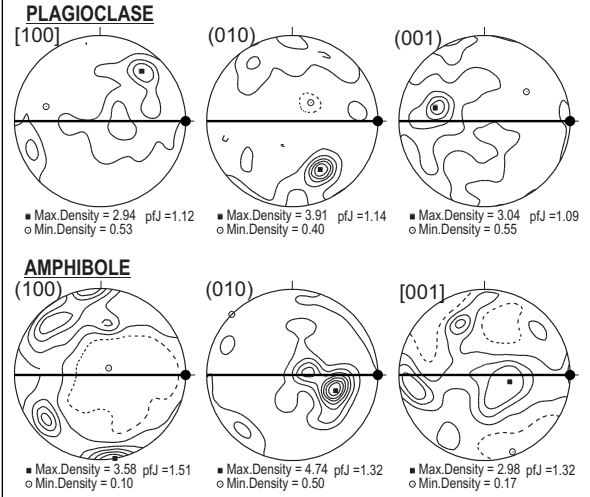
(100)[001] slip system suggesting dislocation creep or by translation glide on {110} plane indicating microfracturing (Baratoux et al., 2005).

LATICE PREFERRED ORIENTATIONS

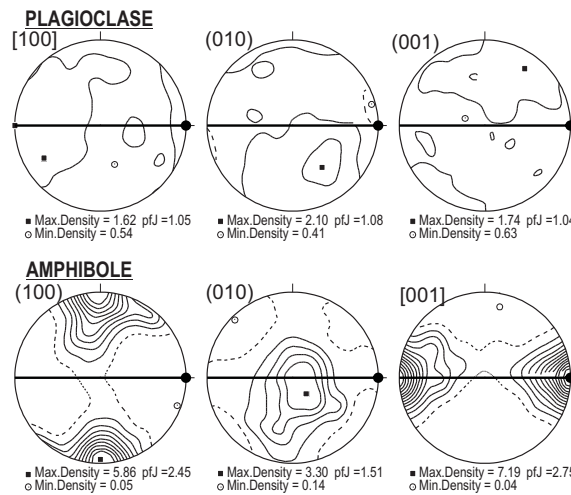
(A) PROTOMYLONITE



(B) MYLONITE



(C) ULTRAMYLONITE



(D) AMP RICH ULTRAMYLONITE

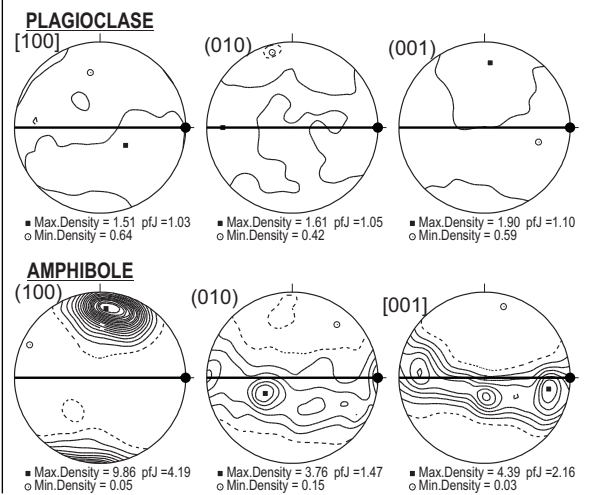


Figure IV.2. Amphibole and plagioclase LPO of a) protomylonite, b) mylonite, c) ultramylonite and d) amp-rich ultramylonite of Staré Město metagabbro measured using the EBSD technique. Equal area projection, lower hemisphere. Contoured at interval 1.0 times of uniform distribution. Foliation (full line) is horizontal and lineation is in this plane in East direction.

4.3. Seismic anisotropy

For the measurements of P-wave velocity distribution in space an experimental method of ultrasonic pulse-transmission technique (Pros et al., 1998) was used. To be able compare the numerically and experimentally obtained

P-wave velocity distributions it is necessary to extrapolate the experimental data to the atmospheric pressure. The measured velocities were extrapolated to 0.1 MPa using the slope of linear velocity increase between 200 and 400 MPa. The measured and extrapolated P-wave velocity values and distribution were compared with numerically obtained velocity distribution data. Calculation and numerical comparison of P-wave velocity data were done by special computer program developed by Spaček & Melichar (2005).

4.3.1. Experimental results

Pressure dependence of P-wave velocity

At small confining pressure, all samples reveal similar pattern of V_P distribution (Fig. IV.3) with maximum V_P oriented in the direction of lineation and minimum V_P oriented perpendicular to the foliation. With increasing confining pressure, the V_P distribution remains stable in samples showing distinct mylonitic fabric pattern. By contrast, protomylonite sample exhibits scattering of V_P distribution above 50 MPa. An increasing confining pressure causes also important decrease in velocity anisotropy. The V_P velocity anisotropy is dependent on the deformational state of the samples and modal proportion of amphibole (Table IV.1). At confining pressure of 20 MPa, the anisotropy increases from 12% in protomylonite to 29% in amphibole-rich ultramylonite. At 400 MPa, the pressure dependence of anisotropy is manifested by its increase from 5.5% in protomylonite to 16.8% in amphibole-rich ultramylonite. At 20 MPa of confining pressure, values of maximum V_P range between 6.1 km/s in protomylonite and ultramylonite to 6.7 km/s in amphibole-rich ultramylonite and 7.0 km/s in mylonite. At maximum confining pressure of 400 MPa, protomylonite samples (7.4 km/s) and mylonite (7.6 km/s) revealed the highest velocity values. Ultramylonites show at 400 MPa notably lower values of maximum V_P (6.9 and 7.1 km/s).

P-WAVE VELOCITY DISTRIBUTION

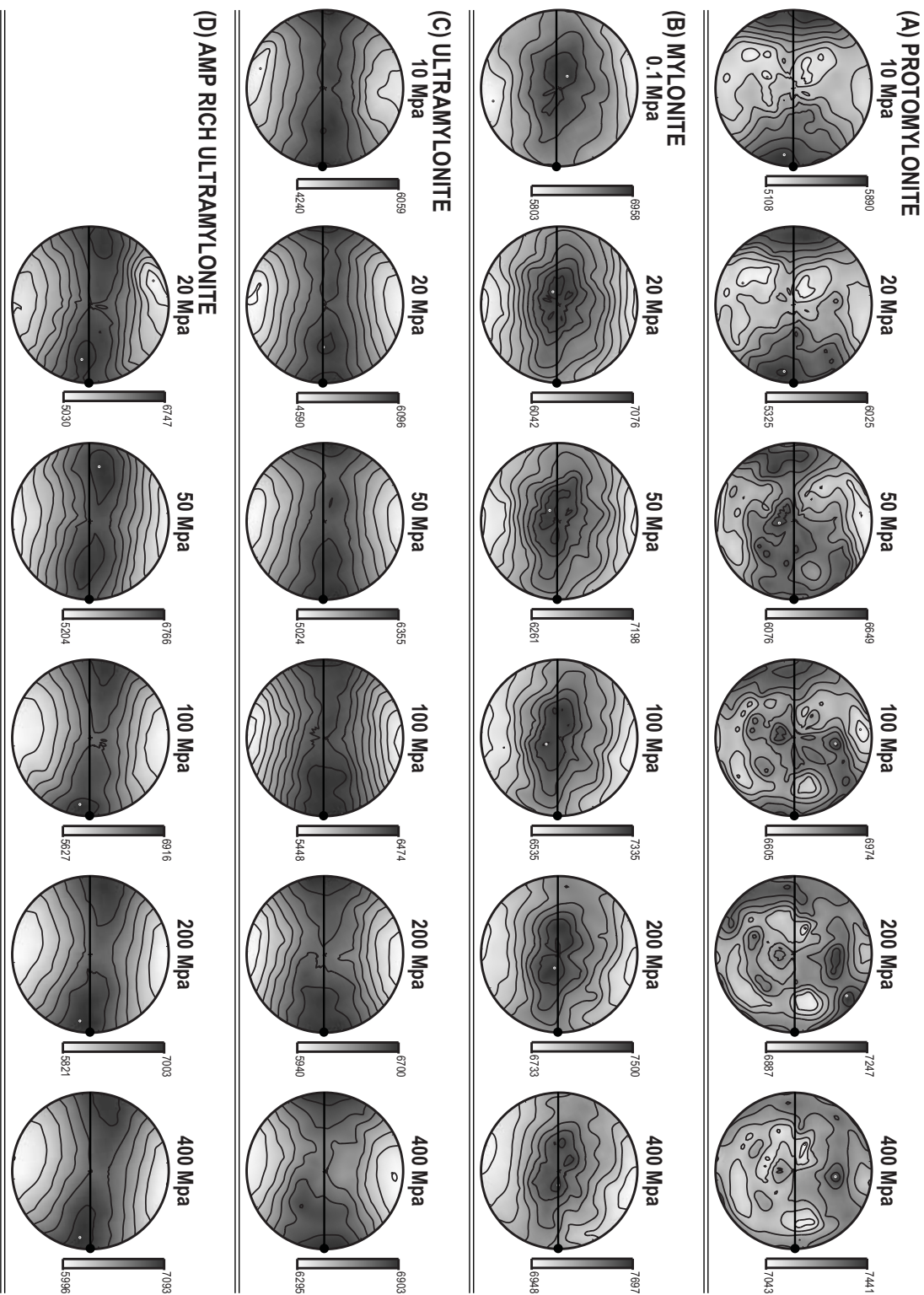


Figure IV.3. Results of measurements of P-wave velocity spatial distribution in a) protomylonite, b) mylonite, c) ultramylonite and d) amp-rich ultramylonite of Staré Město metagabbro. Diagrams are in the form of velocity isolines projected onto the lower hemisphere, equal area projection. Foliation is horizontal and lineation is in this plane in E-W direction.

Table IV.1 Summary of P-wave velocity measurements

	Pressure (MPa)	min V_P (ms^{-1})	max V_P (ms^{-1})	k (%)	average V_P (ms^{-1})
Protomylonite	10	5108	5890	14.2	5460
	20	5325	6025	12.3	5654
	50	6078	6648	9	6400
	100	6605	6974	5.4	6796
	200	6887	7247	5.1	7075
	400	7043	7441	5.5	7215
	0.1 ext.	6709	7184	6.8	6927
Mylonite	0.1	5803	6958	18.1	6374
	20	6042	7076	15.8	6532
	50	6261	7196	13.9	6695
	100	6535	7335	11.5	6880
	200	6733	7500	10.8	7085
	400	6948	7697	10.2	7241
	0.1 ext.	6513	7399	12.7	7010
Ultramylonite	10	4240	6059	35.3	5279
	20	4590	6096	28.2	5414
	50	5024	6355	23.4	5767
	100	5448	6474	17.2	6062
	200	5940	6700	12	6369
	400	6295	6903	9.2	6619
	0.1 ext.	5569	6518	15.7	6166
Amp rich Ultramylonite	20	5030	6747	29.2	5997
	50	5204	6766	26.1	6060
	100	5627	6916	20.6	6276
	200	5821	7003	18.4	6438
	400	5996	7093	16.8	6586
	0.1 ext.	5609	6974	21.7	6340

Pressure - confining pressure during experiment, min V_P and max V_P - minimum and maximum velocity, k - velocity anisotropy, average V_P - average velocity difference, 0.1 ext - extrapolated velocity

Results of extrapolation

Contour diagrams (Fig. IV.4) show that the $V_{P\text{max}}$ directions are oriented parallel to the lineation, while the $V_{P\text{min}}$ directions are perpendicular to the foliation in the mylonitic samples. In the amphibole-rich ultramylonite, $V_{P\text{max}}$ and $V_{P\text{min}}$ are slightly inclined with respect to the lineation and foliation. The protomylonite sample exhibits more scattered V_P distribution pattern with several submaxima forming incomplete girdle oblique to the foliation plane. $V_{P\text{max}}$ slightly increases from 7.2 km/s in the non-deformed protomylonite to 7.4 km/s in the mylonite and decreases to 6.5 km/s in the ul-

P-WAVE VELOCITY DISTRIBUTION EXTRAPOLATED TO 0.1 MPa

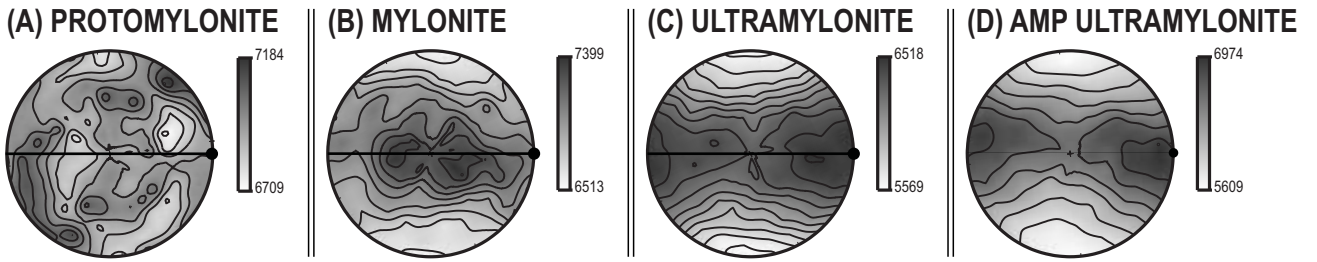


Figure IV.4. Results of measurements of P-wave velocity spatial distribution extrapolated to 0.1 MPa using the slope of linear velocity increase between 200 and 400 MPa.

tramylnite (Table IV.1). The amphibole-rich ultramylnite is characterized by maximum V_P of 7.0 km/s. The P-wave anisotropy increases from 6.8 % in the non-deformed protomylnit to 15.7 % in the ultramylnite up to 21.7 % in the amphibole-rich ultramylnite.

Table IV.2 Summary of difference between measured and calculated V_P distributions

	Calculated			Extrapolated to 0.1 Mpa			Difference	
	min V_P (ms^{-1})	max V_P (ms^{-1})	k (%)	min V_P (ms^{-1})	max V_P (ms^{-1})	k (%)	min V_P (ms^{-1})	max V_P (ms^{-1})
Protomylnite	6.41	6.94	8	6.71	7.12	6.8	-0.632	0.088
Mylonite	6.61	6.82	3.2	6.51	7.4	12.7	-0.642	0.113
Ultramylnite	6.36	6.85	7.4	5.57	6.56	15.7	0.195	0.852
Amp Ultramylnite	6.26	7.1	12.5	5.61	6.97	21.7	0.035	0.828

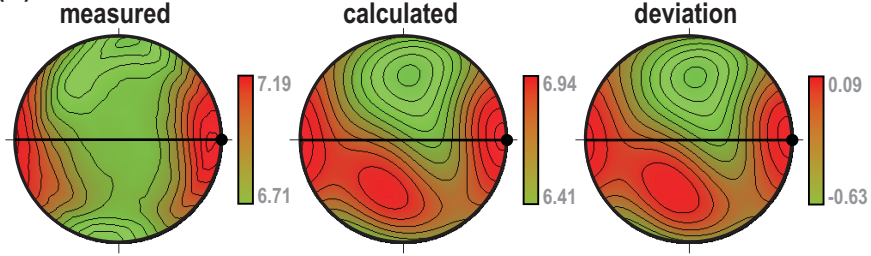
min V_P and max V_P - minimum and maximum velocity. k - velocity anisotropy

4.3.2. Numerical results

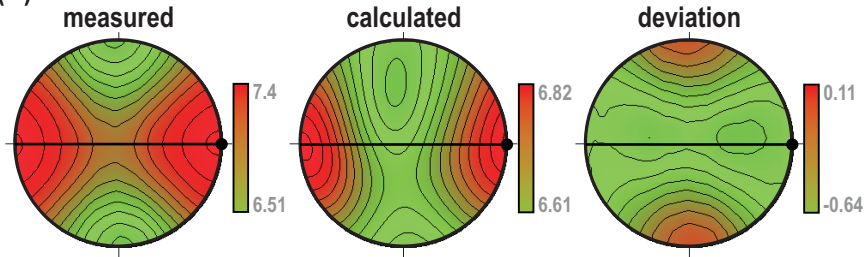
Contour diagrams of P-wave velocities calculated from CPO of plagioclase and amphibole exhibit similar distribution (Fig. IV.5) as diagrams of extrapolated measured velocities. Calculated $V_{P\text{max}}$ values in the weakly deformed protomylnit (6.9 km/s) and in the mylonite (6.8 km/s) are lower than measured values. The ultramylnite and amphibole-rich ultramylnite show higher calculated values of $V_{P\text{max}}$ (6.9 km/s and 7.1 km/s). The calculated anisotropies are significantly lower for all samples than those derived from the measured data (Fig. IV.6 and Table IV.2). Differential diagrams of measured and calculated P-wave velocities (Fig. IV.5) show in the protomylnit and amphibole-rich ultramylnite a pattern similar to that calculated

COMPARISON OF MEASURED AND CALCULATED V_p

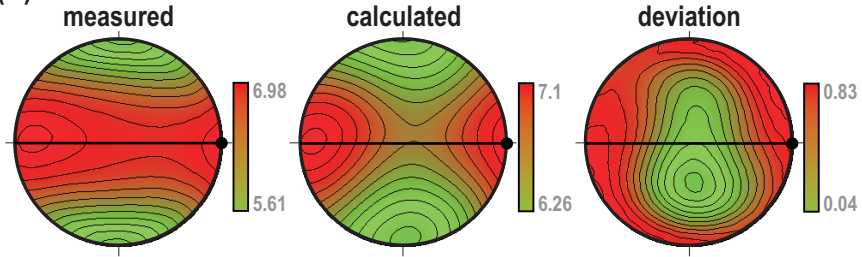
(A) PROTOMYLONITE



(B) MYLONITE



(C) ULTRAMYLONITE



(D) AMP RICH ULTRAMYLONITE

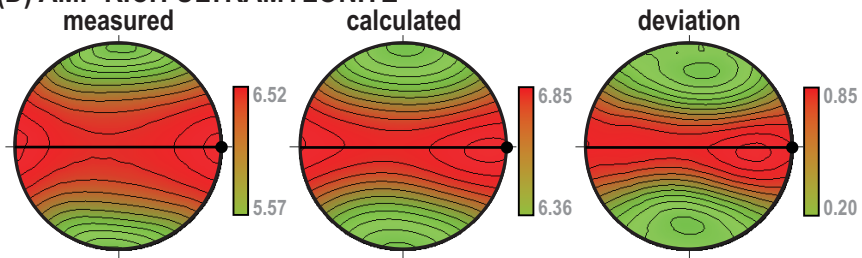


Figure IV.5. Contour diagrams of P-wave velocities calculated from CPO of plagioclase and amphibole together with diagrams of P-wave velocities extrapolated to 0.1 MPa and differential diagrams of measured and calculated P-wave velocities.

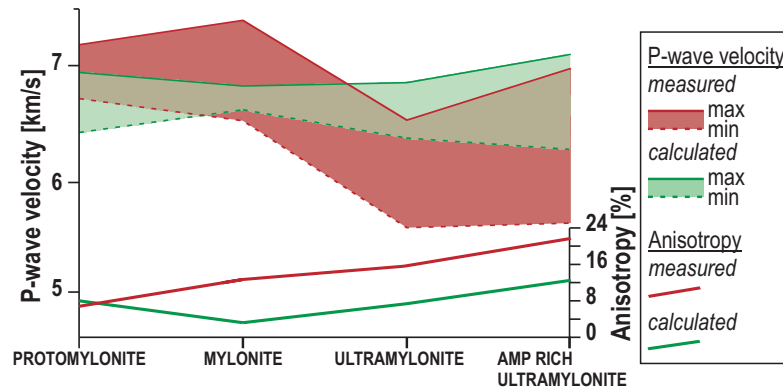


Figure IV.6. Pressure dependence of P-wave velocity maximum and minimum and anisotropy of Staré Město metagabbro.

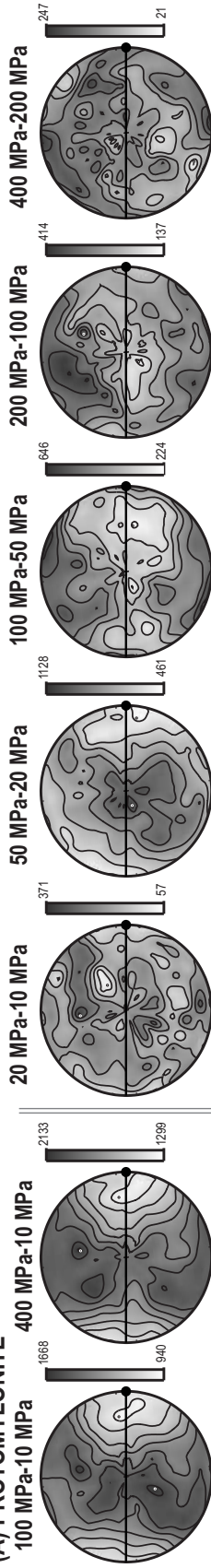
from the CPO of rock forming minerals. meaning that the maximum difference between measured and calculated V_P distributions is in high velocity area. The mylonite sample exhibits differential pattern which is virtually an inverse V_P distribution. The differential diagram of the ultramylonite shows pattern characterized by girdle of high differences perpendicular to the foliation and parallel to the lineation.

4.4. Pore space geometry

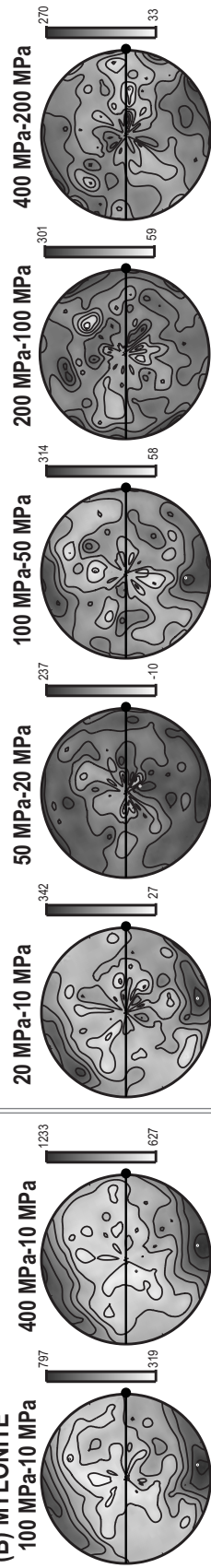
The bulk ΔV_P diagrams between 400 MPa and minimum confining pressure show in all samples a pattern which is in general virtually an inverse of V_P distribution at minimum pressure (Fig. IV.7). However, partial ΔV_P distribution diagrams between lower pressure steps (up to 100 MPa and 200 MPa in case of amphibole-rich ultramylonite) show in mylonite and ultramylonite samples difference from the general distribution. These samples reveal a presence of two more less discrete submaxima located approximately 10° to 30° out of direction normal to the foliation plane. In the protomylonite and mylonite, the partial ΔV_P diagrams show above 100 Mpa a scattered image. In ultramylonites above 100 MPa, the ΔV_P pattern similar to the general distribution of ΔV_P is observed. The anisotropy of P-wave velocity differences increases with increasing degree of mylonitic deformation and modal proportion of amphibole from the mylonite to the amphibole-

P-WAVE VELOCITY DIFFERENCES ($\Delta V_p(\Delta p)$) DISTRIBUTION

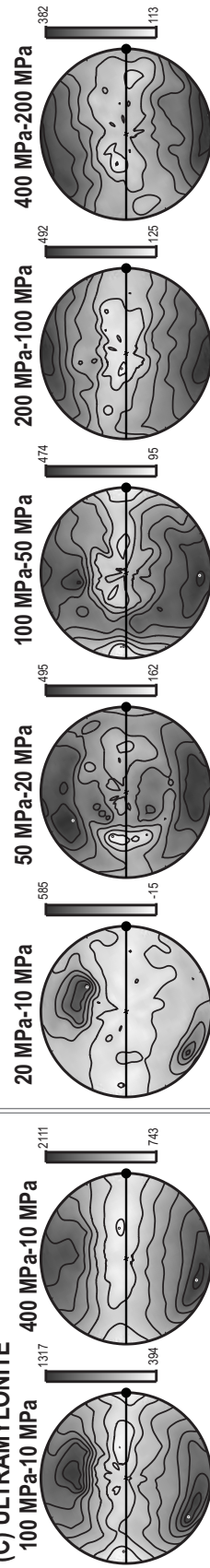
(A) PROTOMYLONITE



(B) MYLONITE



(C) ULTRAMYLONITE



(D) AMP RICH ULTRAMYLONITE

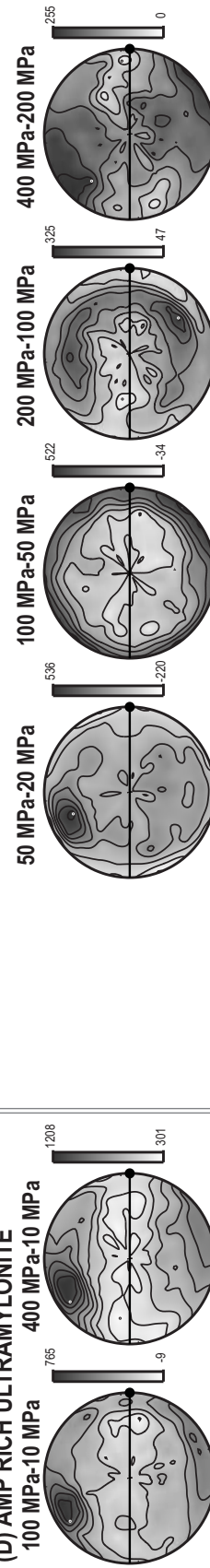


Figure IV.7. Stereodiagrams of the $\Delta V_p(\Delta p)$ dependence in space of a) protolith, b) protomylonite, c) ultramylonite and d) amp-rich ultramylonite of Staré Město metagabbro. It shows diagrams of each pair of subsequent sets of 3D measurements together with bulk difference of V_p between minimum pressure and 400 MPa.

Table IV.3 Summary of P-wave velocity differences

	Pressure (MPa)	min ΔV_P (ms ⁻¹)	max ΔV_P (ms ⁻¹)	A (%)	ΔV_P (ms ⁻¹)
Protomylonite	20-10	57	371	5.2	194
	50-20	461	1128	10	728
	100-50	224	646	6.1	414
	200-100	137	414	3.8	278
	400-200	21	247	3	140
	400-10	1299	2133	11.2	1755
	100-10	948	1668	9.7	1336
Mylonite	20-0.1	27	342	4.5	342
	50-20	-10	237	3.4	237
	100-50	58	314	3.5	314
	200-100	59	301	3.2	301
	400-200	33	270	3.1	270
	400-0	627	1233	7.9	1233
	100-0	319	797	6.2	797
Ultramylonite	20-10	-15	585	9.8	134
	50-20	162	495	5.2	353
	100-50	95	474	5.9	294
	200-100	125	492	5.5	306
	400-200	113	382	3.9	249
	400-10	743	2111	19.8	1339
	100-10	394	1317	13.4	782
Amp Ultramylonite	50-20	-220	536	11.2	62
	100-50	-34	522	8	216
	200-100	47	325	4	162
	400-200	0	255	3.6	147
	400-20	301	1208	12.8	588
	100-20	-9	765	10.9	278

Pressure - subtraction between indicated pressure levels, min ΔV_P and max ΔV_P - minimum and maximum of velocity difference, A - anisotropy of velocity difference, ΔV_P - average velocity difference.

rich ultramylonite (Table IV.3). On the other hand, the protomylonite sample is characterized by the anisotropy and the average velocity difference higher than in the mylonite close to the values of the ultramylonite. The dependence of anisotropy on the deformation state is also documented by the P-wave velocity differences among successive confining pressure levels. The ΔV_P distributions in the mylonitic samples between 100 MPa and minimum confining pressure together with ΔV_P partial diagrams suggest that the planar discontinuities causing the velocity differences at low confining pressure are preferentially oriented about 10° to 30° symmetrically oblique

to the foliation in the orientation parallel to the lineation. In the case of the protomylonite sample, the ΔV_P distributions show more complex pattern, which can be characterized by the lack of oriented pore space in high angles to the lineation.

4.5. Summary and Discussion

The spatial distribution and pressure dependence of P-wave velocities reveals the main difference between the protomylonite and mylonite samples of Staré Město metagabros. All mylonites preserve a similar P-wave velocity distribution with increasing confining pressure characterized by the concentration of high velocities parallel to the lineation and low velocities perpendicular to the foliation. The protomylonite sample shows a similar V_P distribution only at low confining pressure levels (up to 100 MPa). With increasing pressure, the pattern becomes scattered. All samples exhibit a significant decrease in anisotropy and an increase in maximum velocity with increasing confining pressure. The V_P anisotropy reveals also strong dependence on deformational stage of the samples. The maximum velocity increases from the protomylonite to the mylonite and substantially decreases in the ultramylonites. Data extrapolated to the atmospheric pressure exhibit similar trends and V_P patterns. The fabric and P-wave velocity properties of the studied samples correlate reasonably well with the results reported in the previous studies on amphibolites (Barberini et al., 2007; Siegesmund et al., 1989; Kern et al., 1997; Kern et al., 2008; Siegesmund and Kern, 1990; Barruol and Kern, 1996; Tatham et al., 2008).

The pore space geometry deduced from the $\Delta V_P(\Delta p)$ patterns suggests a mutually different organization of microcracks in the protomylonite and in the mylonites. The protomylonite is characterized by the radial preferred orientation of microcracks along the direction of the lineation and their closure at about 100 MPa of confining pressure. In the mylonitic samples, the $\Delta V_P(\Delta p)$ analysis determines two directions of preferred orientation of mi-

crocracks, about 10° to 30° symmetrically around the foliation parallel to lineation. The ΔV_P partial diagrams among the successive confining pressure levels suggest a closure of the most microcracks in these preferred orientations between 100 and 200 Mpa of confining pressure.

This study presents an important difference between the intrinsic anisotropy and the crack induced anisotropy in the metagabbro protomylonite and mylonites. At lower pressures, there is a significant effect of the microcracks on seismic properties in all samples (Barberini et al., 2007; Kern et al., 2008). The pore space geometry shows a direct relation to the structural framework of the rocks, even in the weakly deformed gabbro protomylonite. In the mylonite and ultramylonites, the intrinsic anisotropy and the crack induced anisotropy give rise to a constructive interference (Barberini et al., 2007). while in the protomylonite the intrinsic anisotropy significantly differs from the crack induced anisotropy observed at low confining pressures. The ΔV_P partial diagrams among the successive confining pressure levels suggest that the influence of crack induced anisotropy becomes less important above 100 Mpa. However, the large difference between the calculated and measured V_P anisotropy (extrapolated to 0.1MPa) associated with relatively low minimum velocity values observed in mylonitic samples indicate that even above confining pressure of 200 MPa the microcrack pore space remains open to some extent.

The pore space geometry generally reflects the microstructure of the studied metagabbros. The relation between the deformational rock fabric and the pore space geometry is documented even in the case of the protomylonite sample showing weak deformation as proved by the LPO of amphibole and plagioclase. However, the orientation of pore space is not exactly parallel to the foliation plane as suggested by previous investigations (Barberini et al., 2007; Siegesmund et al., 1989; Kern et al., 2008). In the weakly deformed sample, the micropores exhibit radial preferred orientation along the direction of lineation. In the more deformed samples, micropores become oriented in two directions symmetrically around the

foliation plane and parallel to the lineation. Such an orientation is likely induced by strongly linear fabric of amphibole in studied samples as evidenced by the microstructure and texture analysis (Baratoux et al., 2005). It is suggested that the micropores follow grain boundaries and cleavage planes of amphibole, which are the best oriented planes of weakness allowing cracks to develop and propagate to form the large intergranular cracks which are most likely responsible for the preferential pore space geometry.

The V_P values calculated from the lattice preferred orientation of plagioclase and amphibole exhibit substantial differences in the velocity values. The protomylonit and mylonite show maximum V_P values lower (by about 0.6 km/s) than those obtained by the linear extrapolation of measured values. In contrast, the ultramylonites show slightly higher calculated maximum of V_P values but significantly lower V_P minimum values by about 0.8 km/s. The V_P anisotropy values are similar in the protomylonit sample, while the mylonitic samples reveal significantly lower calculated values. Despite the above mentioned differences, the calculated and measured V_P patterns exhibit the similar spatial distributions. The comparison of measured and calculated P-wave velocities indicate that the amphibole lattice preferred orientation (LPO) is responsible for the most of the rock anisotropy. The role of plagioclase depends on the strength and orientation of its LPO. The results of numerical calculation of P-wave velocities give generally reasonable estimates when compared to the measured data. However, the measured P-wave velocity anisotropies are systematically higher in comparison to the calculated values. The discrepancy in anisotropy of the mylonitic samples is interpreted in terms of the microstructural features such as mineral layering, grain boundary preferred orientation and possible presence of unclosed microcracks oriented parallel to the foliation at high confining pressures. The significantly higher maximum velocity in the protomylonit and mylonite suggests potentially incorrect amphibole elastic constants due to its different chemical composition.

4.6. Conclusions

Using a combination of measurement of lattice preferred orientation, measurements of P-wave velocity distribution in space, subsequent analysis of difference of P-wave velocity measured at different levels of confining pressure and numerically obtained velocity distribution we document relation of pore space geometry and P-waves to deformational stage of the metagabbro samples.

The V_P anisotropy reveals strong dependence on deformational stage of the samples. Significant effect of the microcracks on seismic properties at lower pressures is documented in all samples. In the metagabbro protomylonite an important difference between the intrinsic anisotropy and the crack induced anisotropy was observed. In the mylonite and ultramylonites, the intrinsic anisotropy and the crack induced anisotropy give rise to a constructive interference.

The comparison of measured and calculated P-wave velocities indicate that the amphibole lattice preferred orientation (LPO) is responsible for the most of the rock anisotropy. The measured P-wave velocity anisotropies are systematically higher in comparison to the calculated values. The discrepancy in anisotropy of the mylonitic samples is interpreted in terms of the microstructural features, mainly the possible presence of unclosed microcracks oriented parallel to the foliation at high confining pressures.

The pore space geometry generally reflects the microstructure of the studied metagabbros. The relation between the deformational rock fabric and the pore space geometry is documented even in the case of the protomylonite sample showing weak deformation. However, the orientation of pore space is not exactly parallel to the foliation plane. In the more deformed samples, micropores become oriented in two directions symmetrically around the foliation plane and parallel to the lineation. Such an orientation is likely induced by strongly linear fabric of amphibole in studied samples. It is suggested that the micropores follow grain boundaries and

cleavage planes of amphibole. The large difference between the calculated and measured V_P anisotropy (extrapolated to 0.1 MPa) associated with relatively low minimum velocity values observed in mylonitic samples indicate that even above confining pressure of 200 MPa the microcrack pore space remains open to some extent.

5. Summary

The thesis purpose was identification and semiquantitative estimation of pore space geometry in rocks using combination of indirect and direct methods of physical and microstructural investigation. Influence of different rock structure aspects (grain size of mineral grains, contribution of individual microstructures, role of original magmatic and/or metamorphic microstructure and brittle structure of rock massif) on pore space geometry evolution was studied. Three examples of rock types were examined: two microstructurally distinct eclogites (Chapter II), three microstructural varieties of granites from Melechov massif (Chapter III) and four stages of progressive deformation of metagabbro from the Staré Město belt (Chapter IV). Combination of quantitative microstructural analysis of grains, grain boundaries and microcrack network, measurement of lattice preferred orientation and measurements of elastic velocities at increasing confining pressure turned out to be effective in evaluation of preferred orientation of the pore space in rock samples. Together with information about porosity and permeability these analysis represents solid methodology for determination of zones of potentially high risk of fluid infiltration to the rock mass. For the purposes of this thesis was developed new Fracture network analysis toolbox for MATLAB™ FractNetLX (Ondrej Lexa (c) 2010) in order to the quantification of microcracks in rock samples.

Relation of microstructure and pore space geometry

In studied eclogites the microporosity is related to cracks at grain boundaries and cleavage cracks ((110) planes) in clinopyroxene. The grain bound-

aries have much stronger influence on orientation and amount of microporosity than the cleavage plane. With increasing confining pressure, grain boundaries close below 50 MPa, while cleavage planes in clinopyroxene remain open up to 100 MPa. Orientation of microporosity mostly depends on preferred orientation of grain boundaries and less on orientation of cleavage planes in clinopyroxene. In Melechov granites the pore space geometry reflects the orientation of exfoliation planes in coarse-grained granite. However, in medium-grained and fine-grained granite the, pore space is preferentially oriented 20° to 40° oblique to the closest macrofracture. Microcrack preferred orientation is in agreement with pore space geometry deduced from distribution of P-wave velocity differences, being mostly perpendicular to the maximum of P-wave velocity differences. The most important crack type in terms of fabric strength and interconnectivity is intergranular crack. The analysis of connected networks of microcrack show high importance of intergranular cracks for network connectivity and negligible influence of cracks in mica. In metagabbro rocks the pore space geometry generally reflects the microstructure. The relation between the deformational rock fabric and the pore space geometry is documented even in the case of the protomylonit sample showing weak deformation. However, the orientation of pore space is not exactly parallel to the foliation plane. In the more deformed samples, micropores become oriented in two directions symmetrically around the foliation plane and parallel to the lineation. Such an orientation is likely induced by strongly linear fabric of amphibole in studied samples. It is suggested that the micropores follow grain boundaries and cleavage planes of amphibole. The large difference between the calculated and measured V_p anisotropy (extrapolated to 0.1 MPa) associated with relatively low minimum velocity values observed in mylonitic samples indicate that even above confining pressure of 200 MPa the microcrack pore space remains open to some extend.

Pore space geometry vs. brittle structure of Melechov massif

In general view the pore space preferably formed by planar microcracks does not reflect the observed geometry of macroscopic fractures in the Melechov massif. More likely is the explanation that microcracks forming preferred orientation developed in process zone of closest macrofracture during its propagation and/or reactivation (Scholz et al., 1993; Vermilye and Scholz, 1998; Wilson et al., 2003). Microfracture orientation in fracture process zone corresponds to stress field orientation during fracture propagation and reactivation. The stress field orientation depends on mode of propagation or reactivation (Scholz et al., 1993).

Porosity and permeability relation in Melechov granites

Porosity and observed average velocity difference shows a correlation with the grain size of granite. Permeability in studied granites shows significant decrease up to two orders of magnitude with increasing effective pressure from 0.5 MPa to 10 MPa. Established permeability directional dependence corresponds to preferred orientation of microcracks perpendicular to the maximum P-wave velocities difference. The highest permeability measured at the minimum confining pressure correlates with the maximum density of microcracks.

References

- Åkesson, U., J. Hansson, and J. Stigh (2004), Characterisation of microcracks in the Bohus granite, western Sweden, caused by uniaxial cyclic loading, *Engineering Geology*, 72 (1-2), 131-142, doi:10.1016/j.enggeo.2003.07.001.
- Aleksandrov, K., and T. Ryzhova (1961), The elastic properties of rock forming minerals, 1. pyroxenes and amphibolites, *Izv. Acad. Sci. USSR, Geophys. Ser.*, 16 (4), 795-815.
- Anders, M., and D. Wiltschko (1994), Microfracturing, paleostress and the growth of faults, *Journal of Structural Geology*, 16 (6), 795-815.
- Babuška, V., and Z. Pros (1977), Effect of fabric and cracks on the elastic anisotropy in granodiorite, *Inst. Geophys. Pol. Acad. Sci.*, A-6,(117), 179- 186.
- Babuška, V., and Z. Pros (1984), Velocity anisotropy in granodiorite and quartzite due to the distribution of microcracks, *Geophysical Journal of The Royal Astronomical Society*, 76 (1), 121.
- Babuška, V., J. Fiala, M. Kumazawa, I. Ohno, and Y. Sumino (1978), Elastic properties of garnet solid-solution series, *Physics of The Earth and Planetary Interiors*, 16 (2), 157-176.
- Baratoux, L., K. Schulmann, S. Ulrich, and O. Lexa (2005), Contrasting microstructures and deformation mechanisms in metagabbro mylonites contemporaneously deformed under different temperatures (c. 650 degrees C and c. 750 degrees C), in *Deformation Mechanisms*,

Rheology and Tectonics: From Minerals to the Lithosphere, Geological Society Special Publication, vol. 243, edited by Gapais, D and Brun, JP and Cobbold, PR, pp. 97-125.

- Barberini, V., L. Burlini, and A. Zappone (2007), Elastic properties, fabric and seismic anisotropy of amphibolites and their contribution to the lower crust reflectivity, *Tectonophysics*, 445 (3-4), 227-244, doi:10.1016/j.tecto.2007.08.017.
- Barruol, G., and H. Kern (1996), Seismic anisotropy and shear-wave splitting in lower-crustal and upper-mantle rocks from the Ivrea Zone - Experimental and calculated data, *Physics of The Earth and Planetary Interiors*, 95 (3-4), 175-194.
- Batzle, M., G. Simmons, and R. Siegfried (1980), Microcrack closure in rocks under stress - direct observation, *Journal of Geophysical Research* , 85 (NB12), 7072-7090.
- Benson, P., A. Schubnel, S. Vinciguerra, C. Trovato, P. Meredith, and R. Young (2006a), Modeling the permeability evolution of microcracked rocks from elastic wave velocity inversion at elevated isostatic pressure, *Journal of Geophysical Research - Solid Earth* , 111 (B4), doi: 10.1029/2005JB003710. 1
- Benson, P. M., P. G. Meredith, and A. Schubnel (2006b), Role of void space geometry in permeability evolution in crustal rocks at elevated pressure, *Journal of Geophysical Research - Solid Earth* , 111 (B12), doi: 10.1029/2006JB004309.
- Birch, F. (1960), The velocity of compressional waves in rocks to 10-kilobars .1., *Journal of Geophysical Research*, 65 (4), 1083-1102.
- Birch, F. (1961), Velocity of compressional waves in rocks to 10 kilobars, .2., *Journal of Geophysical Research* , 66 (7), 2199-2224.

- Bouchez, J. (2000), Magnetic susceptibility anisotropy and fabrics in granites, *Comptes Rendus De L Academie Des Sciences Serie Ii Fascicule A-Sciences De La Terre Et Des Planetes*, 330 (1), 1-14.
- Brace, W. (1965), Relation of elastic properties of rocks to fabric, *Journal of Geophysical Research* , 70 (22), 5657-5667.
- Brace, W., and A. Orange (1968), Electrical resistivity changes in saturated rocks during fracture and frictional sliding, *Journal of Geophysical Research* , 73 (4), 1433.
- Breiter, K., I. Gnojek, and M. Chlupáčová (1998), Radiometric patterns constraints for the magmatic evolution of the two-mica granites in the Central Moldanubian Pluton , *Bulletin of the Czech Geological Institute* , 73 , 301- 311.
- Bruhn, R., W. Yonkee, and W. Parry (1990), Structural and fluid-chemical properties of seismogenic normal faults, *Tectonophysics*, 175 (1-3), 139-157.
- Caine, J., J. Evans, and C. Forster (1996), Fault zone architecture and permeability structure, *Geology*, 24 (11), 1025-1028.
- Chester, F., J. Evans, and R. Biegel (1993), Internal structure and weakening mechanisms of the san-andreas fault, *Journal of Geophysical Research - Solid Earth*, 98 (B1), 771-786.
- Chu, C., C. Wang, and W. Lin (1981), Permeability and frictional-properties of San-Andreas fault gouges, *Geophysical Research Letters*, 8 (6), 565-568.
- David, C., B. Menendez, and M. Darot (1999), Influence of stress-induced and thermal cracking on physical properties and microstructure of La Peyratte granite, *International Journal Of Rock Mechanics and Mining Sciences*, 36 (4), 433-448.

- Evans, J., C. Forster, and J. Goddard (1997), Permeability of fault-related rocks, and implications for hydraulic structure of fault zones, *Journal of Structural Geology*, 19 (11), 1393-1404.
- Faulkner, D., and E. Rutter (1998), The gas permeability of claybearing fault gouge at 20°C in faults, fault sealing and fluid flow in hydrocarbon reservoirs , pp. 147-156.
- Forster, C., and J. Evans (1991), Hydrogeology of thrust faults and crystalline thrust sheets - results of combined field and modeling studies, *Geophysical Research Letters*, 18 (5), 979-982.
- Fountain, D., T. Boundy, H. Austrheim, and P. Rey (1994), Eclogite-facies shear zones deep crustal reflectors? *Tectonophysics*, 232 (1-4), 411-424.
- Freund, D., and G. Nover (1995), Hydrostatic-pressure tests for the permeability-formation factor Relation on crystalline rocks from the ktb drilling project, *Surveys in Geophysics*, 16 (1), 47-62.
- Fyfe, N., W.S. and Price, and A. Thompson (1978), Brittle fracture in two crystalline rocks under true triaxial compressive stresses, Elsevier Sci. Publ. Co. Amsterdam, 372 pp.
- Gerdes, A., G. Friedl, P. R.R., and F. Finger (2003), High-resolution geochronology of Variscan granite emplacement - the South Bohemian Batholith , *Journal of the Czech Geological Society* , 48 , 53-54.
- Glover, P., J. Gomez, P. Meredith, K. Hayashi, P. Sammonds, and M. S.A.F. (1997), Damage of saturated rocks undergoing triaxial deformation using complex electrical conductivity measurements: experimental results , *Physics and Chemistry of the Earth* , 22 (1-2), 57-61.
- Gueguen, Y., and J. Dienes (1989), Transport-properties of rocks from statistics and percolation, *Mathematical Geology*, 21 (1), 1-13.

- Gueguen, Y., and A. Schubnel (2003), Elastic wave velocities and permeability of cracked rocks, *Tectonophysics*, 370 (1-4), 163-176, doi: 10.1016/S0040-1951(03)00184-7.
- Gueguen, Y., T. Chelidze, and M. LeRavalec (1997), Microstructures, percolation thresholds, and rock physical properties, *Tectonophysics*, 279 (1-4), 23-35.
- Gurney, J. J., and A. Menzies (1998), The Newlands kimberlite pipes and dyke complex , in *Small Mines Field Excursion guide* , 7th International Kimberlite Conference. Cape Town, South Africa, vol. , pp. 23-30.
- Haimson, B., and C. Chang (2005), Brittle fracture in two crystalline rocks under true triaxial compressive stresses, in *Petrophysical Properties of Crystalline Rocks*, Geological Society Special Publication, vol. 240, edited by Harvey, PK and Brewer, TS and Pezard, PA and Petrov, VA, pp. 47-59.
- Jelínek, V. (1981), Characterization of the magnetic fabric of rocks, *Tectonophysics*, 79 (3-4), T63-T67.
- Jelínek, V., and J. Pokorný (1997), Some new concepts in technology of transformer bridges for measuring susceptibility anisotropy of rocks , *Physics and Chemistry of the Earth* , 22 , 179-181.
- Kachanov, M. (1994), Elastic solids with many cracks and related problems, *Advances In Applied Mechanics*, 30, 259-445.
- Kanaori, Y., K. Yairi, and T. Ishida (1991), Grain-boundary microcracking of granite rocks from the northeastern region of the Atotsugawa fault, Central Japan - SEM backscattered electron images, *Engineering Geology*, 30 (2), 221- 235.
- Kano, S., and N. Tsuchiya (2002), Parallelepiped cooling joint and anisotropy

- of P-wave velocity in the Takidani granitoid, Japan Alps, *Journal of Volcanology and Geothermal Research*, 114 (3-4), 465-477.
- Katz, O., Z. Reches, and G. Baer (2003), Faults and their associated host rock deformation: Part I. Structure of small faults in a quartz-syenite body, southern Israel, *Journal of Structural Geology*, 25 (10), 1675-1689, doi: 10.1016/S0191-8141(03)00011-7.
 - Kern, H., B. Liu, and T. Popp (1997), Relationship between anisotropy of P and S wave velocities and anisotropy of attenuation in serpentinite and amphibolite, *Journal of Geophysical Research - Solid Earth*, 102 (B2), 3051- 3065.
 - Kern, H., T. Popp, F. Gorbatshevich, A. Zharikov, K. Lobanov, and Y. Smirnov (2001), Pressure and temperature dependence of V-P and V-S in rocks from the superdeep well and from surface analogues at Kola and the nature of velocity anisotropy, *Tectonophysics*, 338 (2), 113-134.
 - Kern, H., T. I. Ivankina, A. N. Nikitin, T. Lokajíček, and Z. Pros (2008), The effect of oriented microcracks and crystallographic and shape preferred orientation on bulk elastic anisotropy of a foliated biotite gneiss from Outokumpu, *Tectonophysics*, 457 (3-4), 143-149, doi:10.1016/j.tecto.2008.06.015.
 - Kerrich, R. (1986), Fluid infiltration into fault zones - chemical, isotopic, and mechanical effects, *Pure and Applied Geophysics*, 124 (1-2), 225-268.
 - Klápová, H., J. Konopásek, and K. Schulmann (1998), Eclogites from the Czech part of the Erzgebirge: multi-stage metamorphic and structural evolution, *Journal of The Geological Society*, 155 (Part 3), 567-583.
 - Kowallis, B., H. Wang, and B. Jang (1987), Healed microcrack orienta-

tions in granite from illinois borehole uph-3 and their relationship to the rocks stress history, *Tectonophysics*, 135 (4), 297-306.

- Kranz, R. (1983), Microcracks in rocks - a review, *Tectonophysics*, 100 (1-3), 449-480.
- Kumazawa, M., H. Helmstaedt, and K. Masaki (1971), Elastic properties of eclogite xenoliths from diatremes of East Colorado plateau and their implication to upper mantle structure, *Journal of Geophysical Research* , 76 (5), 1231-1247.
- LeRavalec, M., Y. Gueguen, and T. Chelidze (1996), Elastic wave velocities in partially saturated rocks: Saturation hysteresis, *Journal of Geophysical Research - Solid Earth* , 101 (B1), 837-844.
- Lexa, O. (2010), FracNetLX - Fracture network analysis toolbox for MATLAB, <http://petrol.natur.cuni.cz/ondro/FractNetLX> , .
- Lexa, O., and K. Schulmann (2005), Strukturní dokumentace a vyhodnocení vrtných prací MEL-3 a MEL-4 a detailní strukturní výzkum na loklitě Holý vrch , in *Dílčí zpráva* , edited by RAWA ,
- Lexa, O., P. Štípska, K. Schulmann, L. Baratoux, and A. Kroner (2005), Contrasting textural record of two distinct metamorphic events of similar P-T conditions and diferent durations, *Journal of Metamorphic Geology*, 23 (8), 649-666, doi:10.1111/j.1525-1314.2005.00601.x.
- Liu, S., A. H. M. F. Anwar, B. Kim, and Y. Ichikawa (2006), Observation of microcracks in granite using a confocal laser scanning microscope, *International Journal of Rock Mechanics and Mining Sciences*, 43 (8), 1293-1305, doi:10.1016/j.ijrmms.2006.04.006.
- Lloyd, G., N. Schmidt, D. Mainprice, and D. Prior (1991), Crystallographic textures, *Mineralogical Magazine*, 55 (380), 331-345.
- Lockner, H., D.and Naka, H. Tanaka, H. Ito, and R. Ikeda (2000), Permeability and strength of the Nojima core samples from the Nojima

fault of the 1995 Kobe earthquake , in Proceedings of the International Workshop on the Nojima Fault Core and and Borehole Data Analysis , edited by Ito, H. and Fujimoto, K. and Tanaka, H. and Lockner, D. , 147-152.

- Lockner, J., D.A .and Byerlee (1985), Complex resistivity measurements of confined rock, *Journal of Geophysical Research* , 90 (NB9), 7837-7847.
- Machek, M., P. Špaček, S. Ulrich, and F. Heidelbach (2007), Origin and orientation of microporosity in eclogites of diferent microstructure studied by ultrasound and microfabric analysis, *Engineering Geology*, 89 (3-4), 266-277, doi:10.1016/j.enggeo.2006.11.001.
- Mainprice, D. (2005), The unicef careware petrophysical software package. ftp://www.gm.univ-montp2.fr/mainprice//CareWare_Unicef_Programs.
- Mauler, A., L. Burlini, K. Kunze, P. Philippot, and J. Burg (2000), P-wave anisotropy in eclogites and relationship to the omphacite crystallographic fabric, *Physics and Chemistry of The Earth Part A-Solid Earth and Geodesy*, 25 (2), 119-126.
- McCaig, A. (1988), Deep fluid circulation in fault zones, *Geology*, 16 (10), 867- 870.
- Menendez, B., C. David, and A. Nistal (2001), Confocal scanning laser microscopy applied to the study of pore and crack networks in rocks, *Computers & Geosciences*, 27 (9), 1101-1109.
- Moore, D., and D. Lockner (1995), The role of microcracking in shear-fracture propagation in granite, *Journal of Structural Geology* , 17 (1), 95-114.
- Nasser, M. H. B., A. Schubnel, and R. P. Young (2007), Coupled evolutions of fracture toughness and elastic wave velocities at high crack density in thermally treated Westerly granite, *International Journal of*

Rock Mechanics and Mining Sciences, 44 (4), 601-616, doi:10.1016/j.ijrmms.2006.09.008.

- Onishi, C., and I. Shimizu (2005), Microcrack networks in granite affected by a fault zone: Visualization by confocal laser scanning microscopy, *Journal of Structural Geology*, 27 (12), 2268-2280, doi:10.1016/j.jsg.2005.07.007.
- Peach, C., and C. Spiers (1996), Influence of crystal plastic deformation on dilatancy and permeability development in synthetic salt rock, *Tectonophysics*, 256 (1-4), 101-128.
- Petrov, V. A., et al. (2005), Microstructure, filtration, elastic and thermal properties of granite rock samples: implications for HLW disposal, in *Petrophysical Properties of Crystalline Rocks*, Geological Society Special Publication, vol. 240, edited by Harvey, PK and Brewer, TS and Pezard, PA and Petrov, VA, pp. 237-253.
- Pezard, P., and et al. (1999), Physical properties of granite, with application to nuclear waste storage in subsurface, in *Textures and Physical Properties of Rocks. Gottinger Arbeiten zur Geologie und palaontologie Geologische Institute, Universitat Gottingen*, edited by Leiss, B. and Ullemeyer, K. and Weber, K., 149-151.
- Plumb, R., T. Engelder, and D. Yale (1984), Near-surface insitu stress .3. correlation with microcrack fabric within the New-Hampshire granites, *Journal of Geophysical Research*, 89 (NB11), 9350-9364.
- Popp, T., and H. Kern (2000), Monitoring the state of microfracturing in rock salt during deformation by combined measurements of permeability and P- and S- wave velocities, *Physics and Chemistry of The Earth Part A-Solid Earth and Geodesy*, 25 (2), 149-154.
- Přikryl, R., K. Klíma, T. Lokajíček, and Z. Pros (2005), Non-linearity in multidirectional P-wave velocity: confining pressure behaviour based

- on real 3D laboratory measurements, and its mathematical approximation, in *Petrophysical Properties of Crystalline Rocks*, Geological Society Special Publication, vol. 240, edited by Harvey, PK and Brewer, TS and Pezard, PA and Petrov, VA, 323-334.
- Přikryl, R., T. Lokajíček, Z. Pros, and K. Klíma (2007), Fabric symmetry of low anisotropic rocks inferred from ultrasonic sounding: Implications for the geomechanical models, *Tectonophysics*, 431 (1-4), 83-96, doi: 10.1016/j.tecto.2006.05.031. 6
 - Procházka, V., and D. Matějka (2006), Rock-forming accessory minerals in the granites of Melechov massif, *Acta. Univ. Carol. Geol.*, 48, 71-79.
 - Pros, Z., and V. Babuška (1968), An apparatus for investigating elastic anisotropy on spherical rock samples, *Studia Geophysica et Geodaetica*, 12 (2), 192-198.
 - Pros, Z., T. Lokajíček, and K. Klíma (1998), Laboratory approach to the study of elastic anisotropy on rock samples, *Pure and Applied Geophysics*, 151 (2-4), 619-629.
 - Rasolofosaon, P., W. Rabbel, S. Siegesmund, and A. Vollbrecht (2000), Characterization of crack distribution: fabric analysis versus ultrasonic inversion, *Geophysical Journal International*, 141 (2), 413-424.
 - Reuschle, T., S. Haore, and A. Darot (2003), Microstructural control on the elastic properties of thermally cracked granite, *Tectonophysics*, 370 (1-4), 95- 104, doi:10.1016/S0040-1951(03)00179-3.
 - Rooney, T., R. Riecker, and A. Gavasci (1975), Hornblende deformation features, *Geology*, 3 (7), 364-366.
 - Rufet, C., Y. Gueguen, and M. Darot (1991), Complex conductivity measurements and fractal nature of porosity, *Geophysics*, 56 (6), 758-768.

- Sayers, C., and M. Kachanov (1995), Microcrack-induced elastic-wave anisotropy of brittle rocks, *Journal of Geophysical Research - Solid Earth* , 100 (B3), 4149-4156.
- Schild, M., S. Siegesmund, A. Vollbrecht, and M. Mazurek (2001), Characterization of granite matrix porosity and pore-space geometry by in situ and laboratory methods, *Geophysical Journal International*, 146 (1), 111-125.
- Schmidt, N., and N. Olesen (1989), Computer-aided determination of crystallattice orientation from electron-channeling patterns in the SEM, *Canadian Mineralogist*, 27 (Part 1), 15-22.
- Scholz, C. (1968a), Microfracturing and inelastic deformation of rock in compression, *Journal of Geophysical Research* , 73 (4), 1417.
- Scholz, C. (1968b), Experimental study of fracturing process in brittle rock, *Journal of Geophysical Research* , 73 (4), 1447.
- Scholz, C., N. Dawers, and M. Yu, J.Z. and Anders (1993), Fault growth and fault scaling laws - preliminary-results, *Journal of Geophysical Research - Solid Earth* , 98 (B12), 21,951-21,961.
- Schubnel, A., and Y. Gueguen (2003), Dispersion and anisotropy of elastic waves in cracked rocks, *Journal of Geophysical Research - Solid Earth* , 108 (B2), doi:10.1029/2002JB001824. 7
- Schubnel, A., P. M. Benson, B. D. Thompson, J. F. Hazzard, and R. P. Young (2006), Quantifying damage, saturation and anisotropy in cracked rocks by inverting elastic wave velocities, *Pure and Applied Geophysics*, 163 (5-6), 947- 973, doi:10.1007/s00024-006-0061-y.
- Schulmann, K., Z. Venera, J. Konopásek, and O. Lexa (1998), Structural and geological investigation of the Melechov massif (in Czech) , MS Faculty of Science of the Charles University, Geofond P 93389, .

- Schulze, O., T. Popp, and H. Kern (2001), Development of damage and permeability in deforming rock salt, *Engineering Geology*, 61 (2-3), 163-180.
- Selverstone, J., G. Morteau, and J. Staude (1991), Fluid channeling during ductile shearing - transformation of granodiorite into aluminous schist in the Tauern window, Eastern Alps, *Journal of Metamorphic Geology*, 9 (4), 419- 431.
- Seront, B., D. Mainprice, and N. Christensen (1993), A determination of the 3-dimensional seismic properties of anorthosite - comparison between values calculated from the petrofabric and direct laboratory measurements, *Journal of Geophysical Research - Solid Earth* , 98 (B2), 2209-2221.
- Seront, B., T. Wong, J. Caine, C. Forster, R. Bruhn, and J. Fredrich (1998), Laboratory characterization of hydromechanical properties of a seismogenic normal fault system, *Journal of Structural Geology*, 20 (7), 865-881.
- Sibson, R., F. Robert, and K. Poulsen (1988), High-angle reverse faults, fluidpressure cycling, and mesothermal gold-quartz deposits, *Geology*, 16 (6), 551- 555.
- Siegesmund, S. (1996), The significance of rock fabrics for the geological interpretation of geophysical anisotropies , *Geotekt. Forsch.* , 85 , 1-123.
- Siegesmund, S., and A. Vollbrecht (1991), Complete seismic properties obtained from microcrack fabrics and textures in an amphibolite from the ivrea zone, western alps, italy, *Tectonophysics*, 199 (1), 13-24.
- Siegesmund, S., T. Takeshita, and H. Kern (1989), Anisotropy of Vp and Vs in an amphibolite of the deeper crust and its relationship to the

mineralogical, microstructural and textural characteristics of the rock, *Tectonophysics*, 157 (1- 3), 25-38.

- Siegesmund, S., A. Vollbrecht, and G. Nover (1991), Anisotropy of compressional wave velocities, complex electrical-resistivity and magnetic-susceptibility of mylonites from the deeper crust and their relation to the rock fabric, *Earth and Planetary Science Letters*, 105 (1-3), 247-259.
- Siegesmund, S., A. Vollbrecht, and Z. Pros (1993), Fabric changes and their influence on p-wave velocity patterns - examples from a polyphase deformed orthogneiss, *Tectonophysics*, 225 (4), 477-492. 8
- Simmons, G., and W. Brace (1965), Comparison of static and dynamic measurements of compressibility of rocks, *Journal of Geophysical Research* , 70 (22), 5649-56.
- Simmons, G., and D. Richter (1976), Microcracks in rock, in *The Physics and chemistry of minerals and rocks*. Wiley, New Yourk, N.Y. , edited by Strens, R.G.J., 105-137.
- Simpson, G., Y. Gueguen, and F. Schneider (2001), Permeability enhancement due to microcrack dilatancy in the damage regime, *Journal of Geophysical Research - Solid Earth* , 106 (B3), 3999-4016.
- Špaček, P., and R. Melichar (2005), Seismic velocities in rocks: numerical comparison of calculated data with experiment , *Geolines* , 19 , 110.
- Štípská, P., K. Schulmann, A. Thompson, J. Ježek, and A. Kröner (2001), Thermo-mechanical role of a Cambro-Ordovician paleorift during the Variscan collision: the NE margin of the Bohemian Massif, *Tectonophysics*, 332 (1-2), 239-253.
- Takemura, T., and M. Oda (2004), Stereology-based fabric analysis of microcracks in damaged granite, *Tectonophysics*, 387 (1-4), 131-150,

doi: 10.1016/j.tecto.2004.06.004.

- Takemura, T., A. Golshani, M. Oda, and K. Suzuki (2003), Preferred orientations of open microcracks in granite and their relation with anisotropic elasticity, *International Journal of Rock Mechanics and Mining Sciences*, 40 (4), 443-454, doi:10.1016/S1365-1609(03)00014-5.
- Takeshita, T., and K. Yagi (2001), Paleostress orientation from 3-D orientation distribution of microcracks in quartz from the Cretaceous granodiorite core samples drilled through the Nojima Fault, south-west Japan, *Island Arc*, 10 (3- 4), 495-505.
- Tatham, D. J., G. E. Lloyd, R. W. H. Butler, and M. Casey (2008), Amphibole and lower crustal seismic properties, *Earth and Planetary Science Letters*, 267 (1-2), 118-128, doi:10.1016/j.epst.2007.11.042.
- Vermilye, J., and C. Scholz (1998), The process zone: A microstructural view of fault growth, *Journal of Geophysical Research - Solid Earth* , 103 (B6), 12,223-12,237.
- Vollbrecht, A., S. Rust, and K. Weber (1991), Development of microcracks in granites during cooling and uplift - examples from the variscan basement in NE Bavaria, Germany, *Journal of Structural Geology*, 13 (7), 787-799.
- Vrána, S. (1988), The Moldanubian Zone in Southern Bohemia: polyphase evolution of imbricated crustal and upper mantle segments , *Proceedings of the first international conference on the Bohemian Massif*. Czech Geological Survey, Prague, 331-336.
- Vrána, S., P. Blümel, and K. Petrakakis (1995), Moldanubian Zone: metamorphic evolution , in *Pre-Permian geology of the central and western Europe*. Springer, Berlin , edited by Dallmeyer, D. and Franke, W. and Weber, K. , 453-466.

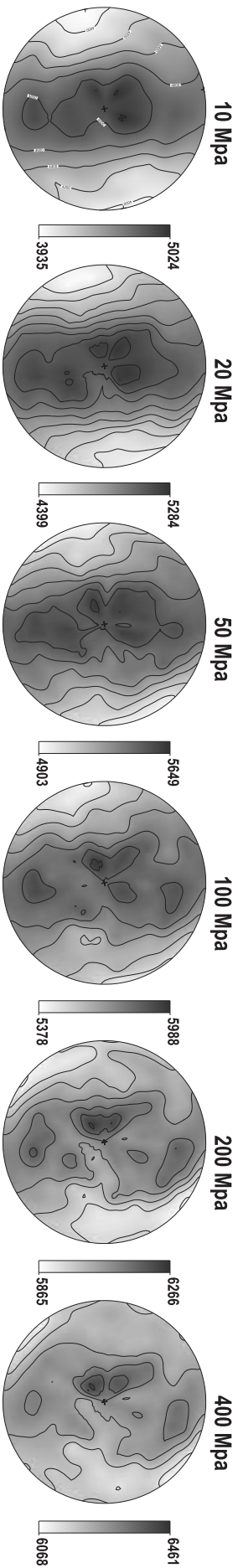
- Wibberley, C., and T. Shimamoto (2003), Internal structure and permeability of major strike-slip fault zones: the Median Tectonic Line in Mie Prefecture, Southwest Japan, *Journal of Structural Geology* , 25 (1), 59-78.
- Wilson, J., J. Chester, and F. Chester (2003), Microfracture analysis of fault growth and wear processes, Punchbowl Fault, San Andreas System, California, *Journal of Structural Geology*, 25 (11), 1855-1873, doi:10.1016/S0191- 8141(03)00036-1.
- Wong, T. (1985), Geometric probability approach to the characterization and analysis of microcracking in rocks , *Mechanics of Materials* , 4 , 261-276.
- Zang, A., F. Wagner, S. Stanchits, C. Janssen, and G. Dresen (2000), Fracture process zone in granite, *Journal of Geophysical Research - Solid Earth* , 105 (B10), 23,651-23,661.
- Zhang, X., R. Harkness, and N. Last (1992), Evaluation of connectivity characteristics of naturally jointed rock masses, *Engineering Geology*, 33 (1), 11-30.
- Zoback, M., and J. Byerlee (1975), Effect of microcrack dilatancy on permeability of Westerly granite, *Journal of Geophysical Research* , 80 (5), 752-755.
- Zoback, M., and J. Townend (2001), Implications of hydrostatic pore pressures and high crustal strength for the deformation of intraplate lithosphere, *Tectonophysics*, 336 (1-4), 19-30. 10

A. Appendix I

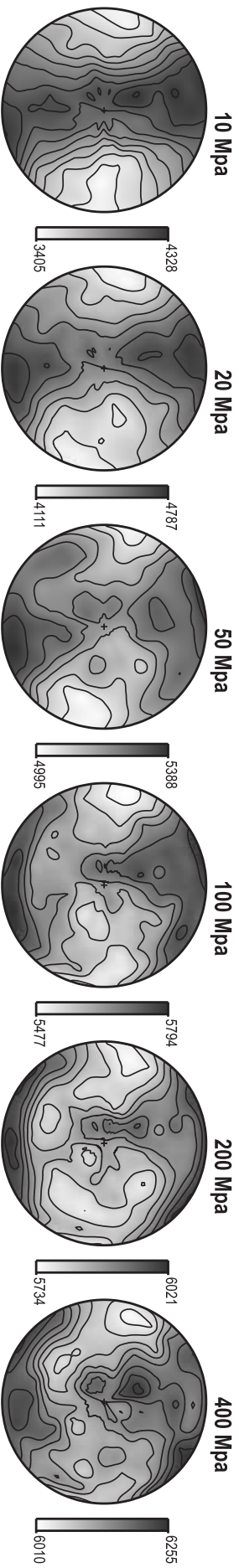
Results of measurements of P-wave velocity spatial distribution (V_p) at all measured pressure levels. Partial stereodiagrams of the of the P-wave velocity differences ($\Delta V_p(\Delta p)$) between succeeding pressure levels. Variety I - sample me01, and me04, Variety II sample me02 and me07. Variety III sample me03, me05 and me06. Diagrams are in the form of velocity and velocity differences isolines projected onto the lower hemisphere, equal area projection. Reference plane (full line) is oriented in N-S direction with dip direction to the S of the diagram.

VARIETY I - P-WAVE VELOCITY DISTRIBUTION

(a) me01

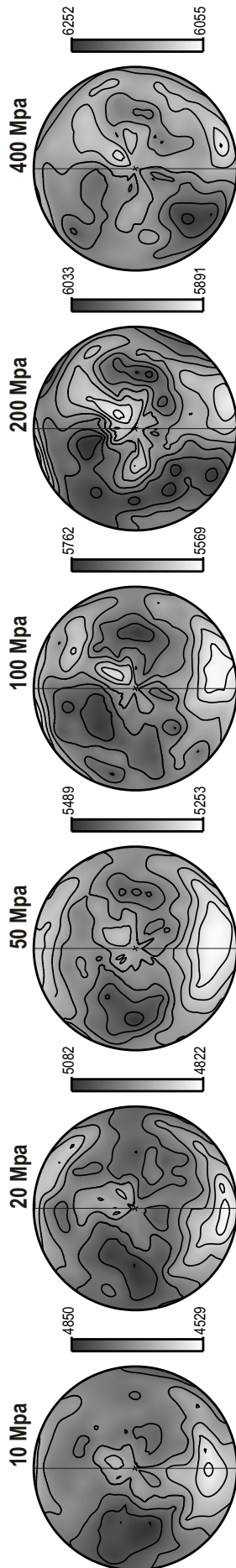


(b) me04

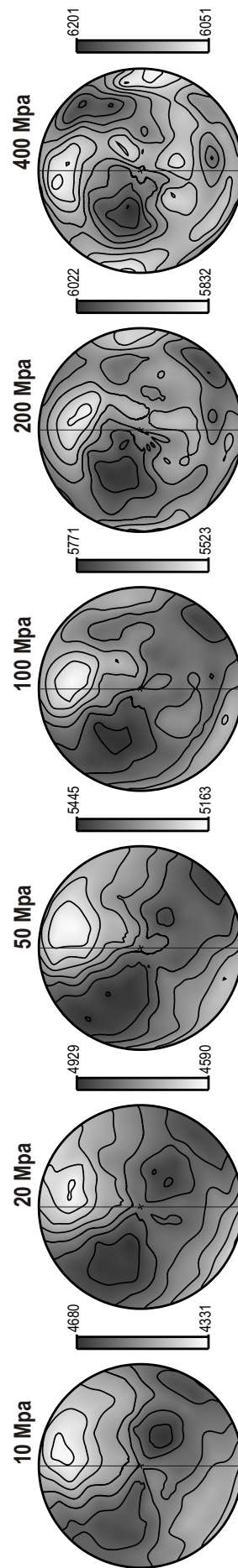


VARIETY II - P WAVE VELOCITY DISTRIBUTION

(a) me02

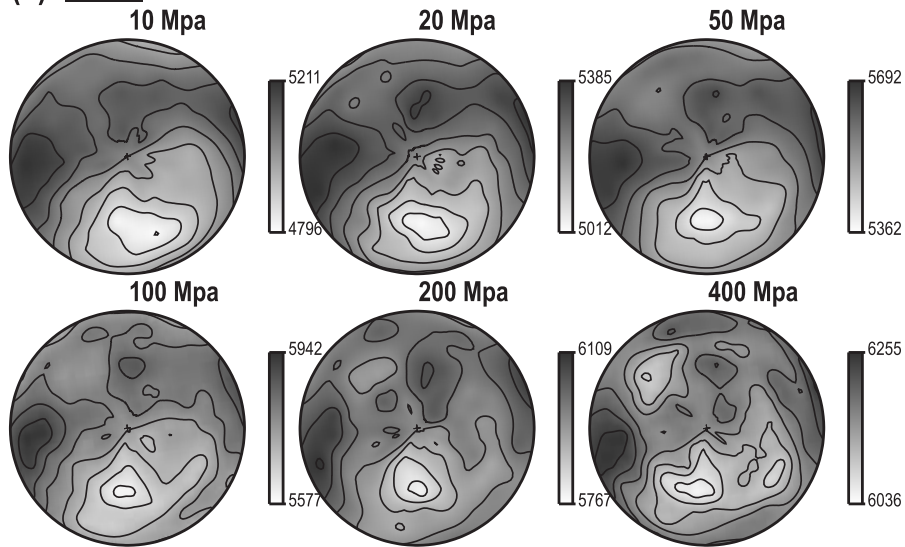


(b) me07

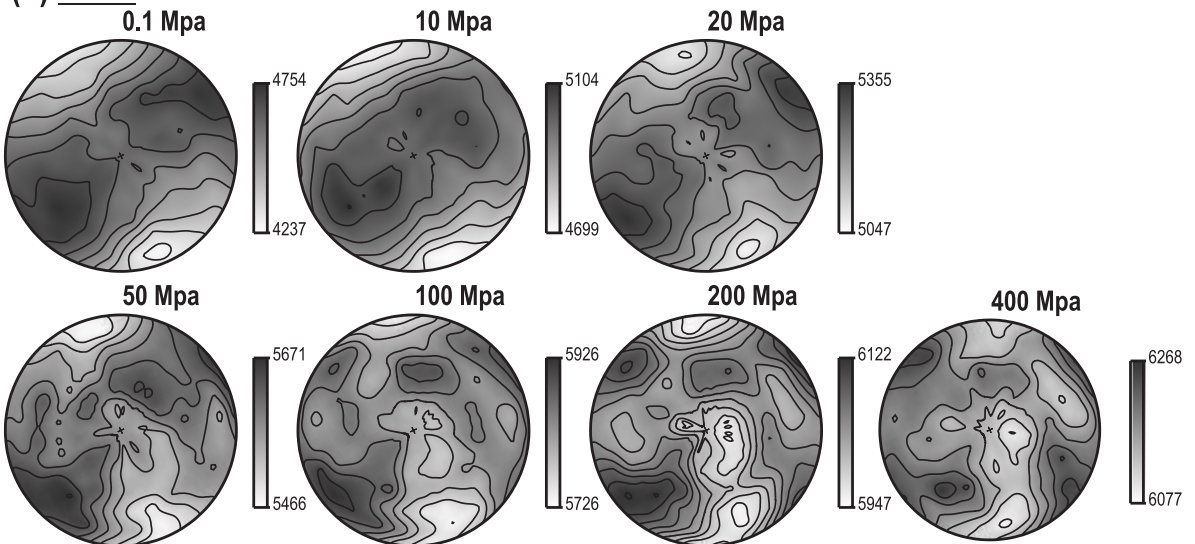


VARIETY III - P WAVE VELOCITY DISTRIBUTION

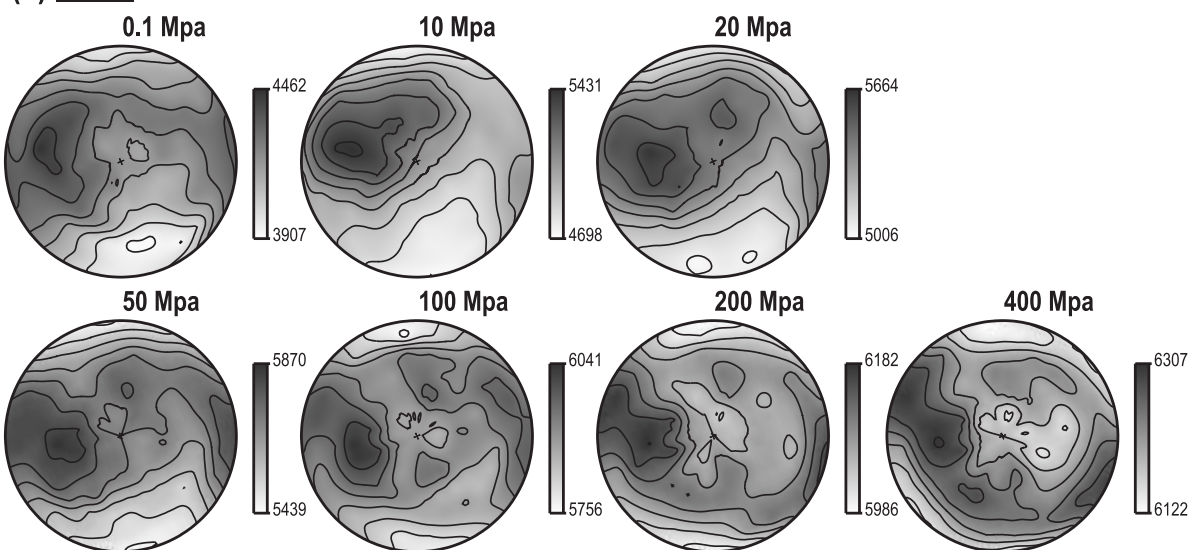
(a) me03



(b) me05

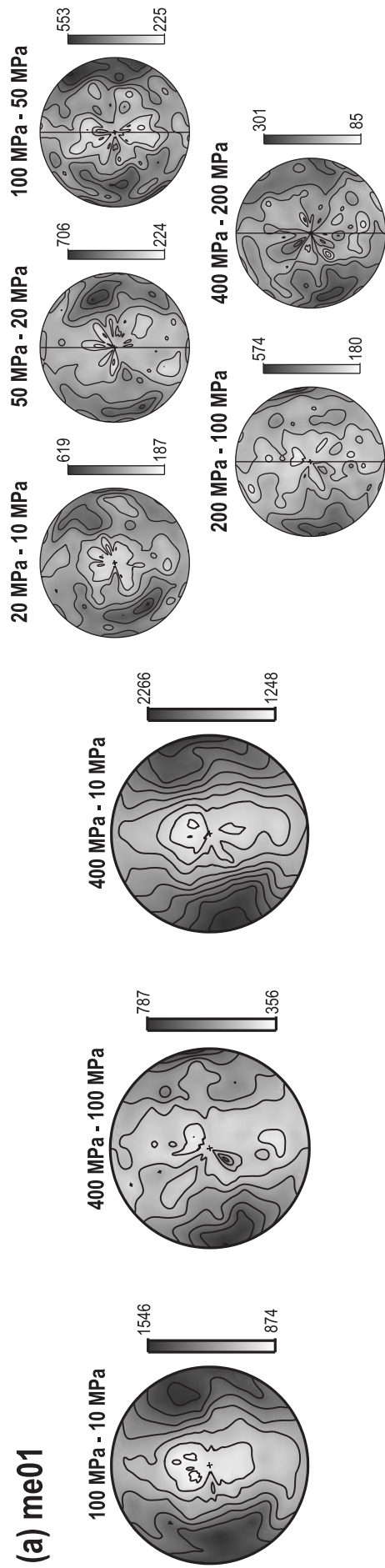


(c) me06

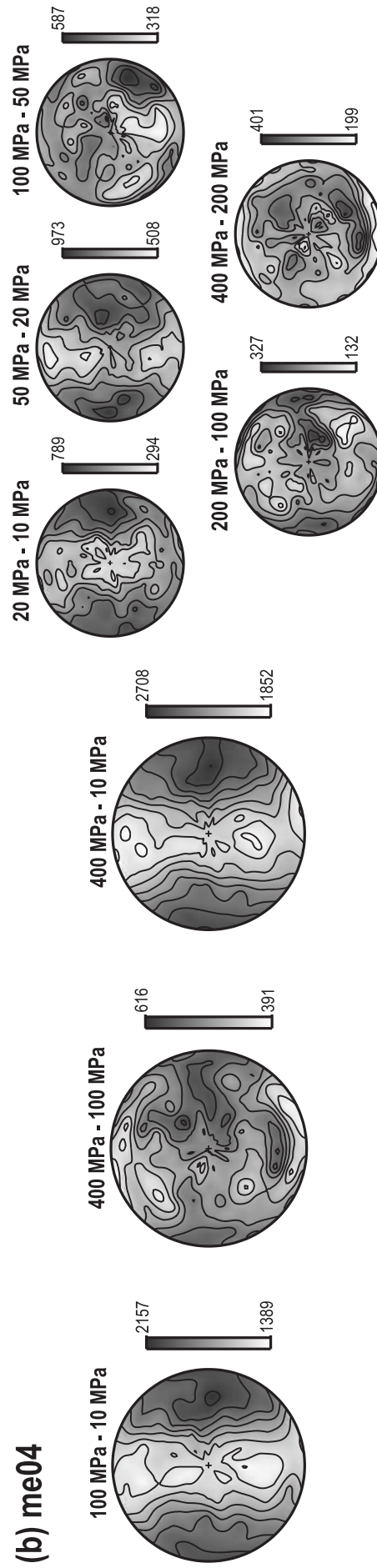


VARIETY I - P-WAVE VELOCITY DIFFERENCES (PORE SPACE)

(a) me01

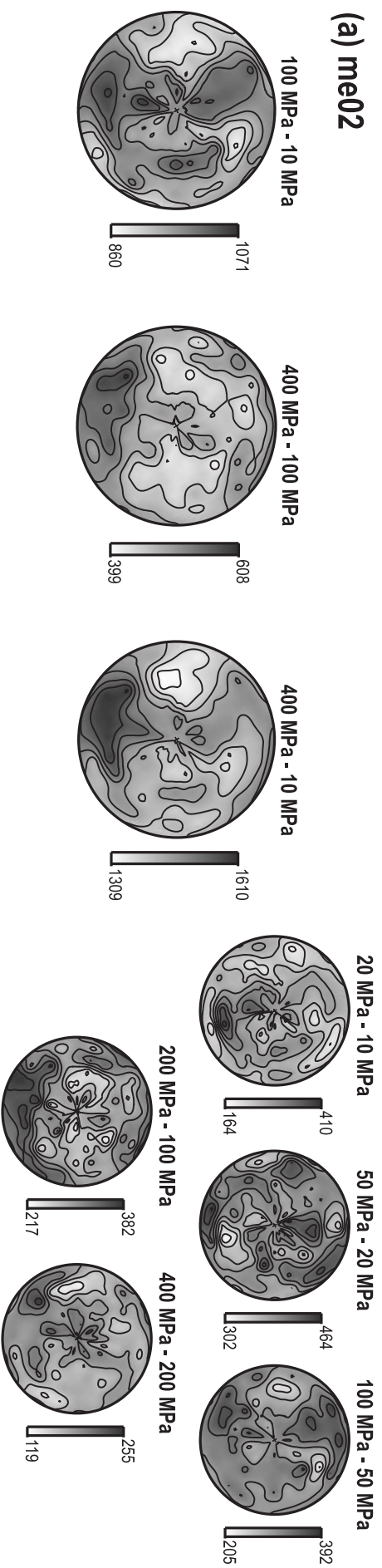


(b) me04

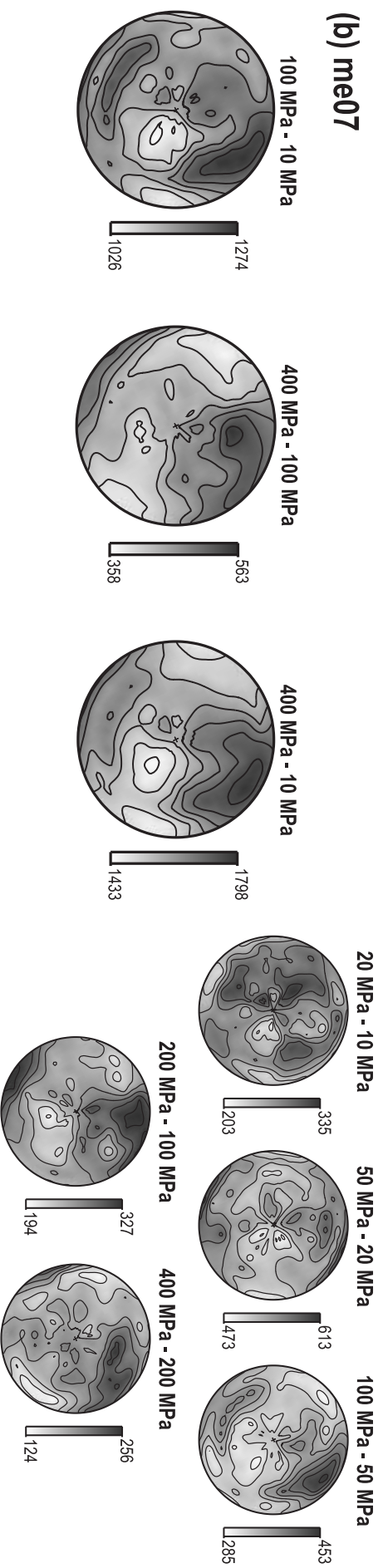


VARIETY II - P WAVE VELOCITY DIFFERENCES (PORE SPACE)

(a) me02

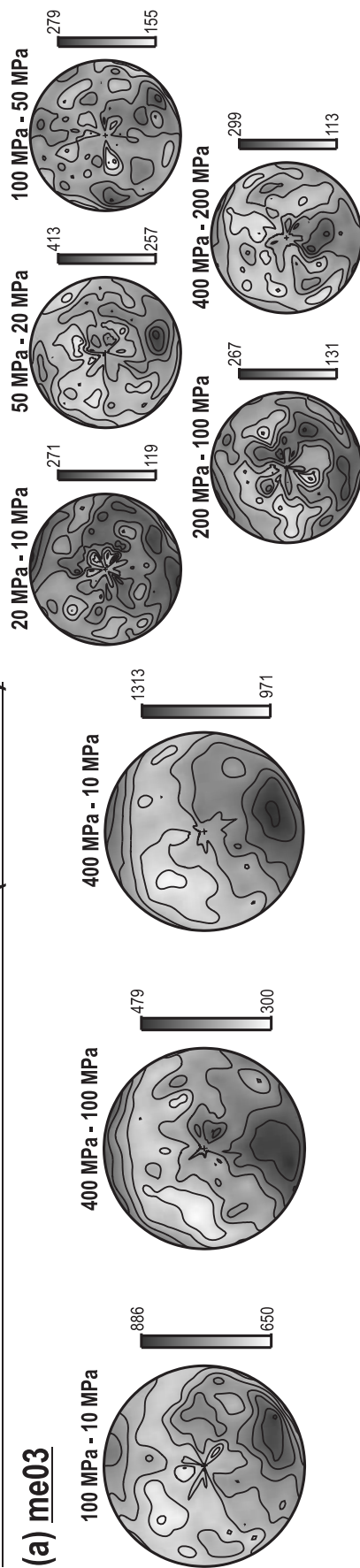


(b) me07

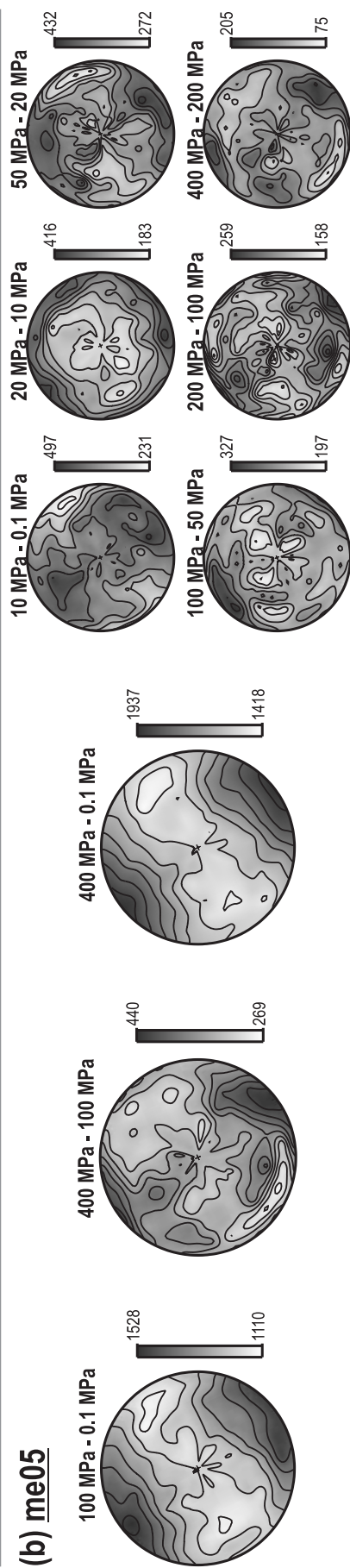


VARIETY III - P WAVE VELOCITY DIFFERENCES (PORE SPACE)

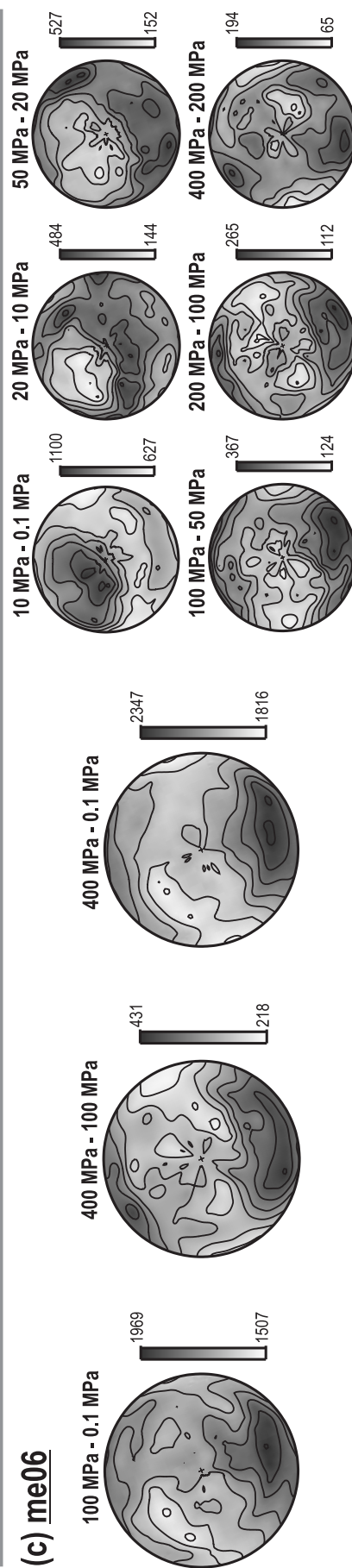
(a) me03



(b) me05



(c) me06



B. Appendix II

Summary of (A) P-wave velocity measurements and (B) P-wave velocity differences of all samples from Melechov masiff. Variety I - sample me01 and me04. Variety II sample me02 and me07. Variety III sample me03, me05 and me06. Pressure - confining pressure during experiment (velocity) and differences between indicated pressure levels, min V_P and max V_P - minimum and maximum velocity, k - velocity anisotropy, average V_P - average velocity difference, min ΔV_P and max ΔV_P - minimum and maximum of velocity difference, A - anisotropy of velocity difference, ΔV_P - average velocity difference.

(A) Summary of P-wave velocity measurements						
	Sample	Pressure (MPa)	min V_P (ms ⁻¹)	max V_P (ms ⁻¹)	k (%)	average V_P (ms ⁻¹)
Variety I	me01	10	3935	5024	24.3	4479
		20	4399	5284	18.2	4874
		50	4903	5649	14	5311
		100	5378	5988	10.7	5701
		200	5865	6266	6.6	6035
		400	6068	6461	6.3	6227
	me04	10	3405	4328	23.6	3906
		20	4111	4787	15.2	4458
		50	4995	5388	7.6	5200
		100	5477	5794	5.6	5641
		200	5734	6021	4.9	5864
		400	6010	6255	4	6142
Variety II	me02	10	4529	4850	6.8	4713
		20	4822	5082	5.2	4970
		50	5253	5489	4.4	5359
		100	5569	5762	3.4	5668
		200	5891	6033	2.4	5972
		400	6055	6252	3.2	6152
	me07	10	4331	4680	7.7	4523

(A) Summary of P-wave velocity measurements

Sample		Pressure (MPa)	min V_P (ms^{-1})	max V_P (ms^{-1})	k (%)	average V_P (ms^{-1})
Variety III		20	4590	4929	7.1	4795
		50	5163	5445	5.3	5329
		100	5523	5771	4.4	5672
		200	5832	6022	3.2	5934
		400	6051	6201	2.5	6115
	me03	10	4796	5211	8.3	5026
		20	5012	5385	7.1	5237
		50	5362	5692	5.9	5556
		100	5577	5942	6.3	5768
		200	5767	6109	5.7	5970
	me05	400	6036	6255	3.6	6157
		0.1	4237	4754	11.4	4541
		10	4699	5104	8.2	4923
		20	5047	5355	5.9	5218
		50	5466	5671	3.7	5576
	me06	100	5726	5926	3.4	5828
		200	5947	6122	2.9	6033
		400	6077	6268	3.1	6174
		0.1	3907	4462	13.3	4175
		10	4698	5431	14.7	4976
		20	5006	5664	12.4	5297
		50	5439	5870	7.6	5656
		100	5756	6041	4.8	5899
		200	5986	6182	3.2	6081
		400	6122	6307	3	6211

(B) Summary of P-wave velocity differences

Sample		Pressure (MPa)	min ΔV_P (ms^{-1})	max ΔV_P (ms^{-1})	A (%)	ΔV_P (ms^{-1})
Variety I	me01	20-10	187	619	8.2	375
		50-20	224	706	8.5	421
		100-50	225	553	5.5	374
		200-100	180	574	6.3	322
		400-200	85	301	3.3	188
		400-10	1248	2266	15.8	1682
		400-100	356	787	6.7	510
		100-10	874	1546	11.2	1171
	me04	20-10	294	789	10.3	524
		50-20	508	973	8.6	734
		100-50	318	587	4.6	438
		200-100	132	327	3.2	222
		400-200	199	401	3.2	281
		400-200d	195	375	2.9	288
		400-10	1852	2708	13.7	2201
		400-100	391	616	3.6	504
		100-10	1389	2157	13.3	1697

(B) Summary of P-wave velocity differences

	Sample	Pressure (MPa)	min ΔV_P (ms ⁻¹)	max ΔV_P (ms ⁻¹)	A (%)	ΔV_P (ms ⁻¹)
Variety II	me02	20-10	164	410	4.8	260
		50-20	302	464	3	388
		100-50	205	392	3.2	308
		200-100	217	382	2.7	298
		400-200	119	255	2.2	182
		400-10	1309	1610	4.8	1438
		400-100	399	608	3.3	480
		100-10	860	1071	3.7	958
	me07	20-10	203	335	2.7	274
		50-20	473	613	2.6	529
		100-50	285	453	2.9	340
		200-100	194	327	2.2	259
		400-200	124	256	2.1	182
		400-10	1433	1798	5.9	1586
		400-100	358	563	3.3	442
		100-10	1026	1274	4.3	1144
Variety III	me03	20-10	119	271	2.8	208
		50-20	257	413	2.7	318
		100-50	131	267	2.2	200
		200-100	17	70	0.9	42
		400-200	113	299	3	188
		400-100	300	479	2.9	388
		100-10	650	886	4	739
	me05	10-0.1	231	497	5.2	384
		20-10	183	416	4.4	279
		50-20	272	432	2.8	354
		100-50	197	327	2.2	249
		200-100	158	259	1.6	201
		400-200	75	205	2.1	140
		400-0.1	1418	1937	8.3	1609
		400-100	269	440	2.7	342
		100-0.1	1110	1528	7.1	1267
	me06	10-0.1	627	1100	8.7	818
		20-10	144	484	6	324
		50-20	152	527	6.4	342
		100-50	124	367	4	233
		200-100	112	265	2.5	177
		400-200	65	194	2	128
		400-0.1	1816	2347	8.4	2027
		400-100	218	431	3.4	306
		100-0.1	1507	1969	7.6	1720

C. Appendix III

Summary of analysis of network connectivity performed on samples from Melechov masiff. Variety I - me01 and me04. Variety II - me07 and Variety III - me06. Order - order of the single crack network, $\sum B_k$ - the sum of the connected crack branches of all kth-order connected networks in a crack pattern, C_k - kth-order connectivity ratio as defined by Zhang et al. (1992) (see paragraph 1.3.2. Microstructure in Chapter I)

Summary of the analysis of network connectivity

	xz section			xy section			yz section		
	order	$\sum B_k$	C_k	order	$\sum B_k$	C_k	order	$\sum B_k$	C_k
Var. I	1	357	0.0318	1	261	0.0297	1	272	0.0288
me01	2	287	0.0256	2	175	0.02	2	225	0.0239
	3	275	0.0245	3	105	0.012	3	170	0.0181
	4	248	0.0221	4	58	0.0066	4	25	0.0027
	5	83	0.0074	5	90	0.0103	5	90	0.0096
	6	155	0.0138	6	102	0.0116	6	70	0.0074
	7	57	0.0051	7	39	0.0045	7	96	0.0102
	8	68	0.0061	8	47	0.0053	8	135	0.0143
	9	105	0.0094	9	54	0.0062	9	23	0.0024
	10	30	0.0027	10	27	0.0031	10	26	0.0028
	11	90	0.008	11	31	0.0035	11	64	0.0068
	12	103	0.0092	12	35	0.004	14	76	0.0081
	13	76	0.0068	13	71	0.0081	16	45	0.0048
	14	36	0.0032	14	38	0.0043	18	51	0.0054
	15	42	0.0037	16	43	0.0049	29	82	0.0087
	16	41	0.0037	17	48	0.0055	32	90	0.0096
	17	48	0.0043	19	50	0.0057	36	101	0.0107
	18	44	0.0039	20	60	0.0068	39	107	0.0114
	20	60	0.0053	22	58	0.0066	50	136	0.0145
	22	61	0.0054	23	60	0.0068	58	142	0.0151
	26	73	0.0065	24	67	0.0076	2716	7112	0.7557
	28	72	0.0064	25	63	0.0072			
	29	77	0.0069	26	75	0.0086			
	30	84	0.0075	27	71	0.008			
	32	171	0.0152	37	103	0.0118			

Summary of the analysis of network connectivity

	xz section			xy section			yz section		
	order	$\sum B_k$	C_k	order	$\sum B_k$	C_k	order	$\sum B_k$	C_k
	33	86	0.0077	43	116	0.0132			
	35	187	0.0167	2498	6579	0.7508			
	54	145	0.0129						
	56	143	0.0127						
	65	173	0.0154						
	89	230	0.0205						
	123	329	0.0293						
	142	362	0.0323						
	426	1113	0.0992						
	463	1246	0.111						
	1516	3997	0.3561						
Var. I	1	165	0.0104	1	153	0.0138	1	126	0.0107
me04	2	131	0.0083	2	131	0.0118	2	103	0.0087
	3	79	0.005	3	55	0.0049	3	36	0.0031
	4	92	0.0058	4	60	0.0054	4	9	0.0008
	5	143	0.009	5	77	0.0069	5	14	0.0012
	6	33	0.0021	6	16	0.0014	6	54	0.0046
	7	61	0.0038	7	81	0.0073	7	22	0.0019
	8	47	0.003	8	62	0.0056	8	43	0.0036
	9	23	0.0015	14	38	0.0034	11	29	0.0025
	11	32	0.002	15	40	0.0036	19	53	0.0045
	12	34	0.0021	3932	10148	0.9128	4388	11108	0.9417
	13	68	0.0043						
	17	48	0.003						
	18	51	0.0032						
	19	47	0.003						
	21	61	0.0038						
	22	117	0.0074						
	23	63	0.004						
	24	68	0.0043						
	25	73	0.0046						
	26	132	0.0083						
	29	72	0.0045						
	30	157	0.0099						
	32	85	0.0054						
	40	99	0.0062						
	49	130	0.0082						
	5288	13469	0.8494						
Var. II	1	551	0.1672	1	481	0.1012	1	262	0.0564
me07	2	311	0.0944	2	345	0.0726	2	131	0.0282
	3	194	0.0589	3	275	0.0578	3	250	0.0537
	4	241	0.0731	4	275	0.0579	4	112	0.0241
	5	149	0.0452	5	182	0.0383	5	155	0.0334
	6	73	0.0222	6	193	0.0405	6	78	0.0167
	7	103	0.0313	7	148	0.0311	7	113	0.0243
	8	120	0.0364	8	41	0.0086	8	108	0.0232

Summary of the analysis of network connectivity

xz section			xy section			yz section			
order	$\sum B_k$	C_k	order	$\sum B_k$	C_k	order	$\sum B_k$	C_k	
9	45	0.0137	9	144	0.0303	9	75	0.0161	
10	28	0.0085	10	52	0.0109	10	27	0.0058	
11	23	0.007	11	28	0.0059	11	30	0.0065	
12	91	0.0276	12	175	0.0368	12	27	0.0058	
13	52	0.0158	13	33	0.0069	13	35	0.0075	
14	31	0.0094	14	67	0.0141	14	110	0.0237	
17	42	0.0127	15	71	0.0149	16	37	0.008	
20	49	0.0149	16	37	0.0078	28	78	0.0168	
22	104	0.0316	17	45	0.0095	29	73	0.0157	
28	61	0.0185	18	131	0.0275	35	90	0.0194	
37	81	0.0246	19	55	0.0116	42	114	0.0245	
			20	52	0.0109	48	121	0.026	
			22	57	0.012	54	135	0.0291	
			40	95	0.02	64	168	0.0362	
			44	103	0.0217	66	163	0.0351	
			176	439	0.0923	73	186	0.04	
			185	481	0.1012	78	208	0.0448	
						110	278	0.0598	
						116	294	0.0632	
						156	401	0.0863	
						198	526	0.1132	
Var. III me06	1	506	0.036	1	116	0.0438	1	606	0.0411
	2	347	0.0247	2	59	0.0223	2	535	0.0363
	3	390	0.0277	3	110	0.0415	3	463	0.0313
	4	325	0.0231	4	99	0.0374	4	368	0.0249
	5	203	0.0144	5	59	0.0223	5	279	0.0189
	6	160	0.0114	6	34	0.0128	6	391	0.0265
	7	140	0.01	7	21	0.0079	7	234	0.0159
	8	115	0.0081	8	69	0.026	8	270	0.0183
	9	148	0.0105	9	48	0.0181	9	208	0.0141
	10	108	0.0077	11	61	0.023	10	140	0.0095
	11	118	0.0084	12	31	0.0117	11	151	0.0102
	12	140	0.01	13	73	0.0276	12	260	0.0176
	13	183	0.013	14	38	0.0143	13	35	0.0024
	14	36	0.0026	17	89	0.0336	14	192	0.013
	15	85	0.006	18	48	0.0181	15	165	0.0112
	16	173	0.0123	19	110	0.0415	16	82	0.0056
	17	93	0.0066	20	52	0.0196	17	139	0.0094
	18	96	0.0068	21	59	0.0223	18	93	0.0063
	19	55	0.0039	24	65	0.0245	19	100	0.0068
	20	164	0.0117	27	78	0.0294	20	103	0.007
	21	53	0.0038	28	79	0.0298	21	225	0.0152
	22	170	0.0121	30	84	0.0317	22	57	0.0039
	24	131	0.0093	31	79	0.0298	23	121	0.0082
	26	73	0.0052	39	207	0.0781	24	67	0.0045
	28	158	0.0112	44	117	0.0442	25	135	0.0091

Summary of the analysis of network connectivity

xz section			xy section			yz section		
order	$\sum B_k$	C_k	order	$\sum B_k$	C_k	order	$\sum B_k$	C_k
29	80	0.0057	78	203	0.0766	26	209	0.0142
31	168	0.0119	173	454	0.1714	27	286	0.0194
33	89	0.0063				28	152	0.0103
35	97	0.0069				29	75	0.0051
40	108	0.0077				32	251	0.017
42	115	0.0082				35	382	0.0259
47	126	0.009				36	94	0.0064
58	156	0.0111				37	200	0.0136
70	193	0.0137				39	205	0.0139
76	203	0.0144				40	207	0.014
80	200	0.0142				43	223	0.0151
87	230	0.0164				44	117	0.0079
113	294	0.0209				51	134	0.0091
227	607	0.0432				54	154	0.0104
231	600	0.0427				59	151	0.0102
473	1242	0.0883				65	166	0.0113
498	1314	0.0934				70	181	0.0123
639	1665	0.1183				76	411	0.0279
688	1817	0.1292				79	194	0.0131
						82	227	0.0154
						83	208	0.0141
						89	234	0.0159
						92	242	0.0164
						94	261	0.0177
						105	280	0.019
						106	277	0.0188
						109	271	0.0184
						132	361	0.0245
						135	348	0.0236
						144	396	0.0268
						151	398	0.027
						220	587	0.0398
						259	676	0.0458